Investigations of the Band Structure and Morphology of Nanostructured Surfaces

Kevin R. Knox

Submitted in partial fulfillment of the

requirements for the degree

of Doctor of Philosophy

in the Graduate School of Arts and Sciences

COLUMBIA UNIVERSITY

2011

ABSTRACT

Investigations of the Band Structure and Morphology of Nanostructured Surfaces

Kevin R. Knox

Two-dimensional electronic systems have long attracted interest in the physics and material science communities due to the exotic physics that arises from low-dimensional confinement. Studying the electronic behavior of 2D systems can provide insight into a variety of phenomena that are important to condensed-matter physics, including epitaxial growth, two-dimensional electron scattering and many-body physics. Correlation effects are strongly influenced by dimensionality, which determines the many-body excitations available to a system. In this dissertation, I examine the electronic structure of two very different types of two-dimensional systems: valence band electrons in single layer graphene and electronic states created at the vacuum interface of single crystal copper surfaces.The characteristics of both electronic systems depend intimately on the morphology of the surfaces they inhabit. Thus, in addition to discussing the respective band structures of these systems, a significant portion of this dissertation will be devoted to measurements of the surface morphology of these systems.

Free-standing exfoliated monolayer graphene is an ultra-thin flexible membrane and, as such, is known to exhibit large out-of-plane deformation due to substrate and adsorbate interaction as well as thermal vibrations and, possibly, intrinsic buckling. Such crystal deformation is known to limit mobility and increase local chemical reactivity. Additionally, deformations present a measurement challenge to researchers wishing to determine the band structure by angle-resolved photoemission since they limit electron coherence in such measurements. In this dissertation, I present low energy electron microscopy and micro-

probe diffraction measurements, which are used to image and characterize corrugation in SiO_2-supported and suspended exfoliated graphene at nanometer length scales. Diffraction line-shape analysis reveals quantitative differences in surface roughness on length scales below 20 nm which depend on film thickness and interaction with the substrate. Corrugation decreases with increasing film thickness, reflecting the increased stiffness of multilayer films. Specifically, single-layer graphene shows a markedly larger short range roughness than multilayer graphene. Due to the absence of interactions with the substrate, suspended graphene displays a smoother morphology and texture than supported graphene. A specific feature of suspended single-layer films is the dependence of corrugation on both adsorbate load and temperature, which is manifested by variations in the diffraction lineshape. The effects of both intrinsic and extrinsic corrugation factors will be discussed.

Through a carefully coordinated study I show how these surface morphology measurements can be combined with angle resolved photoemission measurements to understand the role of surface corrugation in the ARPES measurement process. The measurements described here rely on the development of an analytical formulation for relating the crystal corrugation to the photoemission linewidth. I present ARPES measurements that show that, despite significant deviation from planarity of the crystal, the electronic structure of exfoliated suspended graphene is nearly that of ideal, undoped graphene; the Dirac point is measured to be within 25 meV of E_F. Further, I show that suspended graphene behaves as a marginal Fermi-liquid, with a quasiparticle lifetime which scales as $(E - E_F)^{-1}$; comparison with other graphene and graphite data is discussed.

Image and surface states formed at the vacuum interface of a single crystal provide another example of a two dimensional electronic system. As with graphene, the surface quality and morphology strongly influence the physics in this 2D electronic system. However, in contrast to graphene, which must be treated as a flexible membrane with continuous height variation, roughness in clean single crystal surfaces arises from lattice dislocations, which introduce discrete height variations. Such height variations can be exploited to generate a self assembled nano-structured surface. In particular, by making a vicinal cut on a single

crystal surface, a nanoscale step array can be formed. A model system for such nanoscale self assembly is Cu(111). Cu(775) is formed by making an 8.5° viscinal cut of Cu(111) along the $[11\bar{2}]$ axis. The electronic states formed on the surface of this system, with a nanoscale step array of 14 Å terraces, shows markedly different behavior those formed on Cu(111).

In this dissertation, I show that the tunability of a femtosecond optical parametric oscillator, combined with its high-repetition rate and short pulse length, provides a powerful tool for resonant band mapping of the *sp* surface and image states on flat and vicinal Cu(111)-Cu (775) surfaces, over the photon energy range from 3.9 to 5 eV. Since the time scale for excitation of the metal image state from the Cu surface state is comparable with the electron-electron equilibration time scale, sharp features are measured due to resonant excitation in the photoelectron energy distribution curves. In addition, I explore the range of photon energies and optical intensities which may be used for this approach and show that despite the relatively high pump intensity, the 250 kHz repetition rate of this laser ameliorates the space-charge broadening and electron-energy shifting even for photon energies close to the vacuum edge.

The strong excitation conditions generated by a femtosecond laser pulse applied to a Cu surface also allow the excitation and observation of a recently measured bulk state. In this dissertation I show that angle-resolved, tunable, two-photon photoemission (2PPE) can be used to map a bulk unoccupied band, *viz.* the Cu *sp*-band 0 to 1 eV below the vacuum level, in the vicinity of the L point. This short-lived bulk band can be accessed using our setup due to the strong optical pump rate. I describe how photoemission from this state can be distinguished from photoemission from 2D states which is also present in the data. In particular, the variation of the final-state energy with $\hbar\omega$ has a measured slope of ~ 1.64 in contrast with values of 1 or 2 observed for 2PPE from two-dimensional (2D) states. This unique variation illustrates the significant role of the perpendicular momentum of initial and final states in interpreting 2PPE data.

Table of Contents

List of Figures

List of Tables

Acknowledgments

I owe an enormous debt of gratitude to the numerous people who have helped me during my time at Columbia. Without their help and support I would not have been able to complete my PhD. First and foremost, I would like to thank my advisor Prof. Richard Osgood, Jr., who has been a constant source of encouragement, guidance and support. He has provided a research environment that has enabled me to grow and develop as a scientist.

I am deeply indebted to the research scientists and post-doctoral scientists in Prof. Osgood's research group that have mentored me. In particular, I would like to thank Dr. Jerry Dadap, Jr., Prof. Mehmet Burak Yilmaz and Prof. Shancai Wang. They have provided invaluable training and support, including hands-on training in the technical aspects of experimental research, analysis of data and presentation of results. I would also like to thank the current and former members of Prof. Osgood's research group with whom I have collaborated. Their enthusiasm and dedication as well as their friendship have made my PhD experience particularly enjoyable and fulfilling. In particular, I would like to thank Nader Zaki, Dr. Denis Potapenko, Sung Young Hong, Prof. Nicolae Panoiu, Po-Chun Yeh, Dr. Ravi Bhat, Jeffrey Driscoll, Richard Grote, Dr. Alex Chen, Dr. Avishai Ofan, Ophir Gaathon, Dr. Xiaoping Liu, Dr. Zhaofeng Hao and Stan Huang.

Columbia University and, in particular, the NSEC collaboration provides an excellent environment for collaborative research. I would like to thank the numerous scientists who helped with many aspects of my work, including Prof. Philip Kim, Prof. James Hone, Dr. Stephane Berciaud, Dr. Dr. Chun Hung Lui, Dr. Melinda Han, Dr. Andrea Young, Dr. Changgu Lee, Dr. Erik Henriksen, Dr. Jim Yardley, Dr. Kin Fai Mak and Dr. Kirill Bolotin. I would also like to thank several theoreticians at Columbia and the NSEC for the numerous

enlightening conversations which provided invaluable insight into the fundamental physics underlying my experimental work; thanks to Dr. Mark Hybertsen, Prof. Igor Aleiner and Dr. Matthew Foster.

During my time at Columbia, I have been extremely fortunate to participate in numerous collaborative research projects with scientists at outside institutions both in the United States and abroad, including Brookhaven National Laboratory, TASC Laboratory in Trieste, Italy and the University of Zagreb. A very heartfelt thanks goes out to Prof. Alberto Morgante, Dr. Andrea Locatelli, Prof. Dean Cvetko, Dr. Tevfik Onur Mentes, Dr. Miguel Angel Niño, Dr. Pavel Dudin and Dr. Alexei Barinov. A large partion of the experimental work for my thesis was conducted in collaboration with these scientists at the Elettra Synchrotron light source in Trieste, Italy. During my visits to Elettra, my Italian collaborators were extremely gracious hosts. They are excellent scientists and have been great collaborators and close friends. Additionally, I would like to thank Dr. Peter Johnson at Brookhaven for mentoring. I would also like to thank Dr. Marko Kralj and Dr. Marin Petrovich at the University of Zagreb.

I would like to thank my fellow classmates in the Physics department: Dr. Adam Brown, Dr. Peter Kalmus, Dr. Seth Caughron, Dr. Tatia Engelmore, Dr. Chris Miller, Dr. Jake Hofman, Dr. Cien Shang, Dr. Gabriel Perez-Giz, Dr. Guillaume Plante , Dr. Marilena LoVerde, Dr. Rebecca Grossman, Dr. Mark Cooke, Dr. Mina Fazlollahi, Dr. Tzu-Ling Kuo, Dr. Xuejing Li, Dr. Matthew Lightman, Dr. Laura Newburgh, Dr. Eric Vazquez, Dr. Hugen Yan, Dr. Hui Zhou and Dr. Azfar Adil.

I would also like to thank the many excellent Professors at Columbia who provided me with a sound theoretical framework with which to begin my experimental work: Prof. Brian Greene, Prof. Miklos Gyulassy, Dr. Andrei Beloborodov, Prof. Tony Heinz, Prof. Daniel Kabat, Prof. Robert Mawhinney, Prof. Alfred Mueller.

I would like to thank my dissertation defense committee: Prof. Richard Osgood, Jr., Prof. Philip Kim, Prof Tony Heinz, Prof. Andrew Millis, and Prof. Jim Hone.

A special thanks goes out to David Perry, who graciously agreed to proof read this entire

document.

Last, but certainly not least, a very warm and heartfelt thanks goes out to my family, who have nurtured and supported me throughout my entire life. Without their love and encouragement I would not be where I am today.

I dedicate this dissertation to my beautiful
and loving wife, Meg, and our darling daughter, Juna.

Chapter 1

Introduction

1.1 Two Dimensional Surface Systems

Advances in nanoscale science and engineering over the last decade have revolutionized the world of materials, electronics, and optics. At the same time, improvements in the quality of experimental probes have allowed researchers to examine the electronic structure and dynamics of these nanoscale materials with new levels of precision in both energy and time. Nanosystems of reduced dimensionality provide an excellent platform for examining the emergent properties of complex systems. Low-dimensional surface systems, in particular, allow for a flexible and powerful approach to examining these phenomena, since they can be readily fabricated and altered by self-assembly. Further, because of their open nature, surface systems can be interrogated by the powerful momentum-selective probe of angular-resolved photoemission.

One example of a nanostructured surface system is self-assembled nanowires on single crystal metal surfaces. Ultrafast pump-probe measurements can be used to study lifetime in these nanosystems with the goal of understanding the interrelation of dynamics and confinement in these artificially fabricated nanosystems. In particular, in this dissertation I present work on a surface array patterned by natural self-assembly with Angstrom-scale features, viz. the surface of Cu(775). Additionally, I explore a free-standing monolayer film

formed via exfoliation techniques, viz. monolayer graphene, and examine the physics of this system using advanced photoemission and electron microscopy techniques.

First, I provide a brief overview of the physics in these systems. In particular, the unique massless fermionic band structure of single layer graphene will be presented along with a discussion of the surface morphology of graphene. The physics of electronic states at single crystal metal surfaces will then be presented. Specifically, the formation of surface states and image potential states at the vacuum interface of a single crystal metal will be discussed. Finally, a brief discussion of unoccupied bulk states in single crystal metals will be presented.

1.2 Graphene

Graphene is a single monolayer of carbon atoms arranged in a two-dimensional honeycomb lattice. It can be thought of as the building block for many carbon structures; fullerenes, which are zero-dimensional spherical arrangements of carbon atoms are essentially wrapped up graphene balls, carbon nanotubes are one-dimensional tubes of rolled graphene, and and graphite is a three-dimensional structure composed of stacked graphene sheets. Despite its ubiquity in these other forms, graphene was first produced in isolated form only very recently[9]. However, graphene has long been a subject of theoretical discussion, beginning with a 1947 paper by P.R. Wallace, who used graphene as a starting point to study the electronic structure of graphite[10].

The recent availability of monolayer-thick two-dimensional crystals such as graphene and Boron Nitride has generated widespread interest in the physics and materials science communities. In the case of graphene, in particular, the two dimensional nature of the crystal in combination with its unusual massless Dirac fermions determines a host of intriguing and unique transport phenomena, including graphene's half-integer quantum Hall effect (HE) and non-zero Berry's phase[11, 12]. Unlike most metals, undoped graphene has a Fermi surface which consists of a set of 2 inequivalent points in momentum-space. Thus, at zero temperature and zero doping, the density of states at the Fermi level vanishes. In

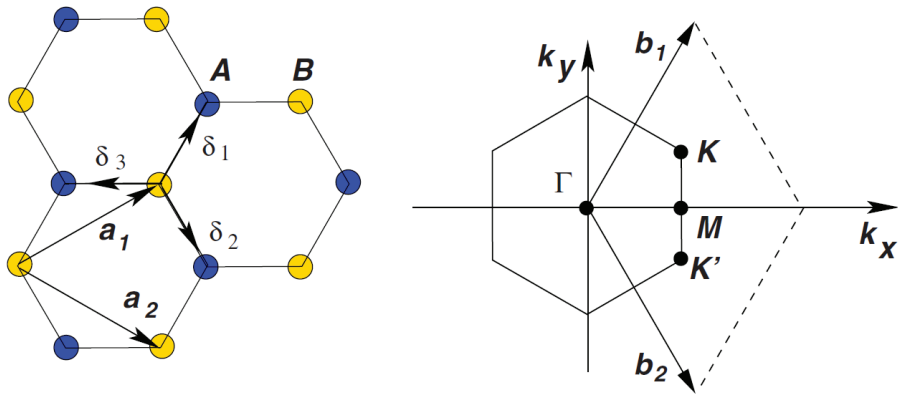

Figure 1.1: (Left) Lattice structure of graphene. A and B designate sublattice sites and a_1 and a_2 the primitive lattice vectors. The δ_i designate nearest neighbors. (Right) Reciprocal space of graphene showing Brillouin zone and primitive vectors of reciprocal lattice. This figure is adapted from Ref. [1]

combination with the linear dispersion of low energy charge carriers, this vanishing density of states is expected to lead to unusual band-renormalization effects that are not seen in Fermi-liquid systems such as unusually high electron-electron coupling.

1.2.1 Electronic Properties

The graphene unit cell contains two carbon atoms, denoted A and B in Fig. 1.1, separated by a distance of 1.42. The two primitive lattice vectors have length $\sqrt{3}a = 2.46$ and form a triangular lattice. Taken together, the two sublattices form the familiar hexagonal lattice of graphene. The corresponding Brillouin zone (BZ) is also hexagonal, with reciprocal space lattice vectors of distance $2/\sqrt{3}a$. The BZ is shown in Fig 1.1. The Dirac points are located at the two inequivalent corners of the BZ, labeled K and K'. They have positions in momentum space given by:

$$\mathbf{K} = (\frac{2\pi}{3\mathbf{a}}, \frac{2\pi}{3\sqrt{3}\mathbf{a}}),\ \mathbf{K}' = (\frac{2\pi}{3\mathbf{a}}, -\frac{2\pi}{3\sqrt{3}\mathbf{a}}) \tag{1.1}$$

Each carbon atom in the graphene crystal is connected to its 3 nearest neighbors by a σ bond formed by a hybridized sp^2 orbital. This σ bond leads to the trigonal planar

structure and is responsible for the enormous mechanical strength of the graphene lattice. The remaining p_z orbital is perpendicular to the planar structure and forms the π and π^* bands, which give graphene it's unique electronic properties. Following the standard tight-binding scheme, we can write the Hamiltonian for low-energy charge carriers in the π and π^* as:

$$H = -t \sum_{\mathbf{R}_A, \mathbf{R}_B} |\mathbf{R}_A\rangle\langle\mathbf{R}_B| + |\mathbf{R}_B\rangle\langle\mathbf{R}_A| \tag{1.2}$$

where t is the nearest-neighbor hopping energy and $|\mathbf{R}_A\rangle$ and $|\mathbf{R}_B\rangle$ represent the atomic orbitals centered at the sublattice points A and B, respectively. The summation is performed over all pairs of nearest neighbors in the crystal. Note that we do not include next-nearest-neighbor terms as their contribution has a negligible effect on the band structure for charge-carriers in close proximity to the Fermi level.

We now write the wavefunctions as explicit sums over the atomic orbitals:

$$|A_\mathbf{k}\rangle = \frac{1}{\sqrt{N}} \sum_{\mathbf{R}_A} e^{i\mathbf{k}\cdot\mathbf{R}_A} |\mathbf{R}_A\rangle \tag{1.3}$$

$$|B_\mathbf{k}\rangle = \frac{1}{\sqrt{N}} \sum_{\mathbf{R}_B} e^{i\mathbf{k}\cdot\mathbf{R}_B} |\mathbf{R}_B\rangle \tag{1.4}$$

where $\mathbf{k} = (k_x, k_y)$ is the 2D, in plane, momentum. This allows us to change bases and express the Hamiltonian in $\mathbf{k}$-space as:

$$H(\mathbf{k}) = -t \begin{pmatrix} 0 & \alpha(\mathbf{k}) \\ \alpha^*(\mathbf{k}) & 0 \end{pmatrix} \tag{1.5}$$

where $\alpha(\mathbf{k})$ is expressed as:

$$\alpha(\mathbf{k}) = e^{ik_x a} + 2e^{ik_y a/2} cos(\sqrt{3} a k_y/2) \tag{1.6}$$

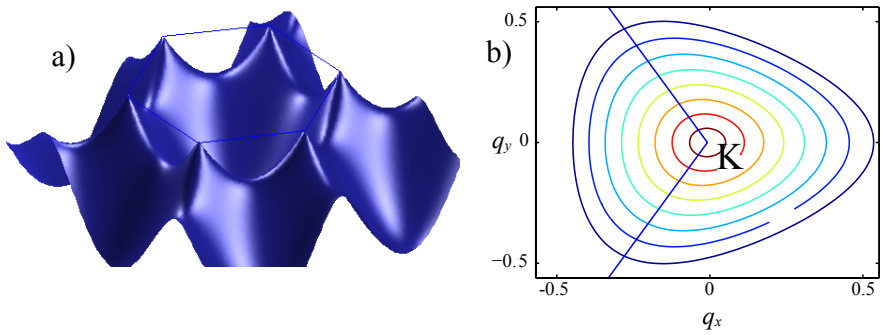

Figure 1.2: Graphene band structure. (a) Valence band dispersion given by Eq. 1.7. (b) Contour plot of conical dispersion in vicinity of K point. Successive equipotential lines are separated by 200 meV.

This results in the following band structure:

$$E(\mathbf{k}) = \pm t\sqrt{1 + 4cos(\sqrt{3}ak_y)cos(ak_x/2) + 4cos^2(ak_x/2)} \tag{1.7}$$

where the plus and minus signs correspond to the conduction (π^*) band and valence(π) band, respectively. A diagram of the valence band structure is shown in Fig x. The characteristic Dirac cones are obtained by expanding the band structure around the $\mathbf{K}$ point as $\mathbf{k} = \mathbf{K}+\mathbf{q}$. This leads to the simple energy dispersion:

$$E_\pm \approx \pm\hbar v_F|\mathbf{q}| \tag{1.8}$$

where v_F is the Fermi velocity, given by $v_F = 3ta/2\hbar$. With $t \approx 2.8$, the Fermi velocity is $\approx 10^6$ m/s. This result is in stark contrast to the standard quadratic dispersion found in most metallic systems, $E(\mathbf{q}) = q^2/2m$, (m is electron mass) where the group velocity, dE/dq, is energy dependent. In the case of graphene the dispersion is linear and the group velocity is a constant, independent of energy and momentum. Thus, the charge carriers in graphene behave like ultra-relativistic particles and can be described by the two dimensional massless Dirac Hamiltonian. The usual two-component Dirac spinors are replaced by eigenfunctions composed of two "pseudospin" components that correspond to the A and B sublattice sites

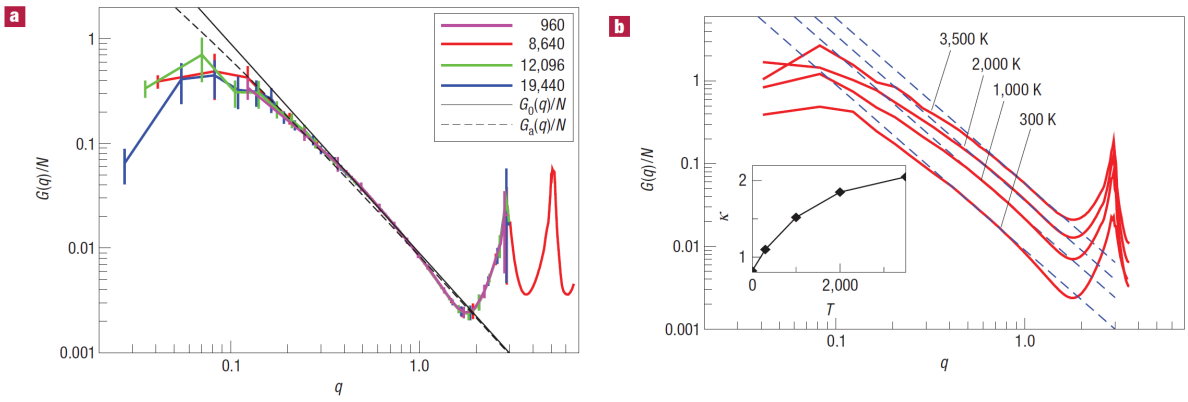

Figure 1.3: (a) Normal-normal correlation function in momentum space, $G(q)/N$, calculated from Monte Carlo simulations of free standing graphene sheets as performed by Fasolino *etal.* for finite graphene lattices of different sizes[2]. Solid straight line gives harmonic power-law behavior and dashed line shows anharmonic corrections. (b) $G(q)/N$ as a function of temperature. This figure is adapted from Ref. [2]

and the velocity of light is replaced by v_F, which is $\sim 1/300\ c$.

1.2.2 Morphology of Graphene

Only a single atom thick, graphene is the ultimate example of a flexible membrane—a true 2D crystal embedded in 3D space. Thus, in addition to the typical acoustic and optical phonon modes encountered in most 3D solids which disperse as $\omega_{\rm ac}(k) \propto k$ and $\omega_{\rm op}(k) \propto$ const, respectively, graphene has additional "flexural" phonon modes which arise due to the out-of-plane oscillations of its carbon atoms. The acoustic flexural mode disperses as $\omega_{\rm flex}(k) \propto k^2$ for small k. The existence of such a flexural mode has long been predicted to cause crumpling of 2D membranes[13, 14, 15] and, thus, before its recent discovery, there was significant debate about whether graphene could exist in the free-standing state. Since the flexural modes disperse at k^2, they dominate the behavior of structural fluctuations at long wavelengths.

The basic theory of flexible membranes can be used to explain this crumbling tendency[16]. We treat the graphene sheet as a smooth 2D membrane and represent the local height as $h(\mathbf{r})$, where $\mathbf{r}$ is the in-plane coordinate. The sheet is then parameterized by $\mathbf{R} = (\mathbf{r}, h(\mathbf{r}))$

and the local surface normal is given by:

$$\mathbf{N} = \frac{\mathbf{z} - \nabla h}{\sqrt{1 + (\nabla h)^2}} \tag{1.9}$$

where $\nabla = (\partial_x, \partial_y)$ is the gradient operator in 2D. For a perfectly flat graphene sheet, the surface normals at all $\mathbf{r}$ are aligned and $\nabla \cdot \mathbf{N} = 0$. The spontaneous creation of ripples costs energy which is proportional to the bending stiffness of the sheet, κ, and can be expressed as:

$$E_0 = \frac{\kappa}{2} \int d^2\mathbf{r} (\nabla \cdot \mathbf{N})^2 \approx \frac{\kappa}{2} \int d^2\mathbf{r} (\nabla^2 h)^2 \tag{1.10}$$

where the second expression is valid in the limit that $(\nabla h)^2 \ll 1$. Taking a Fourier transform of $h(\mathbf{r})$ to obtain $h_{\mathbf{k}}$ we can rewrite the above expression in momentum space as:

$$E_0 = \frac{\kappa}{2} \sum_{\mathbf{k}} h_{-\mathbf{k}} h_{\mathbf{k}} \tag{1.11}$$

We can now quantize the problem by introducing a momentum operator, $P_{\mathbf{k}}$, which allows us to write the Hamiltonian as:

$$H = \sum_{\mathbf{k}} \left(\frac{P_{-\mathbf{k}} P_{\mathbf{k}}}{2\sigma} + \frac{\kappa k^4}{2} h_{-\mathbf{k}} h_{\mathbf{k}} \right) \tag{1.12}$$

where σ is the 2D mass density of the sheet. This is easily recognized as the equation for simple harmonic motion in h with a frequency given by $\omega_{\text{flex}} = \sqrt{\kappa/\sigma}\ k^2$. From this result it is straightforward to see why the existence of long-wavelength phonons should cause crumpling in 2D sheets[16]. The number of flexural modes per unit area at a given temperature is obtained by integrating the Bose-Einstein occupation number, $n_{\mathbf{k}}$:

$$N_{\text{ph}} = \int \frac{d^2\mathbf{k}}{(2\pi)^2} n_{\mathbf{k}} = \frac{1}{2\pi} \int_0^\infty dk \frac{k}{\exp\left(\frac{\sqrt{\kappa/\sigma} k^2}{k_B T} \right) - 1} \tag{1.13}$$

The resulting integral is logarithmically divergent as $k \to 0$. For a system with finite

size, L, we can obtain a finite value for the integral by replacing the lower limit of integration with $k_{\min} = 2\pi/L$:

$$N_{\text{ph}} = \frac{\pi}{L_T^2} \ln\left(\frac{1}{1 - \exp\left(\frac{-L_T^2}{L^2}\right)}\right) \; ; \; L_T = \frac{2\pi}{\sqrt{k_B T}} \left(\frac{\kappa}{\sigma}\right)^{1/4} \tag{1.14}$$

Unfortunately, the above result only produces a well ordered system if $L \ll L_T$. However, for graphene $\kappa \approx 1$ eV [2] and $\sigma \approx 7.5 \times 10^{-7}$ kg/m^2 we find $L_T \approx 1$ Å at $T \approx 300$ K, which means that free-standing graphene should always crumple at room temperature. However, note that the above discussion is only valid in the harmonic approximation, where the flexural modes of graphene can be considered to be decoupled from the stretching modes. Recently, Fasolino, *et.al.* have proposed that, at a critical wavelength of ~ 20 nm, anharmonic corrections, which couple the bending and stretching modes, become dominant and prevent the membrane from crumpling (see Fig. 1.3) [2]. Through the use of Monte Carlo simulations of free standing graphene sheets, they have shown that the harmonic approximation is only valid for flexural phonons with wavelengths < 20 nm. At larger length scales coupling between the bending and stretching modes effectively damps long-wavelength phonons[2].

1.3 Two Dimensional Electronic States on Single-Crystal Metal Surfaces

"God made solids, but surfaces were the work of the devil." -Wolfgang Pauli

Due to the very large number of atoms present in a macroscopic solid, exact theoretical formulations of solid-state physics are essentially impossible to solve. Thankfully, for a very large class of materials, one can derive many of the basic properties of condensed-matter systems by exploiting the translational symmetry of an ideal crystalline lattice to reduce the number of free parameters from an insurmountable 10^{23} to a manageable handful. Thus, most theoretical models in solid state physics are based on the assumption of a

perfect crystalline lattice that extends infinitely in all directions. Such a description allows the application of a number of mathematical symmetry operations, which makes the problem tractable while still providing a good approximation to derive the basic macroscopic properties of a solid.

The introduction of a surface, however, complicates this approach. In particular, surface atoms have fewer neighbors than their bulk counterparts. Thus, chemical bonds must be broken to form the surface which costs energy. Additionally, due to the changes in chemical bonding, surface relaxations and reconstructions are common; surface atoms are displaced from the ideal positions they would occupy in the bulk. Even if one neglects these shifts in atomic positions and models a surface as a truncated bulk (with its atoms at bulk-like positions), new physics arises since the model system is no longer infinite in all directions.

Thus, the electronic structure in the vicinity of the surface of metals and semi-conductors is markedly different than that of the bulk due to the abrupt termination of the crystal lattice. In particular, surface states are formed, which are new electronic states localized to the few atomic layers closest to the surface. Such states exist within energy regions which are band gaps for the bulk and are, thus, not degenerate with any bulk bands. Additionally, if the bulk is metallic or semiconducting, a bound series of unoccupied states can form due to the attraction of an electron near the surface of the bulk to its "image charge." In this section, I present a brief review of the physics of surface states and image states.

1.3.1 Surface States

In general, the mathematical formalism used to determine the band-structure near the surface is more complicated than in the bulk, due to the broken symmetry along the direction perpendicular to the metal-vacuum interface. The translational symmetry which is normally assumed in the derivation of standard electronic Bloch states only applies along the direction parallel to the surface. However, a simple one-dimensional model can be used to understand the basic origin of surface states. In general, a 1D crystal potential with periodicity a can be written as a Fourier sum:

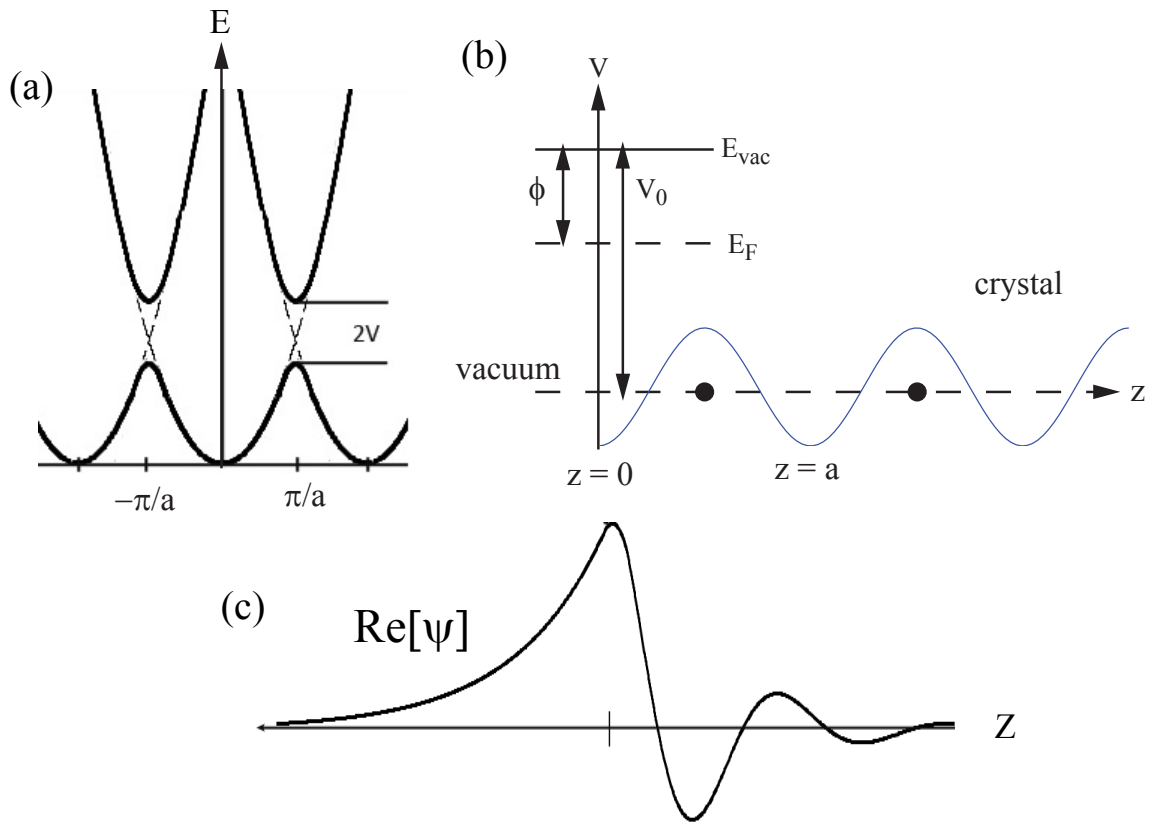

Figure 1.4: Formation of 1D Shockley surface state. (a) Energy bands along $k_\perp$for one-electron bulk states. (b) Nearly-free electron model with cosine potential along a semi-infinite linear chain. (c) Real part of the wave function for Shockley surface state.

$$V(z) = V_0 + \sum_n V_n e^{i\frac{2n\pi}{a}z}; n = \pm 1, \pm 2, ... \tag{1.15}$$

Consider, now, the case where the crystal has a periodic, but weak potential (so that the nearly-free electron model can be used) with the surface located at z=0. Keeping only the leading term in the above expansion and setting V_0=0, we write the potential as:

$$V(z) = \begin{cases} 2Vcos(\frac{2\pi}{a}z) & z > 0 \\ 0 & z < 0 \end{cases} \tag{1.16}$$

where the surface is located at $z = 0$ and $z > 0$ corresponds to the bulk and $z < 0$ to the vacuum.

Very far from the surface we can neglect the effect of termination of the crystal and the solution of the 1D Schrödinger for this potential takes on the standard Bloch wave form. Near the Brillouin-zone boundary ($k \sim \pi/a$) electrons are scattered from the $k = \pi/a$ state to the $k = -\pi/a$ state. Thus, the solutions have the form $\psi(z) = e^{ikz}(A + Be^{i(2\pi/a)]z})$. Plugging this form into the Schrödinger equation with the $V(z)$ potential it is straightforward to show that at the zone-boundaries the free-electron parabola splits and allowed and forbidden bands arise with a band gap of $2V$. This band structure is shown in Fig. 1.4. To extend these solutions to include the surface contribution we match this Bloch wave solution in the bulk onto a decaying exponential outside the bulk. Such a piecewise solution can be found for every possible energy eigenvalue within the allowed band. Thus, the corresponding energy levels are only slightly modified from those of the infinite bulk.

However, the presence of the surface allows us to introduce an additional solution by considering complex values of k, $k = p \pm iq$, where we again consider solutions near the zone-boundary, $p = \pi/a$:

$$\psi(z) = e^{\pm qz}e^{ipz}(A + Be^{i(2\pi/a)z}) \tag{1.17}$$

This class of solutions is forbidden for the infinite bulk crystal because the exponential

term $e^{\pm qz}$ diverges at $+\infty$ or -∞. However, for the semi-infinite crystal considered here we can consider the following solution:

$$\psi(z) = \begin{cases} e^{-qz}e^{ipz}(A + Be^{i(2\pi/a)z}) & z > 0 \\ C\ e^{q'z} & z < 0 \end{cases} \tag{1.18}$$

where, again, $z > 0$ corresponds to the bulk and $z < 0$ to the vacuum. Clearly, this solution decays to zero at both $+\infty$ and -∞. The coefficients A and B are chosen to be $A = e^{i\delta}$ and $B = e^{-i\delta}$, where δ ranges from -$\pi/2$ to 0 corresponding to the bottom and top of the band gap, respectively. After some calculation, the solution inside the crystal can then be written as:

$$\psi(z) = A'\ e^{-qz}\cos[(\pi/a)z + \delta] \tag{1.19}$$

The coefficients A' and C are then chosen to match ψ and $d\psi/dz$ at the surface. In general, there is always a region in the gap, $0 > \delta > -\pi/2$, where the two wavefunctions can be matched and a surface state can exist. From the form shown in Eq. 1.18 it is clear that the wavefunction is localized at the surface and decays exponentially into the vacuum and into the bulk. An example of Re[ψ] is shown in Fig. 1.4

We have shown that such a state can exist in the free-electron model. Such states can also be shown to arise starting with the tight-binding model. In the literature, these surface gap states are often denoted as Shockley states[17] or Tamm states[18] depending on whether they can be mathematically described by the nearly-free electron model or the tight-binding model, respectively.

1.3.2 Image States

Image states are two-dimensional quantized electronic states that form at the surface of a metal or high-dielectric-constant crystal[19, 20, 21, 22, 23]. They form as a result of the electrostatic attraction between an electron above the surface of the crystal and its

corresponding "image charge" in the bulk[19, 20]. In the presence of a projected surface band gap in the bulk a crystal barrier will be present for electrons of particular values of E and $k_{\|}$, preventing those electrons from being recaptured by the metal. Thus, a series of bound states are formed with a Rydberg-like progression of energies. Image states generally have longer lifetimes (20 - 100 fs) than bulk states due to the fact that the image state wavefunction is largely localized outside the metal with minimal penetration into the bulk. Image states are, however, sensitive to surface conditions and will be modified by the presence of adsorbates, step edges or surface roughness. Thus, these states are of interest because of their applicability to other areas of condensed-matter physics. They provide a useful model system with long lifetimes and precise energy eigenvalues to study the physics of two-dimensional electronic systems. Additionally, image states form on a very wide range of metallic surfaces and will change in character based on the underlying properties of the crystal surface. Thus, the study of image states can provide insight into a variety of phenomena that are important to condensed-matter physics, including epitaxial growth, two-dimensional electron scattering and low-dimensional confinement.

Figure 1.5 shows an idealized image-state system. The simplest way to calculate the energy spectrum of the system is to assume that the crystal barrier is infinite. The potential, $V(z)$, is then a $1/z$ form:

$$V(r) = \frac{-e^2}{4z} \tag{1.20}$$

where z is the distance from the electron to the metal surface. The problem is, then, analogous to the hydrogen-atom in one dimension and the spectrum is readily obtained as a Rydberg series:

$$E_n = \frac{-0.85}{n^2} \tag{1.21}$$

This simple treatment yields some useful results which aid in a basic understanding of image states. First, one observes that the spacing between successive Rydberg states

decreases as $1/n^2$ so that higher order states become more difficult to resolve by experimental techniques. However, it can also be shown that the z-position of the maximum value of the wavefunction scales as n^2, which means that higher order states are more decoupled from the bulk and, thus, longer lived with smaller widths in energy space.

A more precise treatment of the image state spectrum can be obtained by considering the phase shift of the electron wavefunction at its turning points. Denoting the phase shifts at the crystal barrier and Coulombic barrier as ϕ_c and ϕ_b, respectively, we can write the condition for a stationary state as :

$$\phi_c + \phi_b = 2\pi n \tag{1.22}$$

where ϕ_c and ϕ_b vary with the energy of the state. The phase shift at the Coulombic barrier, ϕ_b, was implicitly contained in the previous simplified model. However, by introducing an infinite crystal barrier, we have ignored any potential penetration of the image state into the bulk, which effectively fixes ϕ_c at π. By taking into account the variation in ϕ_c with energy (and from one metal to another) we can model penetration of the wavefunction into the crystal. Such penetration into the bulk also modifies the binding energy of the image-state and we obtain:

$$E_n = \frac{-0.85}{(n+a)^2} \tag{1.23}$$

where a is a quantum defect that depends on ϕ_c as:

$$a = \frac{1}{2}(1 - \frac{\phi_c}{\pi}) \tag{1.24}$$

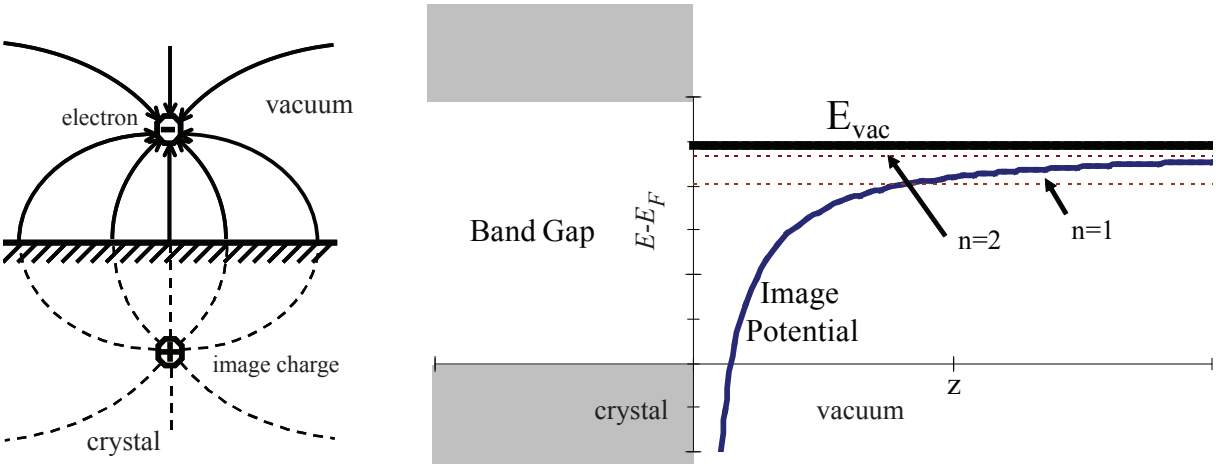

Figure 1.5: (Left) Electric field lines around an image state electron in the vicinity of a metal surface. (Right) Idealized image-state system. Diagram shows electrostatic potential as a function of distance from the surface as well as energetic location of the first two image states.

Chapter 2

Experimental Techniques

A wide range of specialized experimental techniques were employed in the investigations described in this dissertation. In this chapter I review basic principles underlying these experimental techniques and provide details about the specific experimental setups used to acquire data. I also describe the sample preparation procedures used to obtain both suspended and supported graphene as well as a well ordered nano-structured Cu(775) surface.

2.1 Spectroscopic Photoemission and Low Energy Electron Microscopy

2.1.1 Review of Low Energy Electron Microscopy

Low energy electron microscopy (LEEM) is a UHV surface imaging technique developed by Ernst Bauer and Wolfgang Telieps in 1985. In contrast to scanning microscopy techniques such as scanning electron microscopy (SEM) or scanning tunneling microscopy (STM), which require an electron beam or probe to be focused on a small spot and scanned across it, LEEM is a true imaging technique, i.e., all imaging pixels are acquired simultaneously from the illuminated area on the surface. This enables dynamic processes to be studied in real time. Additionally, LEEM differs from other electron microscopy techniques in that typical electron energies are on the order of 1 - 100 eV. Thus, the technique is highly surface sensitive

and allows the probing depth of the electron beam to be tuned by varying the energy.[3]

The basic setup of a LEEM instrument is shown in Fig. 2.2. High energy electrons (15 - 20 keV) are emitted from an electron gun and pass through a series of condenser lenses which focus and position the beam. The electrons are then sent through a magnetic beam separator (used to separate the incoming from the outgoing beams) and an objective lens before impinging on the sample. The sample is held at a very high voltage while the electron gun and objective are grounded such that the incoming electrons are decelerated to "low" energies before interacting with the surface. Backscattered electrons are then re-accelerated to high energies as they move away from the surface before passing back through the objective lens. The beam separator steers the backscattered electrons into the imaging column, after which they are detected by an imaging plate or screen.

Multiple contrast mechanisms exist in LEEM depending on the electron energy used and the specifics of the sample being probed. At typical LEEM energies, the cross section for elastic backscattering from the surface atoms depends both on the electron energy and on the chemical species of the scattering atom. In particular, the backscattering cross section is a non-monotonic function of nuclear charge, which allows one to image light adsorbates which may be present on substrates composed of heavier atoms. Additionally, the reflection coefficient for a crystalline solid varies strong with electron energy due to the band structure of the material; incident electrons with energies corresponding to band gaps in the material will be reflected with high probability, while those with energies that can be matched onto electronic states in the crystal will penetrate into the material. This phenomenon is identical to that encountered in an analysis of low-energy electron diffraction. Thus, a natural contrast mechanism for LEEM is based on local differences in the diffractions conditions, which occur if the periodicity of the sample varies as a function of location along the surface due to strain fields, dislocations, or local variations in surface structure or crystal orientation. This type of contrast is normally called "bright field contrast" if specularly reflected electrons are imaged. If the sample contains regions with different crystal orientations it can be useful to image non-specularly diffracted beams, which is called "dark field contrast." Another contrast

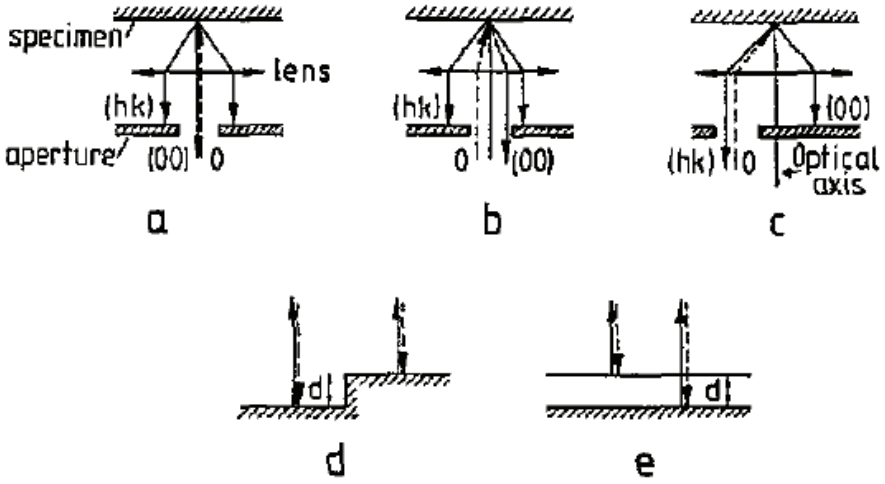

Figure 2.1: LEEM contrast mechanisms. (a-c) Diffraction contrast: (a,b) bright field, (c) dark field. (d, e) Interference contrast: (d) geometric phase contrast, (e) quantum size contrast. Figure adapted from Ref. [3]

mechanism is interference contrast due to surface steps or thin films, called "geometric phase contrast" and "quantum size contrast," respectively. Both mechanisms result from the interference caused by the difference in optical path-length for electrons reflected from the terraces bordering a step or from the top and bottom of a thin film. The quantum size effect is analogous to the effect produced by a Fabry-Pérot interferometer and is very useful for thin film growth studies by LEEM.[3] These LEEM contrast mechanisms are illustrated in Fig. 2.1

2.1.2 Nanospectroscopy Beamline at ELETTRA

All of the graphene measurements described in this dissertation were made using the Spectroscopic Photoemission and Low Energy Electron Microscope (SPELEEM) at the Nanospectroscopy beamline at the Elettra Synchrotron light source[24]. The SPELEEM is a versatile multi-technique microscope that combines low-energy electron microscopy (LEEM) with energy-filtered X-ray photoemission electron microscopy (XPEEM). The microscope images surfaces, interfaces and ultra-thin films using a range of complementary analytical characterization methods[25, 26]. When operated as a LEEM, the microscope probes the specimen

using elastically backscattered electrons. As described above, LEEM is highly sensitive to the surface crystalline structure and, due to the favorable backscattering cross-sections of most materials at low energies, allows image acquisition to be obtained at video frame rates. The lateral resolution of the microscope for LEEM imaging is currently below 10 nm. In XPEEM mode, the specimen is probed using the beamline photons, provided by an undulator source; thus, the technique is sensitive to the local chemical and electronic structures. Laterally resolved versions of synchrotron-based S-ray absorption (XAS) and photoemission spectroscopy (XPS) are possible. The principle of operation for X-ray photoemission will be described in section 2.3. the The lateral resolution in XPEEM approaches a few tens of nm.[27]

Along with real-space imaging, the SPELEEM microscope is capable of micro-probe diffraction imaging, i.e. laterally restricted low-energy electron diffraction ($\mu-$LEED) and angle-resolved photoemission electron spectroscopy ($\mu-$ARPES) measurements when probing with electrons and photons, respectively. In diffraction operation the microscope images and magnifies the back focal plane of the objective lens. In ARPES mode, the full angular emission pattern can be imaged on the detector up to a parallel momentum of $\sim 2\text{Å}^{-1}$; at larger parallel momentum the transmission of the microscope decreases. All diffraction measurements are restricted to areas of $\sim 2\ \mu m$ in diameter, which are selected by inserting a field-limiting-aperture into the first image plane along the imaging-optics column of the instrument. Thus, the microscope enables measurements on samples that are homogeneous over areas of a few square microns. The energy resolution of the SPELEEM is 300 meV and the momentum resolution of the microscope when operated in diffraction mode (LEED or ARPES) is $\sim 0.045\ \text{Å}^{-1}$. This value for the momentum resolution was obtained from calibration on a standard tungsten crystal; measurements using this crystal showed that the value changed by less than 5% as the kinetic energy of photoemitted electrons (or backscattered electrons for the case of LEED) increased from 25 to 100 eV. Specifically, the momentum resolution was observed to increase from $0.044\ \text{Å}^{-1}$ at 25 eV to $0.046\ \text{Å}^{-1}$ at 100 eV.

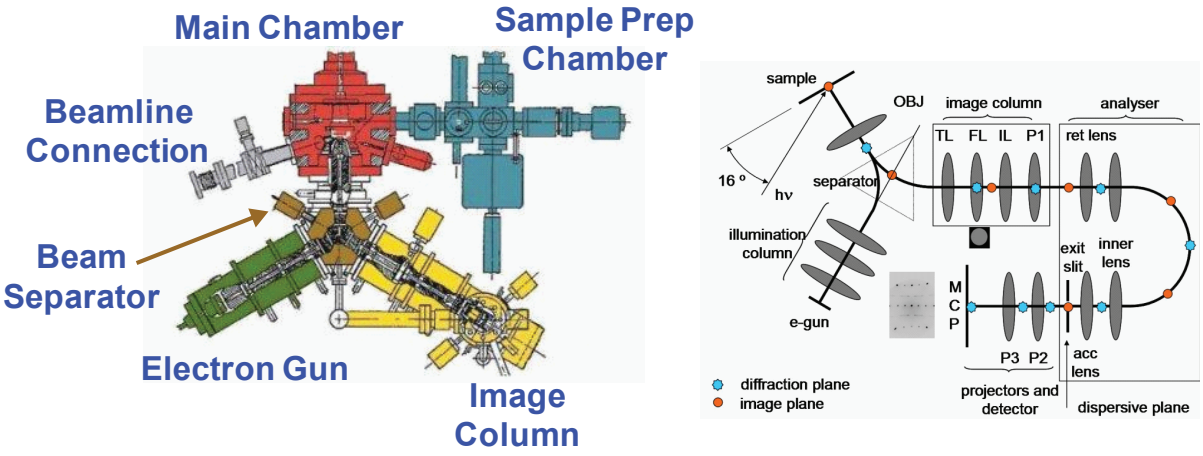

Figure 2.2: (Left) Schematic of SPELEEM microscope. (Right) Details of imaging column and electron analyzer.

Basic introductions to the techniques of LEED and ARPES will be presented in sections 2.2 and 2.3, respectively.

2.2 Low Energy Electron Diffraction

2.2.1 Review of Low Energy Electron Diffraction

Low energy electron diffraction (LEED) is a useful tool for determining the surface structural properties of both crystalline and amorphous materials. In a standard LEED setup a coherent electron plane wave with fixed energy and momentum is directed at a sample mounted in an ultra-high vacuum chamber. The far-field scattered electron intensity is then recorded as a function of scattering angle. Analysis of the resulting diffraction pattern provides useful information about the atomic structure of the sample. Typical electron energies range from 10 to 500 eV; thus the electron wavelengths are on the order of the distances between atoms in the sample (a few Å). Due to the strong interaction between electrons and atoms, the penetration depth of the incident electron beam is typically less than 10 Å.

Due to surface sensitivity of LEED and the need to verify that one has a clean, well ordered surface, a LEED setup is commonplace on nearly all UHV chambers that are employed for use in surface science experiments. A typical LEED setup is diagrammed in Fig. 2.3.

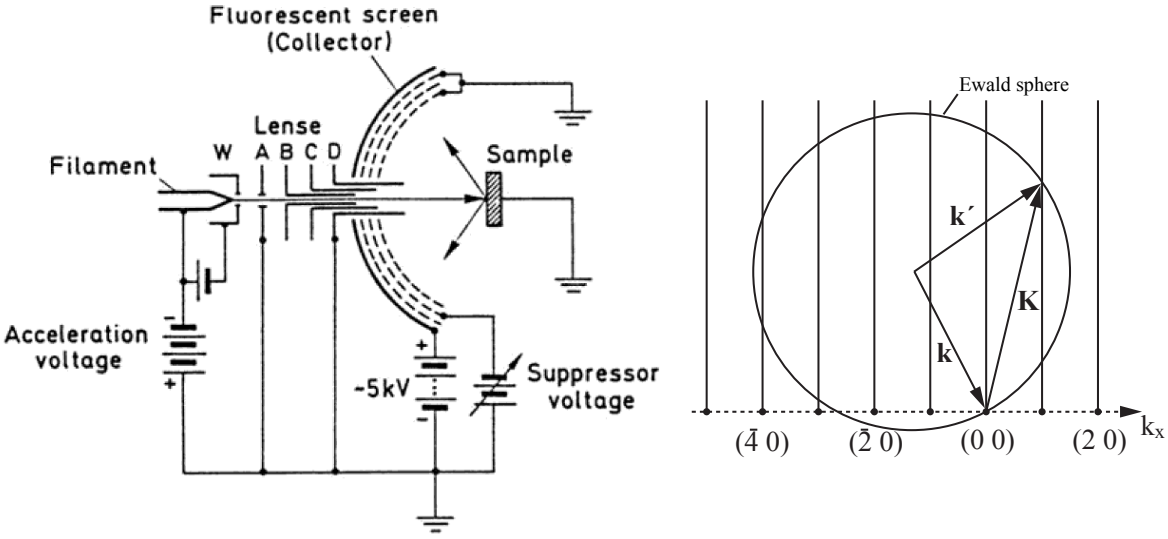

Figure 2.3: (Left) Schematic of a three-grid LEED unit. This figure is adapted from Ref. [4] (Right) Ewald sphere construction for LEED scattering. $\mathbf{k}$ and $\mathbf{k}'$ represent incoming and outgoing momentum vectors and $\mathbf{K} = \mathbf{k}' - \mathbf{k}$. The 2D reciprocal lattice points are plotted along the k_x direction with vertical rods extending from each point. The scattering condition $\mathbf{K}_{\parallel} = \mathbf{G}_{\parallel}$ can be fulfilled for every point at which the sphere crosses a reciprocal-lattice rod. The (1 0) scattering condition is shown explicitly.

Electrons generated by a heated cathode filament are accelerated and focused by a series of electrostatic lenses: A, B, C and D. The acceleration energy is determined by the potential between the cathode and apertures A and D, while apertures B and C are used to focus the electron beam. The last aperture, D, is grounded as is the sample and the first grid in front of the fluorescent screen; thus, electrons traveling towards sample as well as the scattered electrons propagate in a field free region. The backscattered electrons are detected by the fluorescent screen, which must be kept at a large positive bias (~ 5 keV) with respect to the first grid since only high energy electrons can cause the screen to fluoresce. A middle grid is positioned between the first (grounded) grid and the screen and kept at a slight negative bias in order to suppress inelastically scattered electrons.

2.2.2 Theory of LEED

In general, "slow" electrons interact very strongly with atoms in a solid, making an exact theoretical description of the LEED process rather complicated. In particular, multiple scattering events must be taken into account, which means the standard Born approximation is not sufficient. However, many of the essential features of a LEED experiment can be adequately described by the so-called kinematic theory, in which only single scattering events are taken into account. A brief description of the kinematic theory of LEED will be presented here.

We begin by assuming that the incident and scattered waves are both plane waves described by $\psi \propto e^{i(\mathbf{k}\cdot\mathbf{r}-Et/\hbar)}$. The scattering probability from an incident state, ψ_i, with wavevector $\mathbf{k}$, to a final state, ψ_s, with wavevector $\mathbf{k'}$, is proportional to the square of the transition amplitude, given by:

$$c_{\mathbf{k}\mathbf{k'}}(\tau) = \frac{-i}{\hbar}\int d\mathbf{r}\int_0^\tau dt\psi_s^*(\mathbf{r},t)V(\mathbf{r})\psi_i(\mathbf{r},t) \tag{2.1}$$

where $V(\mathbf{r},t)$ is the time-dependent potential that describes the interaction of the incident electrons with the crystal surface. $V(\mathbf{r},t)$ can be written as a sum over the individual atomic contributions as:

$$V(\mathbf{r},t) = \sum_n v[\mathbf{r}-\rho_n(t)] \tag{2.2}$$

where v is the interaction potential of a single atom and $n = (n_1, n_2, n_3)$ labels the atoms in the primitive lattice, which have time varying positions given by $\rho_n(t)$. Inserting our definitions for ψ_i, ψ_s and $V(\mathbf{r},t)$ into Eq. 2.1, we obtain:

$$c_{\mathbf{k}\mathbf{k'}}(\tau) = \frac{-i}{\hbar}\sum_n\int_0^\tau dt e^{i(E'-E)t/\hbar}e^{i(\mathbf{k}-\mathbf{k'})\cdot\rho_n(t)}f(\mathbf{K}) \tag{2.3}$$

where $\mathbf{K} = \mathbf{k}-\mathbf{k'}$ and $f(\mathbf{K})$ is the atomic scattering factor obtained by taking the Fourier transform of $v(\mathbf{r})$. We now explicitly separate the atomic position vectors into static com-

ponents parallel and perpendicular to the surface, as well as a time varying component that represents displacement from equilibrium: $\rho_n(t) = \mathbf{r}_{\parallel n} + \mathbf{r}_{\perp n} + \mathbf{s}_n(t)$. Inserting this definition into Eq. 2.3 the resulting scattering amplitude can be separated into an elastic term and an inelastic term. The inelastic term arises from the time dependence in $\mathbf{s}_n(t)$ and contains information about interaction with surface vibrational modes (phonons). Our main concern in this thesis will be the elastic scattering amplitude, which can be written as:

$$c_{\mathbf{k}\mathbf{k}'}(\tau) = \frac{-i}{\hbar} f(\mathbf{K}) \sum_n \int_0^\tau dt e^{i(E'-E)t/\hbar} e^{-i\mathbf{K}\cdot(\mathbf{r}_{\parallel n}+\mathbf{r}_{\perp n})} \tag{2.4}$$

In the $\tau \to \infty$ limit, the integration over t yields an energy-conserving delta function, $\delta(E' - E)$, as expected. The sum over n is essentially a sum over surface atoms since the penetration depth of the incident LEED beam is limited to a few surface layers. Thus, we obtain terms of the form:

$$\sum_{n_1,n_2} = e^{-i\mathbf{K}\cdot(n_1\mathbf{a}_1+n_2\mathbf{a}_2)} \tag{2.5}$$

where n_1 and n_2 are integers and $\mathbf{a}_1$ and $\mathbf{a}_2$ are primitive lattice vectors in the surface plane. If we let n_1 and n_2 run to infinity, the summation in 2.5 is non-zero only when $\mathbf{K} \cdot \mathbf{a}_1 = 2\pi h$ and $\mathbf{K} \cdot \mathbf{a}_2 = 2\pi k$, where h and k are integers. This condition expresses the familiar conservation of parallel momentum:

$$\mathbf{K}_\parallel = \mathbf{k}'_\parallel - \mathbf{k}_\parallel = \mathbf{G}_\parallel \tag{2.6}$$

where $\mathbf{G}$ is a primitive vector of the reciprocal lattice. Thus, in the basic kinematic interpretation of LEED, scattered intensity is found only when the change in parallel momentum of the scattered electron beam matches the parallel component of a reciprocal lattice vector. The same conservation of momentum is not found in the perpendicular direction, because, as noted above, the summation in 2.5 runs only over the atoms in the top-most layers.

A common visualization tool for illustrating the LEED diffraction condition is the Ewald

sphere, shown in Fig. 2.3. Along a grid in reciprocal lattice space the wave-vector of the incoming electron, $\mathbf{k}$, is positioned with its end at the (0,0) reciprocal lattice point and a sphere is constructed along its starting point. Vertical rods are then constructed starting at each point of the reciprocal lattice. The scattering condition $\mathbf{K}_{\parallel} = \mathbf{G}_{\parallel}$ is then fulfilled at the locus of points for which the Ewald sphere crosses a reciprocal-lattice rod.

2.2.3 Experimental Setup for LEED measurements

The LEED experiments described in this dissertation were performed using two instruments. LEED experiments performed on stepped Cu surfaces used a standard three-grid LEED similar to the one described above. LEED data obtained on suspended and supported monolayer graphene described in chapter 3 was taken with the SPELEEM microscope in operation at the Nanospectroscopy Beamline of the Elettra Synchrotron light source. Although the experimental setup for the SPELEEM microscopy differs from that of a conventional LEED setup, the underlying principle is the same. As described in section 2.1.2, diffraction measurements can be taken by imaging the back focal plane of the objective lens. Additionally, laterally restricted electron diffraction measurements are possible with the SPELEEM microscope by inserting a field limiting aperture into the first image plane along the imaging-optics column of the instrument. This allows regions as small as 2μm to be examined by LEED. Such lateral resolution is not possible with a conventional LEED setup, which employs an electron beam several mm in size.

2.3 Photoemission Spectroscopy

2.3.1 Review of Photoemission Spectroscopy

Photoemission Spectroscopy (PES) is a decades-old experimental technique that has been refined over the years and is still extensively used to study core levels and valence bands in a wide range of systems, ranging from simple monatomic gases to complex structures such as high-temperature superconductors. The first experimental detection of photoemission

was by Heinrich Hertz in 1887[28]. In the earliest experiments monochromatic radiation, obtained by passing light from a continuum source through a prism monochromater, was focused onto the surface of a potassium or sodium sample in a vacuum tube. Liberated electrons then traveled to a second metal plate within the vacuum, where the current generated was measured as a function of retarding voltage. Thus, the maximum kinetic energy of the photoelectrons could be determined by adjusting the retarding voltage until the current was completely suppressed. It was found that this energy depended on both the frequency of the incident radiation and the metal under investigation. Since these early experiments predate the development of modern quantum mechanics, the photoelectric effect, which cannot be adequately explained with the classical theory of electromagnetic radiation, was not fully understood at the time. However, in 1905 Einstein was able to explain the effect by invoking the quantum nature of light.[29] The basic equation governing the phenomenon is:

$$\mathrm{eU} = \mathrm{KE}_{\mathrm{max}} = \hbar\omega - \phi \tag{2.7}$$

where U is the retarding potential, $\mathrm{KE}_{\mathrm{max}}$ the maximum electron kinetic energy, ω the frequency of light, and ϕ the work function of the metal under investigation. Thus, the most energetic electrons are those closest to the Fermi level that absorb all the energy of an incoming photon, $\hbar\omega$, and lose the minimum energy required to escape the metal, ϕ.

In principle, modern PES studies are performed in the same way as those early experiments were. Fig. 2.5 shows a schematic of a modern PES experiment. Experiments are performed under ultra-high vacuum (UHV) conditions with pressures in the 10^{-10} torr range. Monochromatic light with photon energy $\hbar\omega$ and vector potential $\mathbf{A}$ impinges on the sample. A wide range of monochromatic photon sources are available, including laser radiation, gas discharge lamps, and synchrotron light sources. Together, these light sources provide a very wide range of photon energies, from a few eV from laser radiation all the way up to 1 keV or more from synchrotron sources, enabling the researcher to study a large variety of systems and phenomena including surface states, chemical bonding, valence

bands and core levels. The polarization and angle of incidence of the radiation can also be varied to access different electronic states in the system. The photoemitted electrons are detected and counted by an electron detector (usually a microchannel plate (MCP) or charge-coupled device (CCD)) after passing through an electrostatic energy analyzer, which determines their final-state kinetic energy, KE_f. In angle-resolved experiments the emission angle, (θ, ϕ), of the photoemitted electrons is also recorded. In some experiments, the spin of the photoemitted electrons is also detected.

Figure 2.5 shows a typical photoemission electron energy distribution curve and its relation to the energy band structure of a hypothetical metal with core levels and a valence band. As is shown, by plotting the total number of photoemitted electrons as a function of final state kinetic energy, a replica of the band structure of the solid is generated. Final state kinetic energies are referenced to the vacuum level, $\mathrm{E_F}$, while binding energies in solids are generally referenced to the vacuum level, $\mathrm{E_V}$. Thus, if the work function of the material under investigation is known, ($\phi = \mathrm{E_V}$ - $\mathrm{E_F}$), the binding energy of the initial states can be easily calculated from the final state kinetic energies according to:

$$\mathrm{KE}_f = \hbar\omega - \phi - |\mathrm{E_B}| \tag{2.8}$$

Additionally, parallel momentum, $k_\parallel$, is conserved in the photoemission process, so $k_\parallel$ for the initial state can be easily inferred from the final state kinetic energy and the angle of emission as:

$$k_\parallel = \frac{\sqrt{2\mathrm{m}_e\mathrm{KE}_f}}{\hbar}\sin(\theta) \tag{2.9}$$

2.3.2 Angle resolved Ultraviolet Photoemission Spectroscopy

The energy states of a metal or semiconductor are characterized by single-electron energies, E, and wavevectors, $\mathbf{k}$. It is the goal of angle-resolved ultraviolet photoemission spectroscopy (ARUPS) to determine the band structure by mapping this E($\mathbf{k}$) relationship[30, 31, 32, 33,

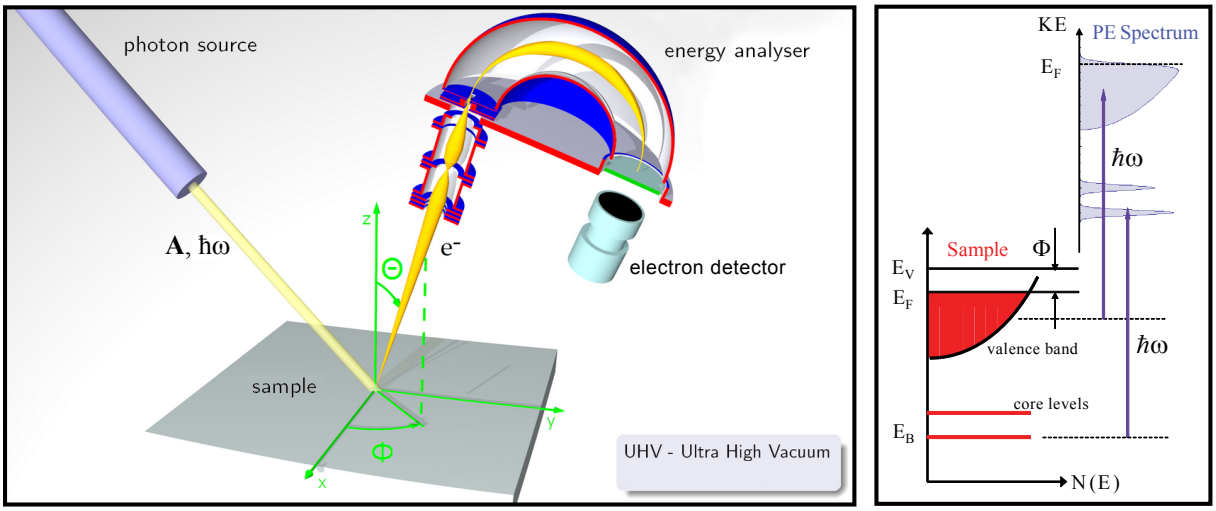

Figure 2.4: (Left) Typical PES setup. A light source provides photons of energy $\hbar\omega$ and vector potential $\mathbf{A}$. The emission angle, (θ, ϕ), and kinetic energy, KE, of photoemitted electrons are measured. Figure adapted from Ref. [5] (Right) Energy level diagram showing core levels and valence band in a solid sample along with the corresponding angle integrated energy distribution curve for photoemitted electrons. E_F and E_V refer to Fermi level and vacuum level, respectively.

6]. In the simplest model of photoemission, the transitions are vertical in a reduced zone scheme; they occur without the participation of other excitations.

The three-step model is the most commonly used model for the interpretation of photoemission spectra of solids.[34]. The PE process is broken up into 3 basic steps: the excitation of the photoelectron from its initial state to an excited state within the crystal, travel from the bulk to the surface, and escape from the surface into the vacuum. Although the process is purely phenomenological (in reality, the photoemission process occurs as a single step) it is adequate to describe many aspects of PE. The first step is considered within the reduced zone scheme and is a direct transition, meaning that the momentum of the electron is conserved up to a reciprocal lattice vector. If the photon has energy in the soft-UV range (which is the case for valence band ARUPS), its momentum can be neglected. The equation governing the initial excitation is:

$$\mathrm{N} = \sum_{i,f} |\mathbf{M}(\mathbf{k}_f, \mathbf{k}_i)|^2 \, \delta(E_f - E_i - \hbar\omega)\delta(\mathbf{k}_f - \mathbf{k}_i - \mathbf{G}) \tag{2.10}$$

where the delta functions explicitly conserve energy and momentum and the transition matrix, **M**, is evaluated between an initial and final state block waves within dipole approximation, where the interacting Hamiltonian is given by:

$$\mathrm{H}^{\mathrm{int}} = \frac{1}{2\mathrm{mc}}(\mathbf{A}\cdot\mathbf{p}) \tag{2.11}$$

In the final step, the electrons that are able to escape are those that have sufficient kinetic energy to overcome the surface potential barrier. As indicated in Eq. 2.10, the initial step preserves total electron momentum. However, in the final step as the electrons cross the surface potential barrier, they lose perpendicular momentum and only $k_{\|}$is conserved. There are several methods that exist to determine $k_{\perp}$. In particular, if one has knowledge about the intermediate excited state into which the electron is excited before escaping into the vacuum it is straightforward to calculate $k_{\perp}$since the first step in the 3-step process preserves total momentum. This is illustrated schematically in Fig. 2.5 (Left). Such information can come from *ab initio* band structure calculations. However, if the photon energy is sufficiently high, such that the intermediate excited state is many eV above E_F, it is more common to assume that this intermediate state "free-electron" like. One then simply uses the standard free-electron dispersion, $\hbar^2k^2/2m$, shifted below the vacuum level by the so-called "inner potential" of the metal.

2.3.3 Two-Photon Photoemission

The ARPES techniques described above can only be used to access *occupied* crystal states. In order to probe *unoccupied* states one must use an alternative technique such as inverse photoemission (IPE) [35, 36, 37] or two-photon photoemission (2PPE) [23, 38, 39, 20, 40, 41, 42, 43, 44, 45, 46, 47]. All of the data presented in this dissertation on unoccupied states of flat and stepped Cu surfaces was collected using two-photon photoemission. Thus, in this section I present a brief review of 2PPE.

The basic 2PPE scheme is illustrated in Fig. 2.6. An electron from an occupied state

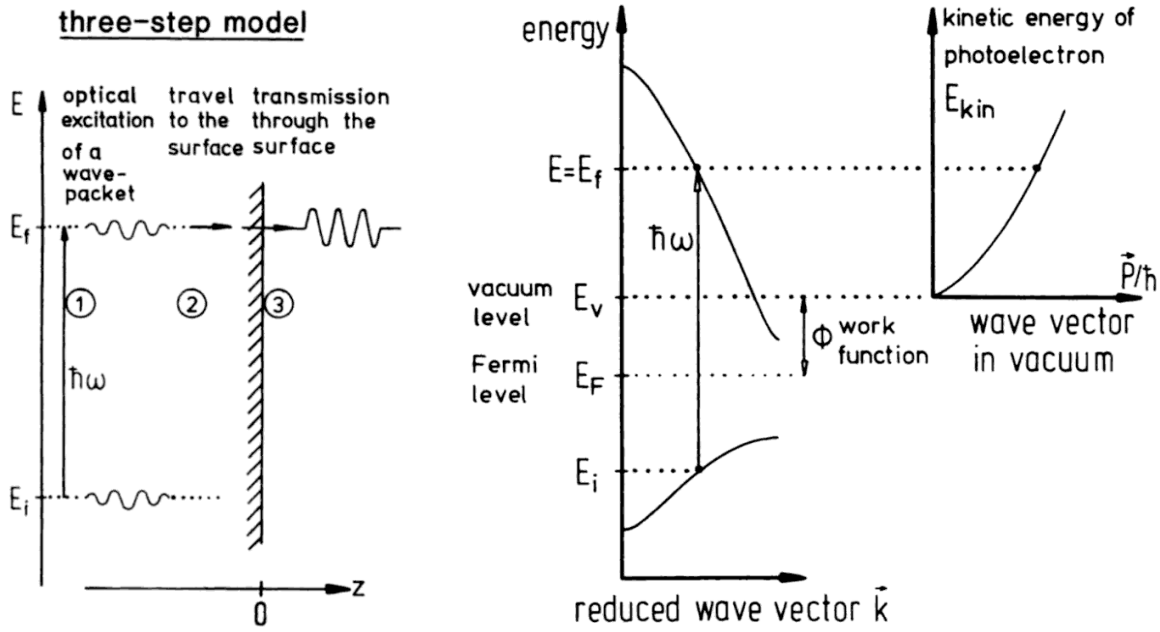

Figure 2.5: (Left) Three-step model of photoemission. (Right) Excitation within the reduced zone scheme. Figure adapted from Ref. [6].

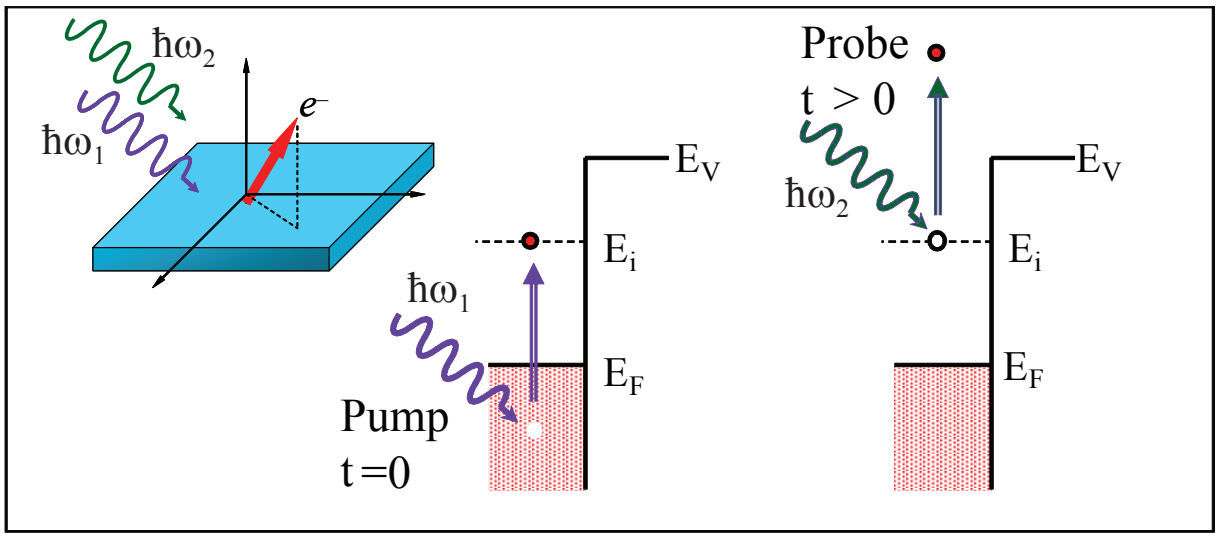

Figure 2.6: Excitation process for two-photon photoemission. A photon of energy $\hbar\omega_1$ is absorbed by an occupied state electron at time $t = 0$. The electron makes a transition from a bound state below E_F to an intermediate state with energy E_i, where $E_V < E_i < E_F$. At a later time a second photon of energy $\hbar\omega_2$ excites the electron to a free state above the vacuum level.

below the Fermi level is pumped to a bound, unoccupied state of the crystal, before being excited above the vacuum level by absorption of a second photon. After excitation to a free state in the vacuum, the detection process is identical to that of single photon photoemission. Since the process is, by definition, a second order process, high photon fluxes are required in order to acquire a good signal-to-noise ratio. Additionally, low photon energies are needed for the pump pulse since the total energy of the pump must be less than the work function to avoid ejecting electrons directly into the vacuum. For this reason, pulsed laser photon sources are used for 2PPE. Pulsed laser sources are also naturally suited to making time-resolved measurements. If the first pulse has a different energy than the second pulse (bichromatic 2PPE), a time delay can be introduced between the pump and probe pulses which can be exploited to measure ultrafast dynamic effects[40, 41, 42, 44, 45, 46, 47].

While a number of condensed-matter systems have been examined using 2PPE, the technique has been used most fruitfully for the study of the electronic-band structure of normally unoccupied image and related surface states on metal surfaces [23, 38, 39, 20, 40, 41, 42, 44, 45, 46, 47]. In addition, the use of time-resolved capability, which is inherent to 2PPE measurements, enables direct determination of ultrafast quasiparticle inelastic decay and thus the measurement precision of scattering in image states has developed to be of the order of several femtoseconds [40, 41, 42, 44, 45, 46, 47]. The technique of 2PPE has even been successfully applied to probe empty bulk states, which are inaccessible to photoemission spectroscopy [48, 49, 50, 51, 52, 53]. The signals from such bulk states are relatively weak in comparison to image and molecular states because of their relatively short lifetimes, which are dominated by electron-electron scattering[53]. More recently, 2PPE has been used to map the unoccupied bulk states in the vicinity of the L-point below the vacuum level[53]. Finally, entirely new and potentially very powerful applications of time-resolved 2PPE have also been demonstrated, such as detection of periodic motion of electron wave packets [54], motion of adsorbate atoms [55], coherent control of currents[56], hot electron dynamics[57], plasmon dynamics[58, 59], and dynamics of electron transfer, localization, solvation, as well as polaron formation[60, 61, 62, 63, 64, 65].

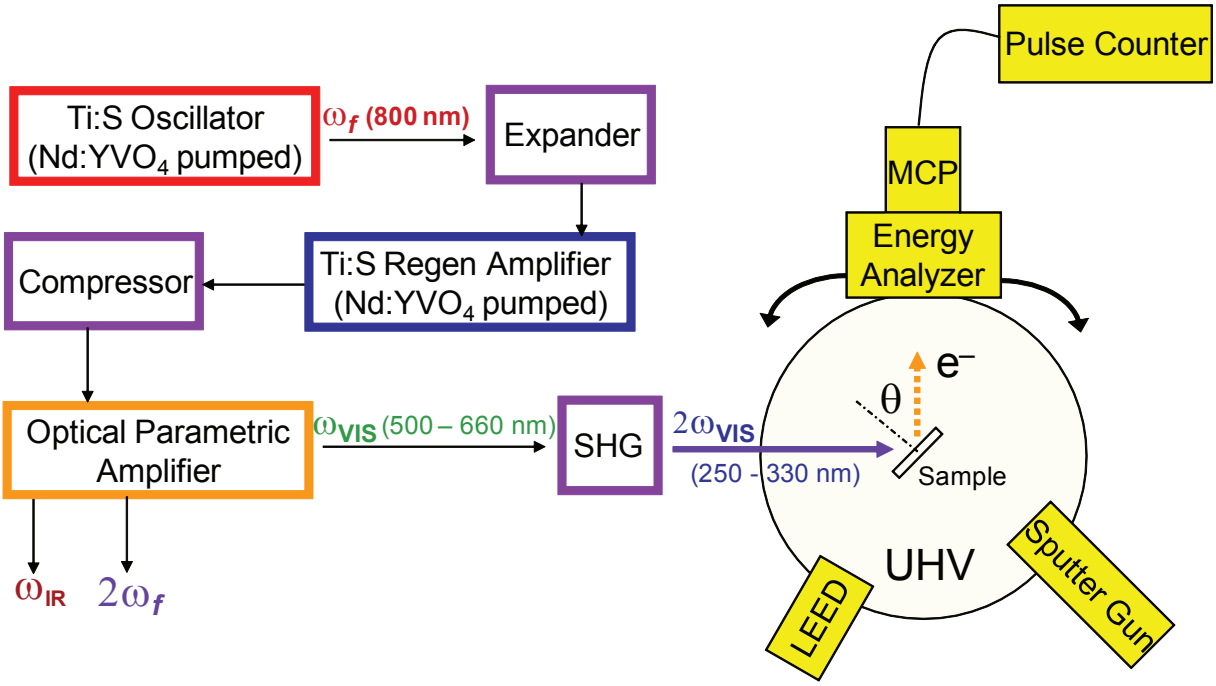

Figure 2.7: Femtosecond laser system and vacuum system.

2.3.4 Experimental Setup for 2PPE with Femtosecond Laser System

The setup used to collect the 2PPE data described in this dissertation is diagrammed in Fig. 2.7. The laser system uses an ultrafast Ti:Sapphire pulse source, the pulses of which are amplified in a regenerative amplifier, and then used to drive an optical parametric amplifier to provide a tunable source of visible light. This output is then converted to UV wavelengths by second harmonic-generation in a 1 mm BBO crystal, thus producing a train of 90 fs tunable UV pulses. The range of available wavelengths is $\sim$ 340 - 250 nm, which corresponds to a photon energy range of 3.6 - 5 eV. The laser has a 250 KHz repetition rate and produces pulses with total energies of the order of 1 nJ. The UV wavelength is determined using a 0.25 m monochromator with a wavelength accuracy of about $\pm$ 1 nm corresponding to $\pm$ 20 meV error in the UV photon energy.

Photoemitted electrons are collected using a 160° (36.5-mm radius) spherical-sector energy analyzer. The acceptor cone of the detector yields a momentum resolution of $\delta\ k_{\|} = 0.03\text{Å}^{-1}$; the energy resolution was set to $\sim$50 meV, a value greater than the energy res-

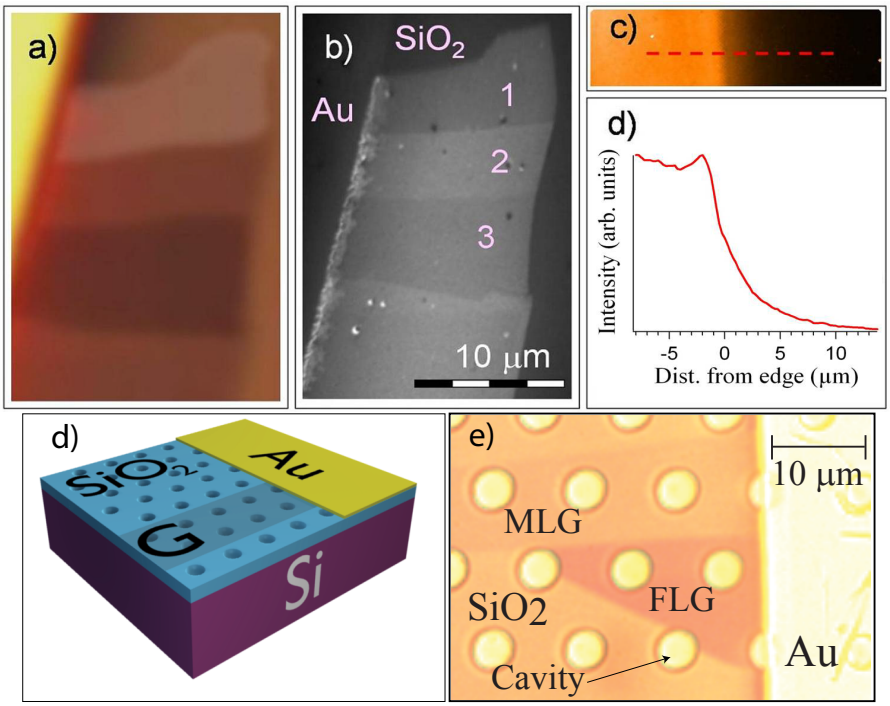

Figure 2.8: Supported and suspended graphene samples (a) Optical microscopy image of monolayer and multilayer supported graphene sample. (colors enhanced to show contrast). (b) LEEM image of the same sample. Numbers indicate graphene thickness in ML. (c) XPEEM image of Au 4f 7/2 core level taken at edge of Au wire on graphene. (d) Intensity profile along red dashed line in (c). (d) Schematic of suspended-graphene sample configuration. (e) Optical micrograph of sample containing suspended monolayer graphene (MLG) and few-layer graphene (FLG).

olution limit of the short optical pulse of $\sim$ 20 meV bandwidth. The laser incidence was fixed at 70° and the angular resolution was achieved by rotating the detector about a fixed sample.

2.4 Sample Preparation

2.4.1 Graphene Sample Preparation

Graphene samples were extracted by micro-mechanical cleavage from Kish graphite crystals (Toshiba Ceramics, Inc.) and placed onto an SiO_2-thin-film layer on an Si substrate using the standard micro-mechanical exfoliation technique[9]. The suspended graphene samples

were obtained through the use of a patterned substrate, in which cylindrical cavities 5 μm in diameter were etched to a depth of 500 nm. A sketch of the sample configuration is shown in Fig. 2.8 along with an optical micrograph. Great care was taken to eliminate any source of surface contamination during sample preparation, ensuring that the graphene surface under study was pristine. In particular, no photo-lithographic patterning techniques were used on the graphene sheets. To avoid charging the substrate under photon and electron beam irradiation, the graphene flakes were grounded by Au/Cr stripes evaporated through a metal shadow mask. Prior to the experiments with the electron microscope, all samples were inspected with an optical microscope to identify the thinnest flakes [66].

After preparation the samples were placed into a UHV chamber with a base pressure of 2×10^{-10} mbar, and the surface cleaned via low-energy electron irradiation to eliminate adventitious hydrocarbon molecules adsorbed during prior atmospheric exposure[67]. XPEEM with 403 eV photons was employed to examine the graphene sheets for impurities that may have been introduced in the preparation procedure. Traces of Au contamination from shadow masking during contact formation were measured only in the immediate proximity (within 5 μm) of the Au strips (see Fig 2.8). For each sample, LEEM was used to locate sample areas of interest and to determine film thickness with atomic resolution by measuring intensity modulations in the LEEM I-V spectra.[67, 68, 69]

Several experiments were carried out to determine the best surface preparation procedure for the graphene. It was found that prolonged UHV annealing at 300 C° resulted in degradation of the graphene LEED pattern, possibly due to the oxidation of the graphene due to the interaction with the underlying SiO_2-substrate [70]. Further, XPEEM measurements showed that heating caused diffusion of Au and Cr across the graphene from the nearby grounding stripes. These two problems prevented us from cleaning samples by annealing. Electron stimulated desorption of the adspecies was chosen instead for *in situ* surface preparation. In fact, irradiation at room temperature with low-energy electrons (in the range 25 to 150 eV) was found to result in a rapid increase in the intensity of the LEED patterns of both graphite and graphene flakes. The samples were locally irradiated until the elec-

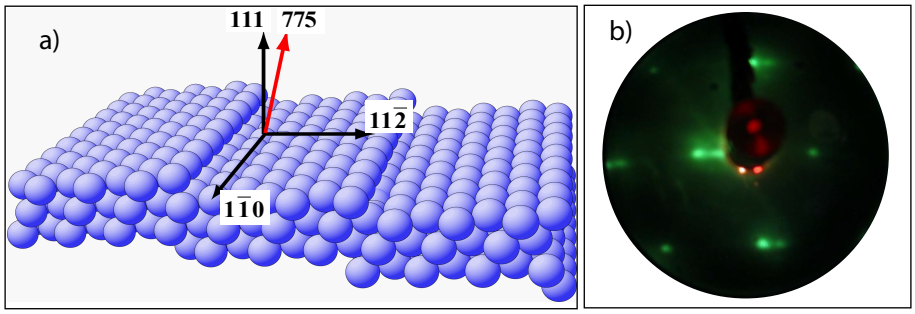

Figure 2.9: (a) Sketch of well ordered Cu(775). The terrace width is 14.02 Å and the sample cut is such that the step descends along the [11$\bar{2}$] direction. (b) LEED pattern at 65 eV of Cu(775) surface illustrates splitting of diffraction spots.

tron reflectivity of the Bragg reflection at 60 eV reached maximum intensity, typically in $\sim$ 30 mins. As we chose not to treat the samples thermally, we cannot exclude the presence of impurities, carbonates in particular, on the films. Comparative LEEM experiments were also carried out on HOPG; these experiments verified that irradiation with 60 eV electrons produced very sharp LEED patterns and led to the development of clean areas as large as 1 μm. The experiments on HOPG also showed that after e-beam irradiation some degree of contamination remained in the form of islands nucleated at steps, step bunches or other surface defects.

2.4.2 Cu(111) and Cu(775) Sample Preparation

In our experiments, a high-purity (99.999% purity) single-crystal copper sample of 1.2-cm diameter is cut to the desired (111) and (775) orientations on opposite sides of the crystal. The 8.5 ° miscut of the (775) surface with respect to (111) is accurate to within 0.1 degree. The sample, with both flat and stepped surfaces accessible, is then placed into a UHV chamber (base pressure less than 2×10^{-10} Torr) equipped with an ion sputtering gun, a low-energy electron diffraction (LEED) instrument, a quadrupole mass spectrometer (QMS), and a spherical-sector electron-energy analyzer. The sample is prepared by Ar+-sputtering at 2 keV for 20 min and subsequent annealing to 500 ° C. Each sample-preparation cycle is repeated until sharp LEED spots are observed. On the Cu(775) surface, the procedure is

repeated until the LEED spots are split to indicate high step regularity as shown in Fig. 3.1. Prior to each experimental run, the samples surface is "re-prepared" 2-3 times, as required.

Chapter 3

Measurements of the Surface Morphology of Graphene

3.1 Introduction

The transport properties of graphene depend strongly on the quality of its crystalline lattice, the presence of defects and dopants, and charge transfer from adsorbed or bound species [1]. Changes in conductance due to molecular adsorption are large enough to permit the detection of individual gas molecules by a graphene sensor [71]. Crystal deformations, due to either intrinsic thermal fluctuations or interactions with the substrate, largely contribute to electron scattering [71] and any attendant decrease in conductivity and carrier mobility [72, 73, 74]. In addition, corrugations and defects are expected to affect the chemical properties of graphene. Theoretical studies show that surface defects and bonding irregularities can lower reaction barriers [75]. Extrinsic ripples and curvature can in fact produce structure distortions showing domains of lower than hexagonal symmetry [76]. Such domains can exhibit admixture of sp^2 and sp^3 C orbital character and π orbital misalignment, which in carbon nanotubes are known to lead to increased reactivity [77]. Thus, techniques which lead to the control of topographic or morphological defects can play an important role in improving the properties of graphene for applications. For instance, ultrahigh electron

mobility was recently achieved in suspended graphene [78] and attributed to the concurrent effects of reduced contamination, the absence of interaction with the substrate, and the decreased surface corrugation.

Considerable experimental and theoretical effort has recently been dedicated to issues related to the morphology of single-layer graphene, addressing in particular the origin of any intrinsic corrugation and its relationship to crystal stability. In one of the earliest of such experiments, transmission electron microscopy revealed that both single- and double-layer suspended graphene display perfect crystalline structure in the short range, but are intrinsically corrugated in the long range, with deformations in the out-of-plane direction extending to a distance of 1 nm and a surface normal variation of 5° [79]. A recent experimental investigation has shown that long-wavelength ripples in graphene can be controlled by inducing mechanical or thermal strain [80]. However, it is believed that at finite temperature, even in the absence of applied strain, ripples at small wavelengths are present in graphene sheets. In fact, buckling in the direction normal to the lattice plane has been invoked to explain the stability of 2D crystals, as it serves to efficiently suppress long-wavelength phonons [16, 81, 82], which would otherwise cause lattice melting at any finite temperature, as demonstrated by the pioneering work of Peierls[14], Landau [13], and later by Mermin [15]. Recent theoretical studies confirm that the intrinsic corrugation in suspended graphene originates from thermal fluctuations and has a well-defined dependence on temperature [2, 83]. At sufficiently small length scales such corrugation is well described by the theory of flexible membranes in the harmonic approximation. At a critical wavelength, estimated to be 20 nm, anharmonic corrections, which couple the bending and stretching modes, become dominant and prevent the membrane from crumpling [2].

By contrast, corrugations measured in supported graphene are expected to be extrinsic in origin, arising from the interaction of graphene with the substrate. In particular, scanning probe experiments have shown corrugation wavelengths for supported graphene that are in the range of 10-30 nm [76, 84, 85, 86]. Analyses of the height-height correlation functions in such measurements indicates that graphene is smoother than the SiO_2 substrate [76]; this

arises because the energetic cost of elastic lattice deformation prevents the graphene film from conforming exactly to the substrate topography. In one study of supported graphene using STM, corrugation was reported with a preferential wavelength of 15 nm and attributed to an intrinsic effect [86], since it was not observed on the supporting substrate.

In this chapter, I describe an investigation of the corrugation in both freely suspended and SiO_2-supported exfoliated graphene layers. Our approach takes full advantage of the multiple techniques offered by a low energy electron microscope (described in detail in Chapter 2), to obtain a full characterization of the corrugation features in graphene. LEEM allows direct, real space imaging of the sample morphology over large surface areas (up to several tens micron), with lateral resolution of 10 nm and high structure sensitivity. In addition, this technique enables micro-probe low energy electron diffraction (μ-LEED) measurements that are restricted to a surface area of only a few square microns, thus providing access to the reciprocal space. Most importantly μ-LEED is sensitive to crystal deformations on length scales from $\sim$ 20 nm down to inter-atomic distances, thus complementing the real space images by providing additional information about corrugation at very short length scales. By combining these two electron microprobes, we are able to access both the microscopic and mesoscopic regimes, and thus the crossover length scale of both intrinsic and extrinsic corrugation.

3.2 Measurements of Graphene Thickness

An important aspect of our experiments is that LEEM can reach atomic depth sensitivity. This is possible in the presence of electron confinement in thin films, which determine a measurable modulation in the electron reflectivity between consecutive Bragg peaks at very low electron energy. Such intensity modulation, generally referred to as quantum-size contrast [87, 88], arises due to the formation of quantum-well resonances (QWRs). In the so-called phase accumulation model [88], QWRs are described by the Bohr-Sommerfeld quantization rule, which sets the condition for a resonance by the existence of constructive interference

between electron waves scattered at the film interface and at the surface:

$$2k(E)mt + \Phi_{surf}(E) + \Phi_{if}(E) = 2\pi n \tag{3.1}$$

Here, $k(E)$ is the perpendicular wavevector of an electron in the film, E its energy (relative to the Fermi level), t is the inter-layer distance, m is the film thickness (in monolayers), $\Phi_{surf}(E)$ and $\Phi_{if}(E)$ are the energy-dependent phase shifts for reflection of electrons at the surface and at the interface, respectively, and n is an integer. In the case of suspended graphene, $\Phi_{if}(E) = \Phi_{surf}(E)$, the phase shift for reflection at the vacuum interface. The same condition can be assumed to hold in the case of SiO_2-supported graphene, as the graphene film is known to be (partially) suspended on the substrate [86].

The phase condition described by Eq. 3.1 is analogous to that for a resonance in a Fabry-Pérot cavity and explains why the LEEM microscope can be effectively used as an electron interferometer for probing the thickness of ultra-thin films [89]. Equation 3.1 can be inverted to determine the existence condition for QWRs [90, 69]. In this way, one obtains a formula for the film thickness m, at which QWRs occur as a function of the allowed wave vectors $k(E)$, and the quantum number, ν:

$$m(E,\nu) = \frac{\left[\Phi_{surf}(E) + \Phi_{if}(E)\right]/2\pi + \nu}{1 - k(E)t/\pi}. \tag{3.2}$$

QWRs (and thus maxima in electron reflectivity) are found for $\nu = m - n$, with $1 \leq \nu < m$. Minima in reflectivity are found for $\nu = m - n - 1/2$. It has been shown that $m - 1$ quantum interference peaks, and thus $m - 1$ maxima and m minima in the electron reflectivity, are produced by a film thickness of m layers [87, 69].

Predictions for the energy of reflectivity maxima and minima were obtained with the phase accumulation model [69, 90], by imposing the condition for the film thickness m at which quantum-well resonances occur as a function of the allowed wave vectors k and the quantum number ν (see Eq. 3.2). In our calculation, the phase shifts upon electron reflection at the surface, which represents the leakage of the standing wave function beyond

the boundary, were assumed to be equal to 0. This approximation, which is essentially phenomenological, has been widely used in previous studies [69, 90]. The phase shift at the other surface plane was treated identically, as both terminating planes of the graphene films are in fact equal in the case of suspended samples. The same holds in the case of supported samples, because the interface is partially suspended and the interaction with the SiO_2 supporting substrate is minimal. Recall that the LEEM IV curves for suspended and supported samples are identical.

The function $k(E)$ was obtained by modeling the conduction band of graphite in the ΓA direction using the simple tight-binding scheme, *i.e.* $E = \epsilon - 2t\cos(ka)$, where ϵ is the energy of the band center, a is the interlayer distance and t is 1/4 of the bandwidth [68]. The electron energy E is referenced to the Fermi level and is given by $E = (E_{kin} - E_{vac}) + \phi$, where E_{kin} is the kinetic energy (often referred to as *start energy*) of the electrons impinging on the surface, E_{vac} is the vacuum level (obtained as the energy of the transition from LEEM to total reflection, ~ 0.75 eV in our case) and ϕ is the work function of graphite, *i.e.* 4.65 eV [91].

The band parameters (band minimum and maximum) were adjusted to optimize the fit with the experimental data. The curves shown in Figure 1, bottom-right, reproduce the position of experimental maxima and minima in electron reflectivity with very good accuracy. They were obtained with E_L and E_T equal to 5 and 10.4 eV (relative to the Fermi level). These values compare reasonably well with 4.4 eV and 10.7 eV, reported in a recent *ab initio* study on multi-layer graphene [68].

Fig. 3.1, top panel, shows a LEEM image of an area composed of graphene layers of different thicknesses on a SiO_2 substrate, each with a different grey-scale intensity. Characteristic LEEM IV spectra (obtained in bright-field mode, i.e. using the specular beam) from similar regions with graphene sheets ranging in thickness from 1 to 6 ML are shown in the lower left of the figure. Full and empty circles in Fig. 3.1, bottom-right, indicate the electron energies at which maxima and minima in electron reflectivity are observed, respectively. As can be seen, the predictions of the phase accumulation model obtained using

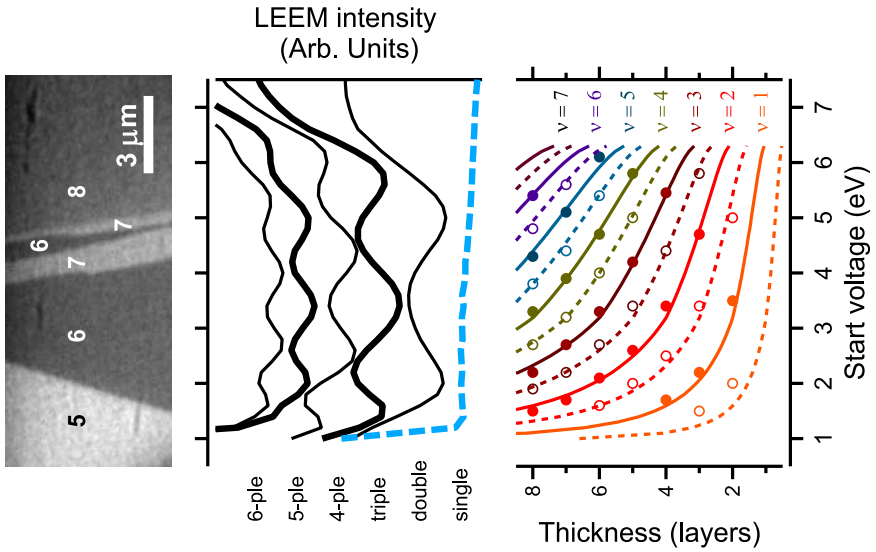

Figure 3.1: LEEM image of a multi-thickness graphene sheet supported on SiO_2; (bottom left) the LEEM IV spectra show the reflectivity modulations induced by quantum-well resonances. Single-layer (dashed line) and multi-layer (continuous lines) spectra are identified by the labels. (bottom right) The observed maxima and minima in electron reflectivity (full and empty circles) are compared to the predictions of the phase accumulation model (continuous and dotted curves respectively); quantum numbers are indicated on the right axis. More details are given in the Methods Section.

Eq. 3.2, represented by continuous and dotted curves in the Figure, match the experimental data closely. Details of the calculations are given in the Methods Section.

The intensity modulations in the IV spectra of exfoliated multi-layer graphene samples closely resemble the previously reported spectra of epitaxial graphene on SiC [68, 92]. The single-layer LEEM IV spectrum of SiO_2 supported graphene (dashed curve in Fig. 3.1, bottom left) is instead completely featureless. The identification of this featureless spectrum with single-layer graphene is confirmed by LEED measurements, which show a clear six-fold symmetry, in contrast to the threefold symmetry observed for multi-layer samples. As expected, no Bragg peaks were observed in the LEED IV spectrum of single-layer graphene. In fact, no such peaks can be seen for suspended or SiO_2-supported single-layer graphene, as the Bragg condition originates from constructive interference between waves scattered at different crystal planes.

3.3 LEEM imaging of graphene corrugation

Due to its high lateral resolution and thickness sensitivity, LEEM provides access to the local morphology of suspended and supported graphene samples. Figure 3.2 shows LEEM images of a large multi-thickness graphene flake on the SiO_2 substrate, into which micron-sized cylindrical cavities have been etched, as described in the Methods Section. The disks correspond to the suspended portions of the film. The variation in the local thickness of the film (indicated by labels in Fig. 3.2 A) becomes evident at an electron kinetic energy of 4.2 eV, due to the quantum-size contrast.

In all samples under study and for all thicknesses examined, the suspended portions of our samples appeared brighter in LEEM than those supported on SiO_2. This is consistent with the reduced intensity and broader width of the zero-order diffraction IV curves recorded on all SiO_2-supported samples (see Fig. 3.2). This type of contrast arises due to surface corrugation, because the finite angular acceptance of the microscope rejects e-beam reflections from surface planes tilted beyond the cutoff angle as determined by a contrast aperture[1].

[1]In the homogeneous field approximation the acceptance angle of the LEEM microscope is given by

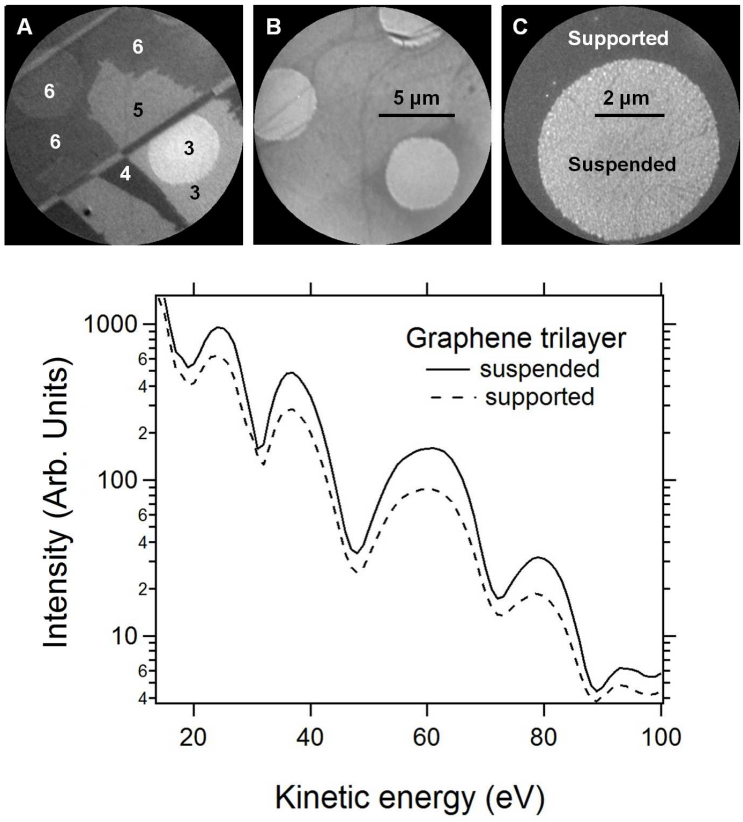

Figure 3.2: (A) LEEM image at 4.2 eV of suspended disks and SiO_2-supported graphene (disk diameter is 5μm). The local thickness in units of monolayer (indicated by labels) was determined by measuring the electron reflectivity curves in the energy interval 1 to 8 eV; (B) LEEM image of the same region at electron kinetic energy of 38 eV; (C) LEEM image of the suspended portion of single-layer flake at electron kinetic energy of 10 eV; (Bottom) Zero-order diffraction IV curves of SiO_2-supported and suspended tri-layer graphene.

Thus, a surface that scatters the e-beam over a wide range of off-normal angles will appear darker than a flat one, aligned normal to the beam. We note that this effect occurs even if the wavelength of the corrugation is below the lateral resolution of the microscope.

LEEM images at higher magnification show clearly the origin of the contrast difference observed between suspended and supported regions. High-lateral resolution images of single, bi- and tri-layer graphene are shown in Figs. 3.3 A-C. The higher reflectivity of the single-layer suspended disk (A) is due to the presence of large flat regions normal to the e-beam (appearing bright in the figure), which in some cases extend up to lengths of about 50 nm. These bright areas are fewer and smaller on the supported part of the film, but become larger on thicker samples. We observed that the patterns in Fig. 3.3 change when deflecting the angle of the e-beam illumination (not shown). As the incident e-beam is tilted, different surface planes become in fact visible. This behavior confirms that the contrast observed in LEEM arises from variations in the local surface normal of a static smooth surface.

The more pronounced corrugation observed in supported regions is very likely induced by the interaction with the substrate [76, 84, 85, 86] and therefore has extrinsic origin. Adsorbates are obviously another possible source of corrugation. It is in fact known that even small quantities of impurities can determine crystal deformation, as has been pointed out in a recent STEM study [93]. However, one should expect adsorbates to be distributed evenly on the graphene surface, resulting in no differences between the supported and suspended regions. Another explanation is that the corrugation of the SiO_2 support induces an increase in the local activity of surface sites which in turn causes the "pinning" of impurities.

Although LEEM is not sensitive to continuous height variations (in the present case, the image contrast is due to off-axis e-beam reflections) the LEEM images in Fig. 3.3 can provide real space information about the horizontal correlation length. The bright regions correspond in fact to "flat" areas, where local height variations are small and correlated. We underline that different bright regions may have different heights. Thus, the horizontal

$\alpha = \arcsin(r/f \cdot \sqrt{E/E_0})$, where E_0 is the kinetic energy (start energy) of the electron, E the high voltage applied to the cathode lens (18kV), f the focal length of objective lens (40 mm) and r the radius of the contrast aperture. At electron energy of 10 eV and contrast aperture of 30μm, we estimate an acceptance half-cone of 1.8°.

correlation length ξ (i.e. the distance beyond which height fluctuations are not anymore correlated) corresponds to the average size and distribution of the bright regions. We have estimated ξ by computing to the full width at height maximum of the central peak in the autocorrelation function on the intensity profiles taken across the LEEM images (see the lower part of Fig. 3.3). In this way, we find a value of 24 ± 0.3 nm and 30 ± 0.3 nm for single-layer supported and suspended graphene respectively, which increase to ~ 36 nm in the case of bilayer graphene. Our value of 24 nm for supported single-layer graphene compares favorably to previously reported correlation lengths measured by STM on SiO_2 supported graphene, which vary in the range 10 to about 30 nm [76, 84, 86].

Finally, we note that the high lateral resolution LEEM images in Fig. 3.3 A-C clearly show that the disk edges appear rough. This roughness, which is due to the imperfect edge definition of the etched well, indicates that graphene has the flexibility to conform to edge surface features at the 10 nm scale. In addition, a close examination of the images also reveals the presence of darker lines (resembling veins) extending across the graphene throughout the supported and suspended regions. As can be seen by comparing Fig. 3.2 A-B, these are not steps separating regions of different thickness. The origin of these features could be short wavelength wrinkles in the graphene membrane, in accord with similar observations reported in a recent STEM study [93].

3.4 LEED Measurements of Morphology of Graphene

Due to the intrinsic sensitivity of the line shape of diffracted electron beams to local height variations, micro-probe low energy electron diffraction (μ-LEED) was used to probe the roughness of SiO_2-supported and suspended regions of uniform thickness. In particular, μ-LEED measurements allowed us to access lattice distortions at length scales below the horizontal correlation length (a few tens of nm in single- and double-layer graphene), thus complementing the LEEM data presented in the previous section.

The most prominent feature that was observed in all graphene samples was the broad-

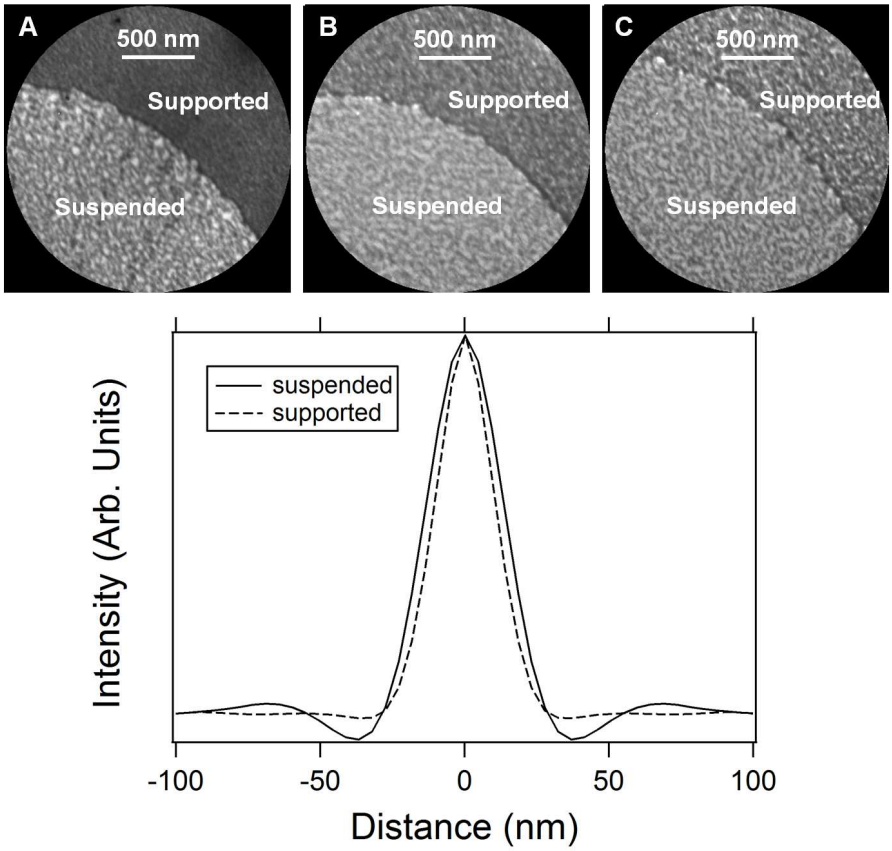

Figure 3.3: (A-C) LEEM images at 10 eV illustrating the morphology of suspended and SiO_2-supported graphene, at field of view of 2 μm: (A) single-layer, (B) bilayer and (C) trilayer suspended graphene disks and surrounding supported areas; (Bottom) Intensity autocorrelation function curves of the SiO_2-supported (dashed line) and suspended regions shown in (A).

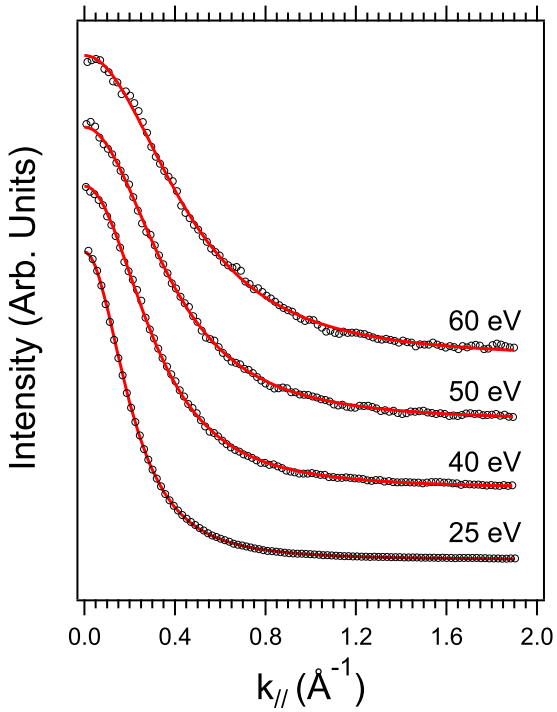

Figure 3.4: Profile across the (00) diffraction beam of single-layer suspended graphene at multiple electron energies. Multidimensional Lorentzian fits are shown as solid lines. See text for details. The curves have been offset for clarity.

ening of the diffraction profile with increasing perpendicular electron momentum transfer. Figure 3.4 shows profiles of the central diffraction beam of single-layer suspended graphene at multiple kinetic energies, together with best fits obtained using a multi-dimensional Lorentzian. This line-shape provides an excellent approximation to the expected diffraction line shape for rough surfaces (see the Supporting Information provided). The fit function was convolved with a Gaussian in order to take into account the response function of the instrument, which has a transfer width of 10 nm. This width is constant within the energy range of pertinence to this study.

Figure 3.5 shows the variation of the half width at half maximum (HWHM) of the (00) diffraction beam as a function of increasing perpendicular momentum transfer of the probe electrons, $k_\perp = (\mathbf{k}_{in} - \mathbf{k}_{out}) \cdot \hat{n} \cong 2\,|\mathbf{k}_{in}|$, for SiO_2-supported and suspended graphene (left and right panels in the figure, respectively). Each data point in the figure was obtained by

fitting the (00) diffraction beam with a multidimensional Lorentzian line profile, as shown in Fig. 3.4. As can be seen, film thickness and the presence of a supporting substrate have a significant influence on the evolution of peak broadening. We observe that peak broadening is always less pronounced in suspended than in supported samples. For example, suspended bi-layer graphene films show such narrow diffraction peaks that their widths are comparable to those of thick supported graphite films.

The broadening of the central diffraction peak with increasing $k_\perp$ is not observed on thick graphite films on SiO_2 (which are expected to be atomically flat) that have undergone the same preparation and cleaning procedure as that used for graphene (see the curve labeled TG in Fig. 3.5). For all graphite flakes the HWHM was less than 0.05 Å^{-1}, and nearly independent of $k_\perp$. This value is considerably smaller than that measured on SiO_2-supported and suspended single-layer graphene (≥ 0.45 Å^{-1} at $k_\perp$=8 Å^{-1}).

All curves in Fig. 3.5 show the presence of several sharp peaks in the width of the central diffraction beam (indicated by the dashed vertical lines in the Figure). In single-layer graphene, such peaks are observed when higher-order diffraction spots enter the Ewald sphere. For instance, at $k_\perp$5.8 $\text{Å}^{-1}$and $k_\perp\sim$ 9.7 Å^{-1}, the peak width of the zero-th order diffraction beam reaches distinct maxima, which correspond to a sharp decrease in the diffraction intensity due to the appearance of the first and second order diffraction spots, respectively. In multi-layer films, additional maxima in peak width can be observed at electron wavelengths that correspond to out-of-phase diffraction conditions, *i.e.* to maximum destructive interference between waves that are backscattered at the different layers. We observe that, under these conditions, the diffraction line shape cannot be described in a simple way as arising from local height variations of the graphene surface because other contributions to broadening may come into play (*e.g.* inelastic scattering, diffuse elastic scattering due to correlation between adsorbates or defects; we can exclude broadening due to the amorphous SiO_2 substrate, as no evidence of zero order diffraction can be observed on it). Therefore, data points corresponding to these values of $k_\perp$ were not considered in the analysis that follows.

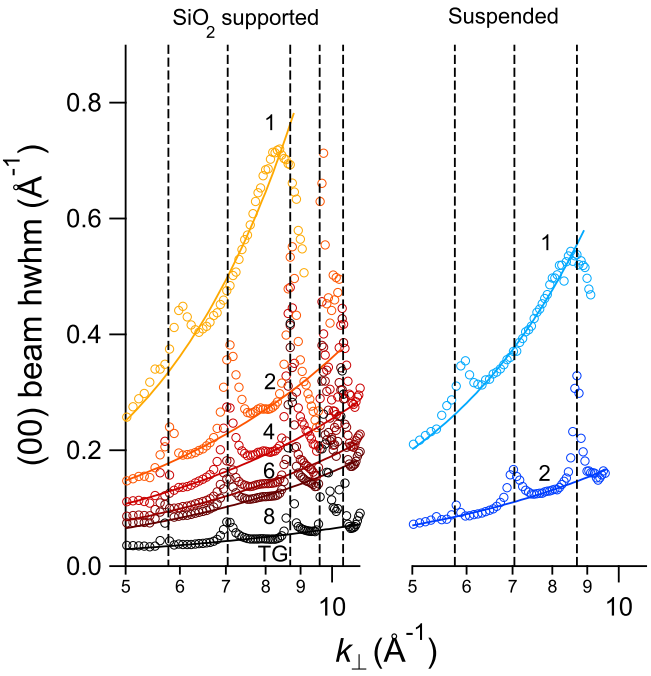

Figure 3.5: Variation of the (00) diffraction beam HWHM (circles) for different graphene films as a function of the electron momentum transfer $k_\perp$, measured at room temperature. The dashed vertical lines indicate resonances corresponding to out-of-phase diffraction conditions in multilayers. The continuous lines represent best fits using Eq. 3.3. The HWHM curves for SiO_2-supported and suspended graphene are shown in the left and right panels, respectively. The film thickness is indicated by the numeric labels; TG refers to thick graphite film on SiO_2.

3.4.1 Quantitative analysis of the short-range roughness in graphene

The analysis of the angular intensity distribution of diffraction data is a powerful investigative tool for characterizing surface disorder and roughness on a vast class of systems, including random, self-affine and mounded surfaces [94, 95, 96]. Relevant examples of application can be found in epitaxial growth processes [97, 98, 99, 100]. As will be shown below, LEED line-shape analysis allowed us to estimate an important parameter that is commonly used to quantify surface roughness, the *roughness exponent* α. This parameter describes the short range behavior of the height-height correlation function, which, below horizontal correlation length, scales as a power law with exponent 2α. In fact, α *measures* surface roughness. It ranges from 0 to 1: small (large) values indicate jagged (smooth) morphology on short length scales.

The data set presented in Fig. 3.5 allows us to determine accurately the dependence of broadening on momentum transfer, demonstrating that the zero-order diffraction width increases according to a power law (continuous lines). Deviations from linearity are small and become important only in the case of single-layer graphene. This behavior can be understood invoking the model developed by Yang, Wang and Lu [94, 95, 96], which describes the general principles of diffraction from rough surfaces (a summary of the model can be found in the Supporting Information provided). This kinematic model predicts that the diffraction line-shape, which is connected to the height-height correlation function of the rippled surface by a Fourier transform, can be expressed as a function of the parameters describing roughness on self-affine surfaces. For sufficiently large perpendicular momentum transfer $k_\perp$, the diffraction profile does not show a δ function character but becomes purely diffusive (*i.e.* broadened). This occurs when $\Omega \equiv (wk_\perp)^2 \gg 1$, where w, referred to as interface width, is the standard deviation of the surface height. [2] In this case, the HWHM of the zero-order diffraction scales according to a power law of the electron momentum

[2] For the range of electron energies used in our LEED experiments, $k_\perp \geq 5$ Å^{-1}; according to the literature, w varies in the range of few Å to 1 nm. Therefore, the requirement $\Omega \gg 1$ is readily satisfied.

transfer $k_\perp$[94]:

$$\text{HWHM } (00) = Z_g \eta^{-1} k_\perp^{1/\alpha} \tag{3.3}$$

Z_g defines the half width of the scaling function that determines the actual shape of the peak profile. The parameter η (roughness length) also describes roughness in the short range and is defined as: $\eta = \xi w^{-1/\alpha}$. From this definition, it follows that η is proportional to the average width of correlated areas (*i.e.* the flat regions in the continuously bent graphene film). Note that η is not dimensionless, but $\eta = [L]^{(\alpha-1)/\alpha}$ (where L is a length).

Rigorously, Eq. 3.3 is only valid for self-affine surfaces.[94] It is unclear whether graphene can be considered purely self-affine. In the case of thin supported films, self-affinity might be inherited from the SiO_2 substrate, to which the graphene partially conforms. Suspended as well as thicker supported films show different characteristics. The oscillatory behavior in the autocorrelation function observed in single-layer suspended graphene (see for example Fig. 3.3) suggests that the large wavelength ripples show a preferential periodicity, so that the surface can be more appropriately considered *mounded*. In this case the HWHM is expected to depend both on the correlation length and ripple wavelength [100]. However, we observe that, for sufficiently large values of the momentum transfer, diffraction theory predicts that peak broadening results from corrugations at length scales much smaller than the correlation length [96]. Thus, the effect of the surface curvature at large wavelengths can be neglected and Eq. 3.3 can be safely assumed to hold validity.

Experimentally, the roughness exponent α was obtained by fitting the data in Fig. 3.5 using Eq. 3.3. The data points corresponding to the out-of-phase diffraction condition were not included in the fit for two reasons: i) Other broadening contributions may become important, as anticipated; ii) one of the hypotheses that form the basis of Yang's model does not hold, and the model cannot be applied. Z_g was calculated numerically after finding α (see the supporting information), which allowed us to determine the short range parameter η. The values of α and η for suspended and supported graphene are shown in Table 3.1 as a function of film thickness. As can be seen, two distinct regimes can be identified corre-

Thickness (layers)	SiO_2-supported		suspended	
	α	η	α	η
1	0.49 ± 0.04	77 ± 20	0.54 ± 0.02	84 ± 11
2	0.80 ± 0.04	64 ± 6	0.80 ± 0.05	144 ± 25
3	0.80 ± 0.06	81 ± 14	0.82 ± 0.06	131 ± 24
4	0.77 ± 0.07	104 ± 28	-	-
6	0.80 ± 0.05	133 ± 25	-	-
8	0.80 ± 0.05	157 ± 25	-	-
TG	0.87 ± 0.07	327 ± 70	-	-

Table 3.1: The roughness exponent α and roughness parameter η as a function of film thickness for supported and suspended graphene at room temperature. TG stands for thick graphite films supported on SiO_2. η is in units of $[\text{Å}]^{(\alpha-1)/\alpha}$.

sponding to single- and multi-layer graphene. For single-layer graphene we measure values of α close to 0.5. This value is consistent with the roughness exponent of the height-height correlation function reported in two recent scanning probe studies [86, 76]. The rougher short-range morphology of single-layer supported graphene results from the interaction with the SiO_2 substrate, to which the graphene partially conforms [86]. Conversely, both in suspended and SiO_2-supported multilayers α saturates to ~ 0.8. Note that a similar value of α is observed even at bilayer thickness, which suggests that the increased stiffness of the bilayer is already sufficient to warrant a smooth short-range morphology. The smoother texture of supported multilayers is confirmed by the monotonic increase of η with film thickness [3]. This suggests that the films become progressively flatter with increasing thickness. Large values of η are observed in the case of suspended graphene even at bi-layer thickness, suggesting the presence of very large *flat* regions (namely areas over which the height-height correlation function is constant).

3.4.2 Effect of Adsorbates and Temperature Dependence

We now discuss the effect of electron and photon irradiation on the LEED peak width in suspended single- and bilayer graphene. As reported in the methods section, our samples

[3] A comparison of η values for different thickness is possible in this case because $\alpha \sim 0.8$ for all multilayer samples.

were treated using electron-stimulated desorption (ESD). Figure 3.6, left panel, shows the HWHM vs $k_\perp$ of single- and bilayer films, for different exposures to electron and photon beams. Empty circles (curves labeled A) indicate HWHM data that were acquired shortly after the standard preparation procedure used in this study, which corresponds to an irradiation time of 30 min with 60 eV electrons (see the methods section). The other curves (labeled B, empty triangles) were measured after much longer irradiations with electrons (about 3 hours and 30 mins, at energy > 10 eV) and photons (~ 50 eV, for about 1 hour). As can be seen, only suspended single-layer graphene displays a notable narrowing of the peak width after prolonged irradiation. Conversely, the HWHM curves of suspended bilayer disks do not differ appreciably before and after long irradiation. The LEED peak narrowing observed in single-layer graphene results from an increase in value of the parameter η, rather than that of α (see Table 3.2). Thus, we can relate the narrowing of the zero-order diffraction to the improved sample cleanliness that was achieved by ESD. We argue that the roughness may vary significantly as a result of small variations in adsorbate concentration, due to the reduced stiffness of single-layer films. This suggests that the corrugation in single-layer exfoliated graphene can be affected by adsorbates, and thus is, at least in part, extrinsic in origin.

In order to gain a more detailed understanding of the corrugation in graphene, we investigated the effect of temperature change on the LEED peak broadening in suspended single- and bilayer films. Contrary to bi-layer graphene, single-layer displays temperature-induced changes in the shape of the zero order diffraction peak. The effect of temperature on line broadening of single-layer graphene is shown in the right panel of Fig. 3.6, for short (A) and long (B) e-beam irradiation times. The curves at high and low temperatures were acquired after those at room temperature. As can be seen in both cases, a change in sample temperature leads to a noticeable change in the slope of the HWHM versus $k_\perp$. Peak-profile analysis shows that, independent of electron and photon irradiation time, the roughness parameter α increases with decreasing temperature (see Table 3.2), and reaches a maximum value of 0.64 at 155K. Thus, temperature induced changes in peak broadening can be clearly resolved

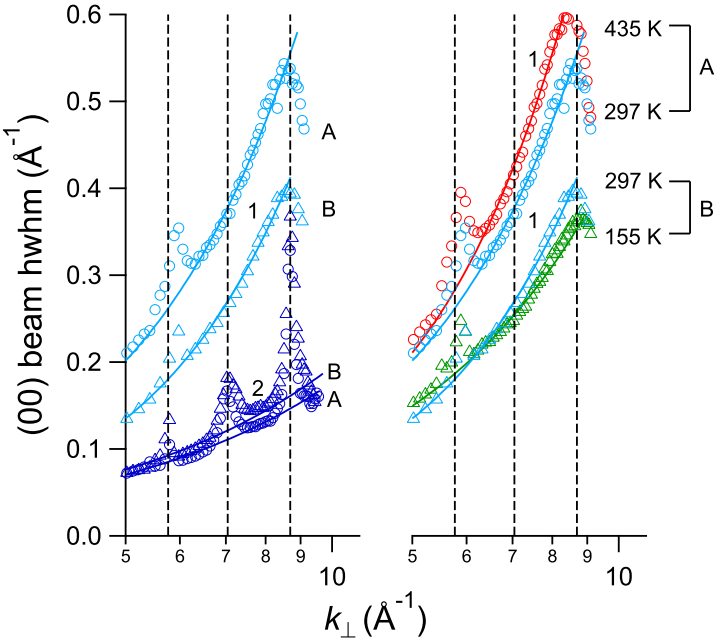

Figure 3.6: Left: variation of the (00) diffraction beam HWHM for single- (1) and bilayer (2) suspended graphene at room temperature, as a function of the electron momentum transfer $k_\perp$. The curves labeled A (empty circles) were measured after irradiating the film for 30 minutes with 60 eV electrons. Curves B (empty triangles) were measured after a longer irradiation (see text). Right: HWHM curves of single-layer suspended graphene at different temperatures, for different exposures to e-beam (A and B). Sample temperature is indicated by the labels.

from those induced by adsorbates, which affect η. The observed variation of α suggests that the film roughness decreases at wavelengths well below horizontal correlation length and coherence of the probe electron beam ($\sim$ 20 nm in both cases). In this instance, LEED peak narrowing is due to an increase of coherent scattering at short wavelengths, which we attribute to a reduced deformation of the lattice at low temperature.

It is important to note that the Debye-Waller effect is not expected to produce a broadening of the diffraction peaks. Increasing vibrational amplitudes, in fact, leave the average lattice constants unchanged, and therefore simply result in a decrease of the diffraction intensity [101]. Our results are in agreement with the theory of Fasolino *et al.*, which predicts

Thickness (layers)	Temperature (K)	short irradiation (A)		long irradiation (B)	
		α	η	α	η
1	435	0.49 ± 0.02	94 ± 11	–	–
1	297	0.54 ± 0.02	84 ± 11	0.50 ± 0.02	143 ± 23
1	155	–	–	0.64 ± 0.03	91 ± 11
2	435	0.73 ± 0.08	153 ± 50	–	–
2	297	0.80 ± 0.05	144 ± 25	0.74 ± 0.07	150 ± 50
2	155	–	–	0.78 ± 0.06	96 ± 19

Table 3.2: The roughness exponent α and roughness parameter η as a function of film thickness for suspended graphene at different temperatures and for different irradiations times: (A) irradiation of 30 min with 60 eV electrons. (B) irradiations with electrons (about 210 min, at energy > 10 eV) and photons (~ 50 eV, for about 1 hour). η is in units of $[\text{Å}]^{(\alpha-1)/\alpha}$.

that phonon-induced corrugations in graphene should occur on length scales below 20 nm. Such corrugations, which may be related to the different bond-lengths arising from the multiplicity of the carbon bond, display a well defined dependence on temperature [2]. In fact, in the harmonic approximation, the *rms* height variation across a flexible membrane scales with temperature as $\sqrt{T/\kappa(T)}$, where $\kappa(T)$ is the bending rigidity. A detailed comparison with theoretical predictions for the above functional dependence is impossible in our case, because of the interplay between intrinsic and extrinsic factors. We underline that the effect of temperature is smaller than that of adsorbates. This warrants the need of additional, detailed investigations in order to discriminate the different effects of temperature, adsorbate loading and substrate configuration.

3.5 Conclusion

LEEM and μ-LEED measurements were used to characterize the surface morphology, local thickness and crystal structure of suspended and SiO_2-supported graphene layers. Our results show clearly that the corrugation observed on supported graphene samples is quantitatively different than that observed on suspended samples. While the former is largely determined by the morphology of the substrate, the latter is influenced by intrinsic and

extrinsic factors. Supported graphene samples display a rough morphology at short wavelengths, up to a thickness of several layers. This corrugation decreases with increasing film thickness, as the stiffer multi-layer film becomes effectively suspended on the hills of the SiO_2 substrate.

Suspended samples appear significantly smoother in the short-range than those supported on SiO_2. For instance, bi-layer suspended graphene shows very narrow diffraction peaks, comparable to those measured on thick supported graphite films. The smooth short-range texture of suspended bilayer is confirmed by the high value of the roughness exponent (~ 0.8). Micro-probe diffraction measurements demonstrate, however, that suspended single-layer graphene films are still corrugated. The roughness exponent, ~ 0.55 at room temperature, is lower than that measured on multilayers. We note that the reduced corrugation of suspended graphene reported here correlates well with the significantly improved transport properties of suspended-graphene devices [78].

Most relevantly, our experiments provide evidence that the corrugation in single-layer suspended graphene is sensitive to adsorbate load and temperature variations. This behavior, which is characteristic of single-layer graphene, is determined by the very high flexibility of the crystal at this thickness. The weak temperature dependence of the diffraction line shape observed in single-layer disks points to a line broadening mechanism that is only partially phonon-induced, and thus intrinsic in nature, which supports the picture that thermal fluctuations produce deviations from planarity [2]. However, we underline that the most important contributions to corrugation in single-layer exfoliated graphene are extrinsic. Our results, in fact, suggest that interactions with physisorbed or chemisorbed species can cause significant changes in the surface morphology. We envisage that the ability to modify such corrugation, by means of temperature, boundary conditions, deposition or removal of host adatoms and molecules *etc.*, will be crucial in assuming further control of the transport properties of graphene, with important implications to the their future exploitation in practical devices.

Chapter 4

Measurements of the Band Structure of Exfoliated Graphene

4.1 Introduction

Angle-resolved photoemission spectroscopy (ARPES) is the experimental method that is most frequently used to probe the electronic structure of crystals. However, so far, the majority of ARPES studies of graphene have been conducted on epitaxial graphene, which has been grown on a variety of substrates such as SiC, Ru, Ni and Ir. [102, 8, 103, 104, 105, 106, 107, 108] Epitaxial graphene is ideal for photoemission experiments, but, due to the interaction between the epitaxial graphene monolayer and the substrate, the band structure is often distorted such that the Dirac point shifts away from the Fermi energy, thus changing the quasiparticle dynamics. In an effort to minimize the effect of substrate interaction on epitaxial graphene, recent ARPES studies have focused on several multilayer systems, such as intercalated graphite[109] and graphene grown on the C face of SiC. [110] These layered systems consist of multiple stacked graphene sheets that are substantially electrically isolated, thus resulting in an electronic band structure that mimics that of suspended exfoliated single-layer graphene. However, despite its scientific and technological importance, exfoliated graphene has been the subject of only a limited number of ARPES studies,[111, 106]

despite the fact that it remains the best choice for device physics, as it is easily backgated and has the highest measured mobility.[78]

Several obstacles impede measurement of the bandstructure of exfoliated graphene. One difficulty arises from the fact that available single-layer exfoliated graphene flakes are typically less than 20 μm in size, thus precluding the use of standard ARPES systems, which require samples to be several mm in size. Hence, most information regarding low-energy occupied states in exfoliated graphene has been obtained indirectly from electrical-transport measurements[11, 12] or directly by optical-probing techniques.[112, 113] These techniques examine the bandstructure generally within 1eV of the Dirac point and do not directly provide momentum resolution. For photoemission the limitation in size can be overcome by working with high lateral-spatial-resolution probes such as those available using spectromicroscopy.[114, 108] A second major impediment to photoemission studies is due to the fact that graphene is an ultrathin crystal. This ultrathin property has, in turn, two important consequences for photoemission studies. The first is the transparency of monolayer graphene to UV photons and photoemitted electrons, which causes a strong background photoemission signal if the monolayer graphene is in close physical proximity with a substrate.[111] The second is that exfoliated graphene is not atomically flat, but is known to deform locally, a result shown through AFM, STM, electron microscopy, and electron scattering results.[86, 76, 67, 84, 115] It has been argued that the deformation is due to the fact that monolayer-thick graphene has soft flexural modes leading to ready bending of the graphene. The presence of a supporting substrate or scaffold can, to a certain degree, stabilize height fluctuations in the graphene layer, but corrugations in the underlying supporting substrate are transferred in part to the graphene due to the reduced stiffness of this material. Additionally, intrinsic corrugations that cannot be attributed to interaction with the substrate were recently observed in supported graphene.[86] Further, in a recent low energy diffraction study, we demonstrated that even graphene suspended over etched cavities exhibits corrugation, which appeared to have been intrinsic in origin. [67]

Thus, in general, two dimensional crystals produced by exfoliation may show significant

local curvature, manifested as corrugation and ripples. This corrugation is known to affect not only the electronic and transport properties of the material, but can also have a major impact on photoemission results. In particular, the theory of ARPES was developed for single-crystal atomically flat surfaces and relies on the fact that momentum perpendicular to the surface is conserved in the photoemission process. On such perfectly ordered crystals the photoemission lineshape is directly related to the spectral function of the electronic state being probed, from which information about many-body physics can be extracted. The corrugation in thin sheets of layered materials breaks this symmetry and obscures the intrinsic many-body effects.

In this chapter, I present a systematic approach to account for such corrugation-induced broadening in ARPES on thin films. By combining photoemission results with detailed information about surface morphology obtained from prior electron-microscopy measurements[67] taken in-situ on the same samples the influence of corrugation on spectral broadening can be quantified. I go on to describe a method to discount the effect of surface corrugation from ARPES measurements to reveal the intrinsic many-body physics present in graphene. The results show that suspended graphene behaves as a marginal Fermi-liquid with an anomalous quasiparticle lifetime which scales as $(E - E_F)^{-1}$.

4.2 Experiment

The measurements used the Spectroscopic Photoemission and Low Energy Electron Microscope (SPELEEM) at the Nanospectroscopy beamline at the Elettra Synchrotron light source[24] described in detail in Chapter 2.

The SPELEEM instrument used to collect data has the important advantage of having a sufficiently high spatial resolution to guarantee that we are measuring a single crystal sample of monolayer graphene and that all of the measured spectral intensity is derived from a fully suspended region. This capability is necessary since the suspended regions are approximately 5 μm in diameter and, therefore, cannot be resolved with conventional

photoemission instruments, which employ spatial averaging techniques that collect data over surface areas of several square millimeters. The potential to combine both photoemission and electron scattering measurements is essential for this experiment since it allows us to measure bandstructure and surface morphology on the same samples.

ARPES data at multiple photon energies were obtained on the suspended areas of the graphene film. Only regions of uniform thickness were considered. In order to elucidate the role of surface corrugation and substrate influence, comparative experiments were also carried out on corresponding regions where the film was supported by the SiO_2 substrate. This surface has been recently carefully calibrated by prior STM and electron-scattering measurements. [76, 84, 86] In addition, ARPES measurements were made on Kish-graphite flakes that were present on the same substrates. As graphite is a well understood and commonly studied system, these measurements provided a useful point of comparison for our graphene measurements. Photoemission from graphite is, in some respects, similar to that from graphene because of the stacked-layer nature of the former. However, the physics near the Dirac point is significantly different owing to the fact that the multilayer stacking in graphite breaks the symmetry between A and B sublattices, which results in two dispersing branches, such that low energy excitations do not have the simple linear dispersion relation that is found for graphene.

4.3 Results

Photoemission spectra were measured from two samples with differing degrees of surface corrugation and substrate interaction, that is, on suspended and substrate-supported graphene; note that all ARPES data presented in this chapter are raw (*i.e.* unprocessed) unless explicitly stated otherwise. Previous LEED measurements have shown that the horizontal correlation length increases from 24 nm to 30 nm in measurements taken on supported and suspended samples, respectively.[67] In addition, ARPES data were collected at room temperature over the entire surface Brillouin zone (SBZ) from 0.5 eV to -8 eV (energy ref-

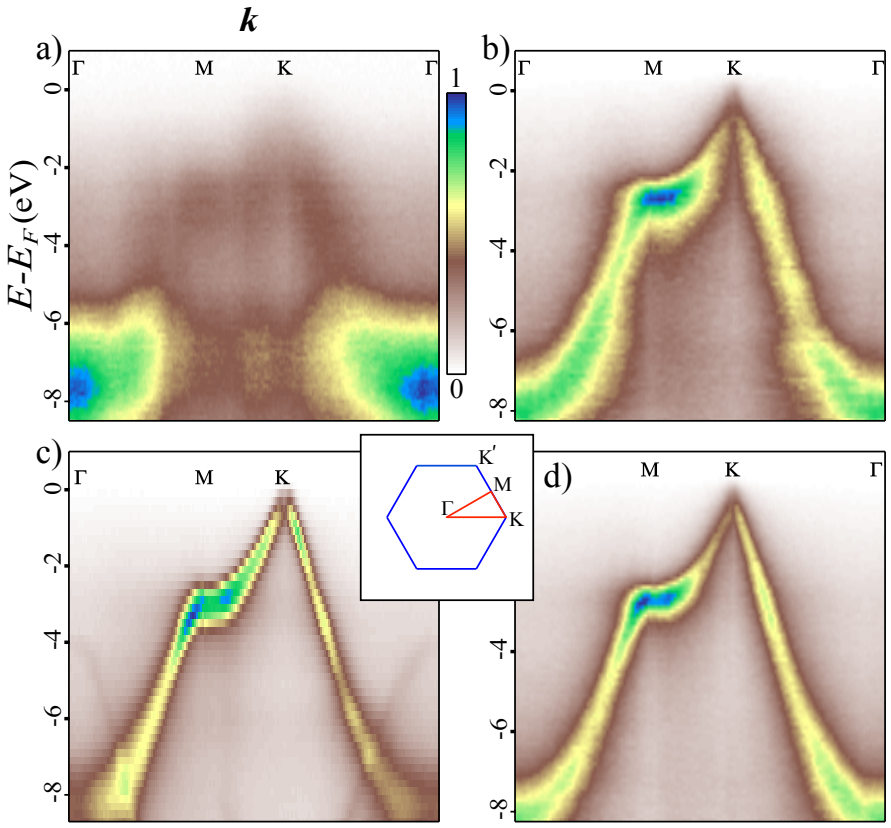

Figure 4.1: ARPES data along symmetry directions in Brillouin Zone for graphene and graphite. (a)SiO_2 supported graphene ($\hbar\omega$=90 eV). (b) Suspended graphene ($\hbar\omega$=84 eV). (c)Kish graphite ($\hbar\omega$=90 eV). (d) Suspended graphene ($\hbar\omega$=50 eV). Inset shows 2D graphene Brillouin zone.

erenced to E_F), for monolayer graphene and graphite, using a range of photon energies. Figure 4.1 shows ARPES spectra taken from a sample supported by and in contact with the SiO_2 surface and a sample that was suspended over the 5 μm wells shown in Fig. 2.8. For comparison, the ARPES spectrum from Kish graphite is shown as well. This data has been included to provide an example of the photoemission linewidth obtained by the SPELEEM instrument on a well known and related crystal system.

The data show dispersion along 3 symmetry lines in the SBZ. As expected from the reduced corrugation, as well as the absence of any substrate interaction, the ARPES data for suspended graphene show a dramatic improvement in quality as compared to the data for supported graphene. Additionally, there is a very broad, parabolically dispersing peak centered at the Γ point at a binding energy of $\sim$8 eV in the data taken on *supported* graphene. This feature has been previously attributed to photoemission from the amorphous SiO_2 substrate[111] and is not observed in the spectrum taken on suspended graphene. Although the substrate is only 300 nm below the suspended graphene, any background electrons emitted at this height will be significantly defocused in the electron optics of SPELEEM microscope. Additionally, due to the grazing incidence angle of the photon beam (16°), the bottom of the cavity is not fully illuminated. Thus, the cavity edge casts a shadow, which further reduces the photoemission signal from the substrate.

In the vicinity of the K points, a conical dispersion is observed centered at the K point on the suspended graphene spectrum. At $\sim$ 1 eV below the Fermi level a trigonal-warping deviation from angular isotropy becomes clearly noticeable. Measurements taken through the K point and in the direction parallel to the ΓM direction (vertical direction) show two symmetric dispersing branches forming the two sides of the Dirac cone. The band structure can be made significantly sharper (see Fig. 4.2) by taking the second derivative along each momentum direction. In this case, use of the second derivative allows easier determination of the Dirac point with respect to the Fermi level. Figure 4.2(b) shows the linear best fit to the two branches as well as the location of the Fermi level. From the fit, we find that the Dirac point is within 25 meV of E_F ($E_D = -9 \pm 25meV$). Thus, the sample is minimally doped

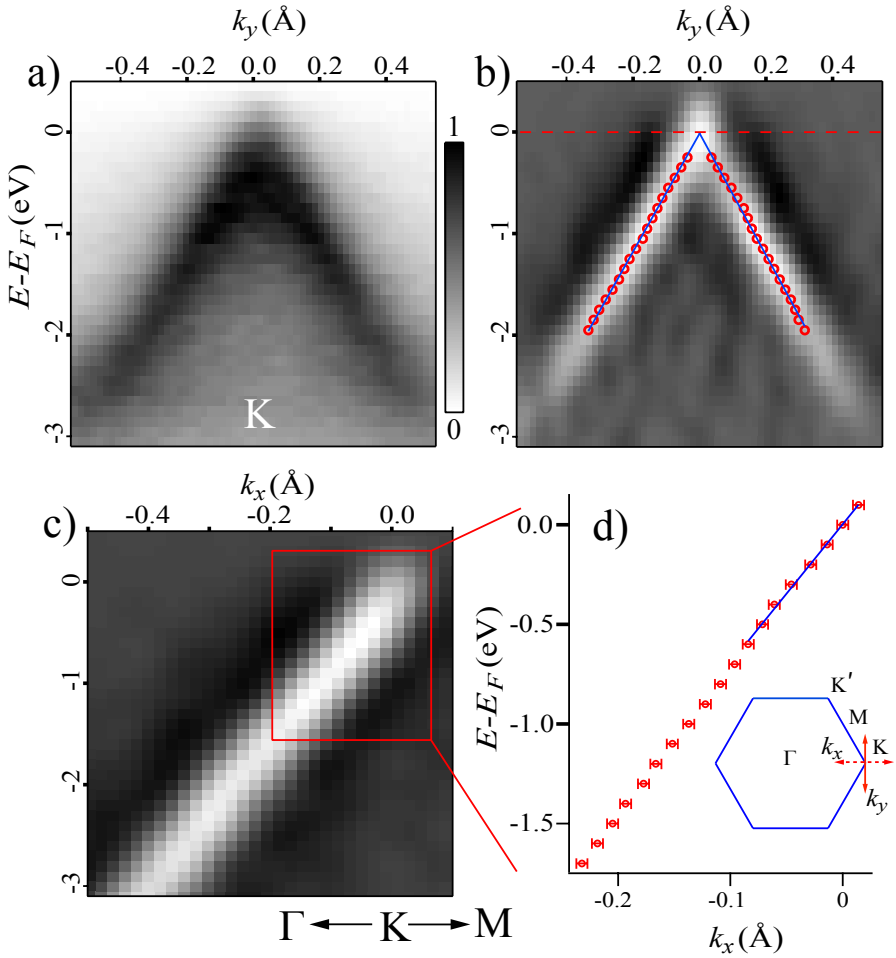

Figure 4.2: (a) ARPES intensity through K point along ΓM (k_y) direction in suspended monolayer graphene ($\hbar\omega = 50eV$). (b) Smoothed second derivative image of dispersion shown in (a). (c) Smoothed second derivative ARPES intensity through K point along ΓK (k_x) direction. (d) Extracted dispersion from (c) Inset shows graphene Brillouin zone. Red solid (dashed) line indicates k_y (k_x) direction through K point.

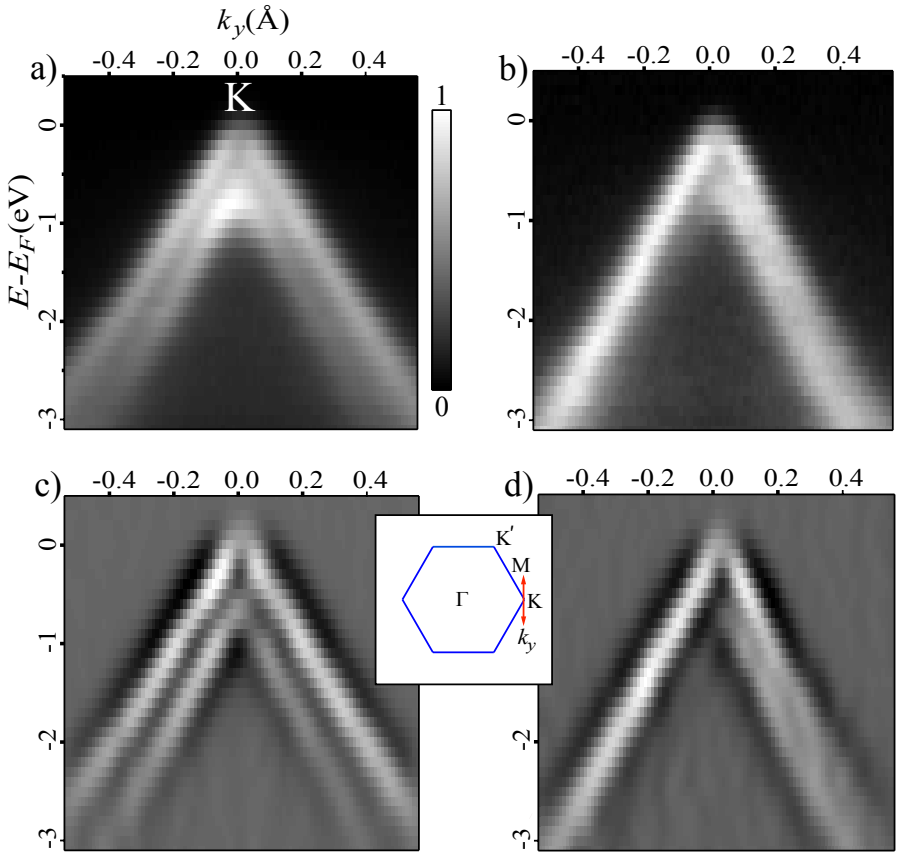

Figure 4.3: Dispersion along the vertical (k_y) direction through the $\bar{\text{K}}$ point for graphite obtained at photon energies of (a) $\hbar\omega = 86$ eV and (b) $\hbar\omega = 76$ eV. (c,d) Smoothed second derivative images of spectra shown in (a) and (b), respectively. Inset shows graphite surface Brillouin zone. Solid red line indicates k_y direction through $\bar{\text{K}}$ point.

due to the preparation procedure used here, which did not involve any photolithographic or chemical-transfer techniques. In contrast, the Dirac point previously measured by our group on a supported sample was found to be ∼300 meV below the Fermi level, which was attributed to doping by interaction with charged impurities in the SiO_2 layer.[111]

For comparison with results on a known photoemission materials system, graphite spectra were taken at two photon energies (86 and 76 eV) along the same (vertical) direction through the K point; these results are shown in Fig. 4.3. The dispersion obtained at $\hbar\omega$=86 eV is clearly symmetric about the K point. At this photon energy we can resolve the splitting of the π state into bonding and antibonding bands, with the two bands separated by

~ 0.12 Å^{-1}. The bands themselves are approximately 0.1 Å^{-1} in width. In the spectrum taken at 76 eV the two peaks are nearly degenerate. Again, the second derivative allows for easier determination of peak locations.

Figure 4.4 shows the graphene dispersion taken along the ΓK direction through the K point. Comparative measurements were made at two different photon energies ($\hbar\omega = 50, \hbar\omega = 84$) and are shown in Fig. 4.4(a) and (b), respectively. In this direction, only one branch of the dispersion can be seen as the difference in phase between electron waves emitted from the A and B sub-lattice sites results in complete destructive interference. [116] Thus, this is a convenient direction along which to measure precisely the dispersion in the vicinity of the Dirac cone. The inset to Figure 4.4(c) compares momentum distribution curves (MDCs) taken at a binding energy of 0.7 eV for the suspended-graphene spectra at both photon energies. The data in Fig. 4.4(c) show that the width of the $\hbar\omega$=84 eV MDC is significantly larger than the $\hbar\omega$=50 eV MDC (0.17 Å^{-1} vs 0.12 Å^{-1}).

Additionally, there is a slight asymmetry in all three MDCs as additional spectral weight is present on the right side of the peak (at higher values of k_x). The background signal decreases and the peaks become narrower for 50 eV photons as compared to 84 eV photons. Specifically, in the 0-4 eV range (referenced to E_F), the MDC width increases monotonically from 0.1 to 0.2 Å^{-1} and from 0.15 to 0.3 Å^{-1} for data collected with 50 eV photons and 84 eV photons, respectively. In contrast, MDCs taken along the same direction (ΓK) on supported graphene are significantly broader[111] and show almost no dependence on binding energy; they are $\sim$0.5 Å^{-1} in width from the Fermi energy to -4 eV binding energy. Thus, spectral features are sharpest for suspended samples measured with lower photon energy.

Referring, now, to data taken on the suspended sample, one obvious concern is that the dramatic increase in spectral features observed with increasing photon energy reflects an electron kinetic energy dependence in the momentum resolution of the instrument. However, as noted in Chapter 2, the instrumental resolution has been calibrated with a standard tungsten crystal and shown to increase by less than 5 % over a large range in electron kinetic energies (25 to 100 eV). This change in resolution is not sufficient to explain the $\sim$ 50 %

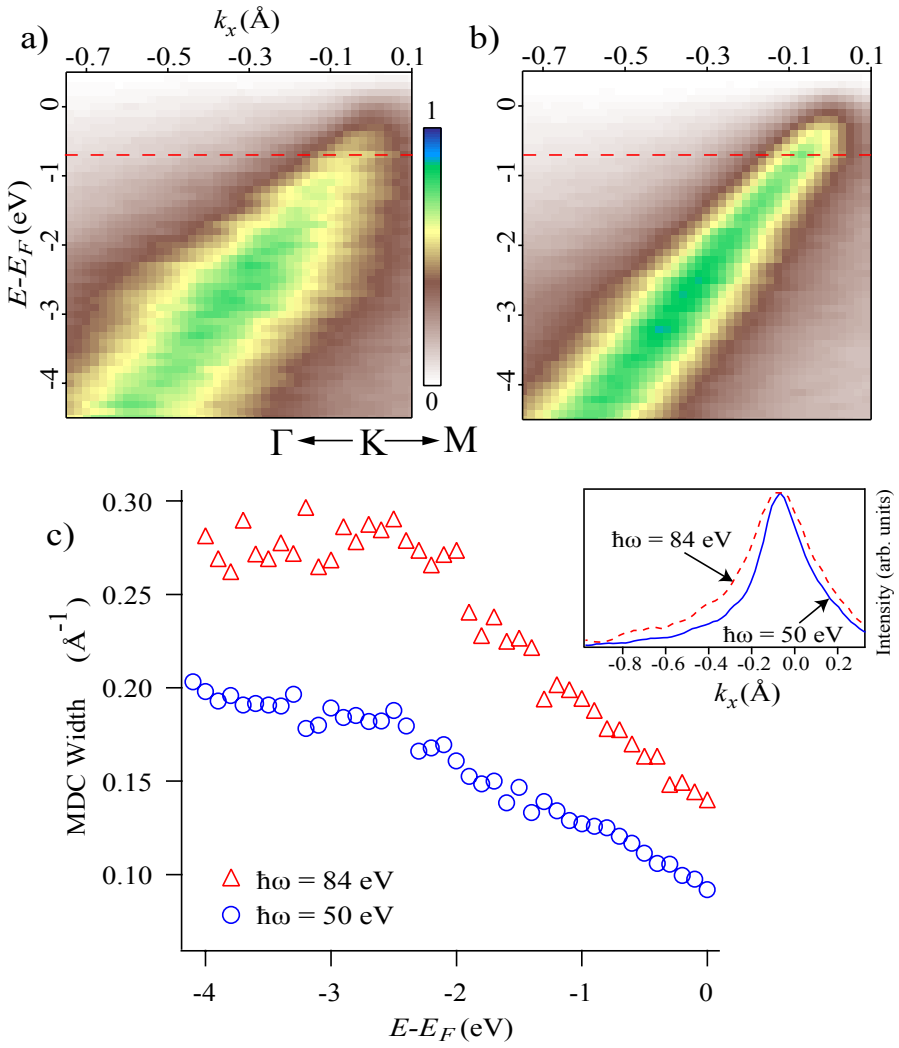

Figure 4.4: ARPES intensity along ΓK direction in suspended monolayer graphene. Graphene photoemission taken with photon energies of (a) $\hbar\omega = 84eV$ and (b) $\hbar\omega = 50eV$. (c) HWHM of MDCs as a function of binding energy taken from (a) and (b). Inset shows sample MDCs taken 0.7 eV below E_F as indicated by dashed red lines in (a) and (b).

increase seen in MDC width between data taken with 50 and 84 eV photons. Additionally, as noted above, one can clearly resolve features that are separated by less than 0.12 Å^{-1}in the graphite spectrum obtained with a photon energy of 86 eV.

4.4 Discussion

4.4.1 Comparison of Graphite and Graphene Results

As shown in Fig. 4.4, variation in photon energy results in changes to the linewidth of the graphene photoemission spectra, which can be exploited to sharpen the spectrum. In explaining these results on graphene, it is useful first to examine the effect of photon energy variation for *graphite*. The differences in the measured photoemission spectra of graphite taken at $\hbar\omega$=76 eV and $\hbar\omega$=86 eV shown in Figs. 4.3(a) and (b), respectively, are easily understood by considering the 3 dimensional band structure of graphite. In particular, according to the standard model of photoemission, variation in $\hbar\omega$ allows one to access a range of initial states with different k_z.[6] Using the free-electron approximation for the final state allows calculation of k_z of the initial state.[6, 117] Thus, in the case of the data shown in Fig. 4.3, photoemission obtained at $\hbar\omega = 86$ eV corresponds to $k_z = 0$ (the ΓKM plane), while $\hbar\omega = 76$ eV accesses $k_z = 0.3c^*$ which is nearer the AHL plane. Since k_z is changed, the clear double band feature seen for $k_z = 0$ changes as the graphite band structure varies along k_z in accord with the known graphite band structure. [116, 118, 119, 117]

Consider now the effect of changing photon energies for the case of graphene photoemission. Since graphene is truly a 2D crystal, the initial states in the valence band are highly localized along the z direction. Thus, the Brillouin zone is strictly 2D and the electronic structure is essentially k_z independent. Comparison with photoemission from surface states is useful, since they are also localized in 2D.[120] However, the role of evanescent decay into the bulk, which is important for surface states in metals and results in a partial k_z dependence,[120] such as surface resonance, is absent in graphene and, thus, we may treat the initial state as independent of photon energy. In fact, as seen in Fig. 4.4, changing

the photon energy in the case of graphene causes only a change in the overall linewidth and does not affect the measured bandstructure. As will be discussed below, the difference in the width of ARPES features between spectra obtained at $\hbar\omega$ =50 and $\hbar\omega$ =84 is a consequence of the surface roughness of the graphene samples. Since electrons in graphene propagate on a locally curved surface, the usual momentum conservation rules in ARPES must be modified and a photon-energy-dependent broadening term is introduced.

4.4.2 General Considerations

In standard many-body ARPES theory, the intensity of the photoemission signal is proportional to the spectral function, $A(\mathbf{k},\omega)$:

$$A(\mathbf{k},\omega) = \frac{\mathrm{Im}[\Sigma(\mathbf{k},\omega)]}{(\omega - \omega_{\mathbf{k}} - \mathrm{Re}[\Sigma(\mathbf{k},\omega)])^2 + \mathrm{Im}[(\Sigma(\mathbf{k},\omega)]^2} \tag{4.1}$$

where $\omega = E - E_F$ and $\mathbf{k}$ are binding energy and momentum, respectively, and $\omega_{\mathbf{k}}$ is the single-particle dispersion. The real and imaginary parts of the self-energy, $\Sigma(\mathbf{k},\omega)$, represent renormalization of the bare-bands and scattering rate, respectively. To obtain the full expression for the photocurrent, the above function is then multiplied by energy and momentum-preserving delta functions, $\delta(\mathbf{k}_i - \mathbf{k}_f - \mathbf{G})\delta(E_i - E_f - W)$, where $\mathbf{G}$ is a reciprocal lattice vector and i and f label the initial and final states, respectively, and W is the work function of the material.

However, one major complication to this approach arises for the case of suspended graphene since the momentum preserving function, $\delta(\mathbf{k}_i - \mathbf{k}_f - \mathbf{G})$, is only a precise delta-function if the system under investigation is atomically flat. While this is the case for the majority of single-crystal samples probed with ARPES, including the Kish graphite described above, exfoliated monolayer graphene, as is discussed in the Introduction, has significant deviations from planarity, ranging from 1 to 10 Å.[79] This corrugation introduces an additional broadening mechanism into the ARPES spectrum, which can be as large as, or larger than, the intrinsic broadening represented by $\mathrm{Im}[\Sigma(\mathbf{k},\omega)]$. Thus, in order to extract

the true self-energy of carriers in the crystal, such corrugation-induced broadening must be taken into account. The MDCs are best fit by a convolution of $A(\mathbf{k},\omega)$ with a function that represents broadening due to surface roughness. Thus, as will be shown below, at fixed ω, photoemission intensity as a function of $\mathbf{k}_\parallel$ can be expressed as:

$$I(\mathbf{k}_\parallel) \propto \int d^2\mathrm{k}_\parallel{}' S_{k_\perp}(\mathbf{k}_\parallel) A(\mathbf{k}_\parallel - \mathbf{k}'_\parallel, \omega) \tag{4.2}$$

where $\mathbf{k}_\parallel = \mathbf{k}_{i\parallel} - \mathbf{k}_{f\parallel}$ and $S_{\mathbf{k}_\perp}$ represents corrugation-induced broadening. $S_{\mathbf{k}_\perp}$, the surface structure factor, is a function of the surface geometry of the sample and is also generally dependent on the change in perpendicular momentum from initial to final state, $k_\perp = k_{i\perp} - k_{f\perp}$. We note that several prior studies have examined the effect of surface roughness on ARPES measurements.[121, 122] In these prior studies, the roughness considered was due to discrete height variations caused by monatomic steps, rather than the continuous undulations of a thin film. Thus, the broadening in spectral features measured by ARPES was attributed to increased electron scattering rather than a variation in the phase of photoemitted electrons induced by local height fluctuations. In our experiments on suspended graphene samples, the surface morphology is carefully measured simultaneously with the ARPES measurements presented here, thus allowing us to determine $S_{\mathbf{k}_\perp}$ independently.[27]

Finally, note that the surface corrugation of the graphene sheets will also alter the bandstructure by inducing a change in the local potential proportional to the square of the curvature. Thus, the ripples act as scattering centers, which will decrease lifetime and potentially change the Fermi velocity. These effects are contained in $A(\mathbf{k},\omega)$ and will also be present in the ARPES data. However, such effects are distinct from that described by $S_{k_\perp}$, which represents decoherence as electrons pass from a curved 2D space to free space.

4.4.3 Corrugation Broadening

Corrugation broadening can be treated by considering the equation that describes photoemission from a Bloch state in the graphene sheet into a free-electron state above the crystal.

Using the standard tight-binding approach to describe the initial state:

$$\psi_{\mathbf{k}}(\mathbf{r}) = \frac{1}{\sqrt{N}} \sum_{\mathbf{R}} e^{i\mathbf{k}\cdot\mathbf{R}} \sum_{j=A,B} C_j^{\mathbf{k}} \phi(\mathbf{r} - \mathbf{R} - \tau_j) \tag{4.3}$$

we obtain the following matrix element for excitation into a free electron final state:

$$M \propto (\mathbf{k_i} \cdot \hat{\lambda}) \sum_{j=A,B} C_j^{\mathbf{k_i}} e^{-i\mathbf{k_f}\cdot\tau_j} \sum_{R} e^{i(\mathbf{k_i}-\mathbf{k_f})\cdot\mathbf{R}} \tilde{\phi}(\mathbf{k_f}) \tag{4.4}$$

where $\mathbf{k_i}$ is the initial pseudo-momentum of a valence-band electron and $\mathbf{k_f}$ is the final-state momentum (for a full description and definitions of symbols see Appendix). Equation 4.3 describes an initial state with precise momentum at a fixed binding energy. For an atomically-flat crystalline 2D surface the position vectors can be expressed as $\mathbf{R} = n_1\mathbf{a}_1 + n_2\mathbf{a}_2$, where the n_i are integers and the $\mathbf{a}_i$ primitive lattice vectors in the xy plane. In this case, the sum over $\mathbf{R}$ in Eq. 4.3, $\sum e^{i(\mathbf{k_i}-\mathbf{k_f})\cdot\mathbf{R}}$, is zero unless $\mathbf{k_{i\parallel}} - \mathbf{k_{f\parallel}} = \mathbf{G}$, where $\mathbf{G}$ is a reciprocal lattice vector. This condition is, thus, a statement of the momentum conservation discussed above, $\delta(\mathbf{k_i} - \mathbf{k_f} - \mathbf{G})$. If, however, z is allowed to vary continuously as a function of position along the surface, so that $\mathbf{R} = n_1\mathbf{a}_1 + n_2\mathbf{a}_2 + \Delta x + \Delta y + z$[1], with z no longer constant, the summation in Eq. 4.4 is not as readily calculated. Perfect phase cancellation away from reciprocal lattice vectors does not occur, resulting in non-zero photoemission intensity when $\mathbf{k_{i\parallel}} - \mathbf{k_{f\parallel}} \neq \mathbf{G}$.

Summations such as the one in Eq. 4.4 are encountered in the theory of LEED on rough surfaces.[97, 98, 94] In fact, in many respects the formal analysis of LEED results bears many similarities to that of ARPES. In a prior study using one-photon photoemission and high-resolution LEED applied simultaneously to surface states of Cu(100) and Cu(111), it was demonstrated experimentally that the photoemission linewidth and the width of the LEED-spot profile are correlated linearly.[122] In particular, for LEED one measures the diffraction structure factor, $S(\mathbf{k}) \propto |\sum \mathbf{e^{ik\cdot R}}|^{\mathbf{2}}$ where, as in the case of photoemission, $\mathbf{k}$ is

[1] It is implied here that Δx, Δy and z are functions of position along the surface with z representing the local height of the surface and Δx, Δy representing deviations from the ideal lateral positions of surface atoms which are necessary to keep the average bond length unchanged.

the total momentum transfer, $\mathbf{k} = \mathbf{k_i} - \mathbf{k_f}$, and the sum is over atomic positions, $\mathbf{R}$, on a surface. In addition, for ARPES transition probability is proportional to the square of the matrix element; thus, the same structure factor, $S(\mathbf{k})$, is applicable. Thus, LEED theory can guide our analysis.

The structure factor, $S(\mathbf{k})$, can be calculated with information about the average properties of the surface, described by three variables: horizontal correlation-length, ξ, RMS height variation, w, and a dimensionless parameter, α, termed the "roughness exponent," which describes surface roughness on length scales smaller than ξ.[94] All three parameters can be extracted from real-space information about the surface by computing the height-height correlation function, which is used in a variety of thin film measurements, including those on graphene and other surfaces, and is defined as $H(r) = \langle |z(r_0 + r) - z(r_0)|^2 \rangle$. As is shown in the appendix, $S(\mathbf{k}) = S(k_\perp, \mathbf{k}_\parallel)$ is intimately related to $H(r)$ as the Fourier transform of $e^{-\frac{1}{2}k_\perp H(r)}$. Thus, the average parameters that characterize a given rough surface (w, ξ, and α) and determine the form of $H(r)$ also determine $S(k_\perp, \mathbf{k}_\parallel)$. Hence, with these parameters, it is possible to compute the summation in Eq. 4.4. In fact, previously reported measurements using low-energy electron microscopy and low-energy electron diffraction have determined these parameters to be $\alpha = 0.54 \pm 0.02$, $w = 1.99 \pm 0.15$ Å, and $\xi = 30 \pm 0.3$ nm for the same suspended graphene samples used in this study.[67] Although the functional form of $S(k_\perp, \mathbf{k}_\parallel)$ is complex, the width of $S_{k_\perp}(\mathbf{k}_\parallel)$ (i.e. for $k_\perp$ fixed) in $\mathbf{k}_\parallel$ space has a simple dependence on $k_\perp$ and the parameters describing the surface roughness. In particular, the width, Γ_S is proportional to $(k_\perp w)^{\frac{1}{\alpha}}/\xi$, which explains the decrease in experimental linewidth with decreasing $k_\perp$ shown in Fig. 4.4. For fitting purposes it is useful to have the exact functional form of $S_{k_\perp}(\mathbf{k}_\parallel)$. Yang, *et al.* have shown that for $(wk_\perp)^2 \gg 1$ the form is purely diffusive and can be expressed as:[94]

$$\begin{aligned} S_{k_\perp}(\mathbf{k}_\parallel) &= (\xi/(wk_\perp)^{\frac{1}{\alpha}}) F_\alpha(\mathbf{k}_\parallel \xi/(wk_\perp)^{\frac{1}{\alpha}}) \\ F_\alpha(Y) &= \int X dX exp(-X^{2\alpha}) J_0(XY) \end{aligned} \tag{4.5}$$

4.4.4 Intrinsic Broadening

It is straightforward to introduce intrinsic initial-state broadening into our ARPES description by replacing our initial state wavefunction, $\psi_{\mathbf{k}}$, with a sum over multiple momentum states, $\sum a_{\mathbf{k}}\psi_{\mathbf{k}}$, where the $a_{\mathbf{k_i}}$ are complex coefficients related to the spectral function by $|a_{\mathbf{k_i}}|^2 = A(\mathbf{k},\omega)$. Our transition matrix then becomes a sum, $M = \sum a_{\mathbf{k}} M^{\mathbf{k}}$, over multiple matrix elements weighted by the complex coefficients $a_{\mathbf{k}}$, where the $M^{\mathbf{k}}$ are the original transition matrix elements defined in Eq. 4.4. Again, using Fermi's golden rule we find that the transition probability is proportional to the square of this sum.

$$I \propto |M|^2 = |\sum_k a_k M^{\mathbf{k}}|^2 = \sum_{\mathbf{k}} |a_{\mathbf{k}}|^2 |M^k|^2 + \sum_{\mathbf{k}\neq\mathbf{k'}} a^*_{\mathbf{k}} a_{\mathbf{k'}} M^{\mathbf{k}*} M^{\mathbf{k'}} \tag{4.6}$$

As shown in the appendix the $\mathbf{k} \neq \mathbf{k'}$ sum can be safely neglected due to random phase cancellation and we arrive at the final expression for the full photoemission intensity expressed in Eq. 4.2.

Note that the broadening introduced by the surface corrugation of the suspended graphene sheet is *only* contained in the transition matrix element M^k. The many-body physics that describes the interaction of charge carriers in graphene with other excitations is contained in the complex coefficients $a_{\mathbf{k}}$. Thus, the "intrinsic" or initial state broadening referred to in this section, as well as subsequent sections, is the width of the spectral function derived from the complex coeffiecients, $A(\mathbf{k},\omega) = |a_{\mathbf{k_i}}|^2$.

Finally, we note that, in general, the linewidth (Γ_m) measured in ARPES from well prepared, atomically flat surfaces is a function of the initial state or photohole linewidth (Γ_i) as well as the linewidth of the final state or photoelectron (Γ_f). However, for the case of 2D states such as surface states in metals or thin films like graphene, there is no dispersion with $k_\perp$ and $\Gamma_m = \Gamma_i$.[123]

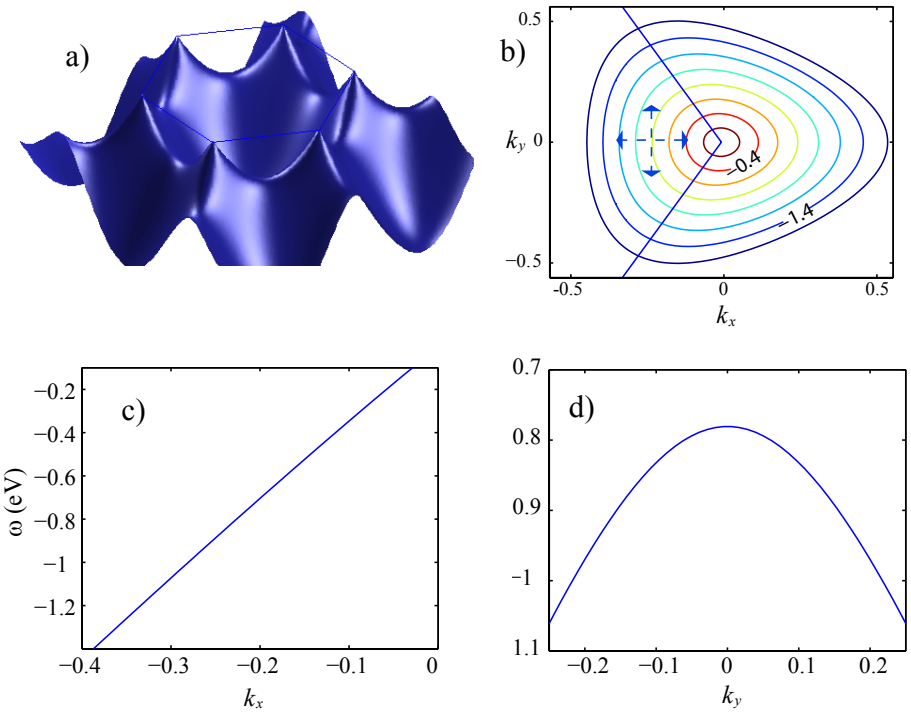

Figure 4.5: (a) Graphene bandstructure over first BZ. (b) Contour lines drawn along constant binding energies in the vicinity of the K point (binding energies indicated in eV). (c,d) Dispersion along k_x and k_y, respectively (along dashed blue lines in (b)).

4.4.5 Analysis of Spectra and Discussion

Figure 4.2 shows a plot of the dispersion obtained along the ΓK direction in the vicinity of the Dirac point. The average Fermi velocity, derived from the slope of ω vs k_x is $1.07 \pm 0.05 \times 10^6$ m/s. This value is obtained from an analysis of the dispersion in the energy range from 0 to 0.6 eV (see blue best-fit line in Fig. 4.2(d)). This value is in excellent agreement with results obtained by IR measurements on undoped supported exfoliated graphene.[124, 125] Additionally, the dispersion along ΓK is linear in this region (0 to 0.6 eV) with no deviations from linearity within our experimental uncertainty. As discussed above, despite the roughness-induced broadening in the spectrum, the dispersion curve is easily extracted from the raw ARPES data by taking the second derivative of the ARPES intensity along the momentum direction. However, determining the intrinsic width of spectral features requires a deeper analysis.

Our prior measurements of the surface corrugation in suspended graphene allow us to extract the intrinsic electronic structure from our ARPES data. The procedure for this fitting is as follows: first, $S_{k_\perp}$ is determined from our surface morphology measurements and used as a constant parameter, then $A(\mathbf{k}_\parallel)$ is varied until the convolved function, $I(\mathbf{k}_\parallel)$, represents a good fit to the experimental data. Although a full deconvolution is, in principle, possible, it is much more straightforward to begin with an assumption for the functional form of $A(\mathbf{k}_\parallel)$ and systematically vary the parameters until a good fit is found. The functional form of $A(\mathbf{k}_\parallel)$ is assumed to be a Lorentzian, the most commonly used photoemission lineshape, which results from the $\mathbf{k}$-independent approximation for $\mathrm{Im}[\Sigma(\mathbf{k}, \omega)]$.[2]

In carrying out this procedure, we introduce two additional simplifications. First, note that we are examining the region in $\mathbf{k}$-space within the first Brillouin zone along the ΓK (k_x) direction in the vicinity of the K point. As shown in Fig. 4.5, the π state disperses rapidly along k_x in this region, but relatively slowly along k_y since $\partial\omega/\partial k_y$=0 at k_y=0. Thus, al-

[2] In fitting the MDCs an instrumental broadening term was also convolved with our spectral function. The energy resolution introduces a width of $\Delta E v_F$. In combination with the lateral resolution of the instrument (known from prior calibration), this results in a Gaussian response function with a width of approximately 0.042 Å^{-1}.

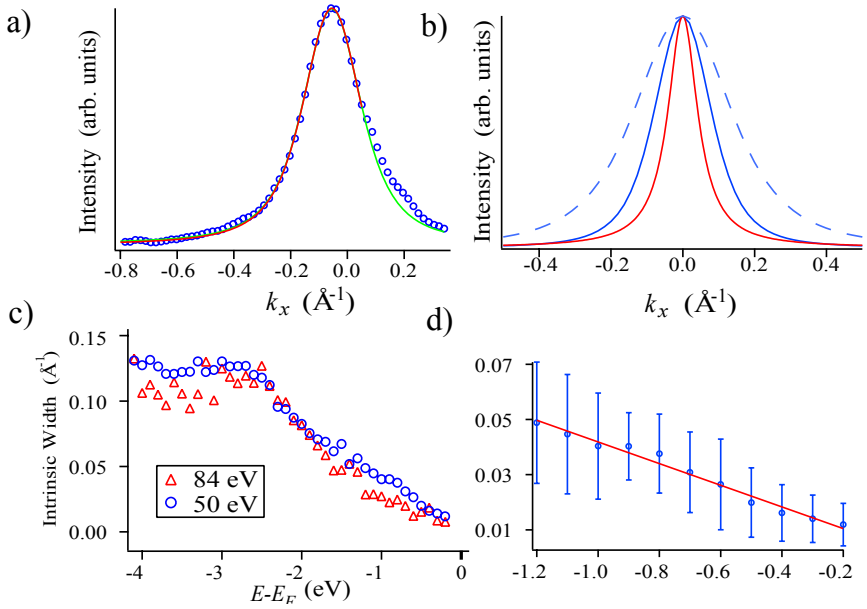

Figure 4.6: Intrinsic width of ARPES features for Suspended monolayer graphene. (a) Example of MDC fitting. (b) Two independent contributions to broadening. Red line: intrinsic linewidth of initial state. Blue line: broadening due to corrugation at $\hbar\omega$=50 eV (solid) and $\hbar\omega$=84 eV (dashed). (c) Inverse lifetime as a function of binding energy for $\hbar\omega$=50 (blue) and $\hbar\omega$=84 eV (red). (d) Best fit line to intrinsic width vs. binding energy for $\hbar\omega$=50 data in vicinity of Fermi level.

though Eq. 4.6 describes a 2D convolution, it is possible to replace the required 2D $k_x k_y$ integral with a 1D integral along k_x. Second, we note that most of the MDCs considered here have an asymmetric peak shape, with additional spectral weight in the $\omega > v_F|\mathbf{k}|$ region of the curve. Possible reasons for this asymmetry are discussed in a separate paragraph below. For fitting purposes, this additional spectral weight was not considered and the best fit was obtained by imposing a momentum cutoff within 0.1 Å^{-1} of the peak position on the $\omega > v_F|\mathbf{k}|$ side of the curve. Figure 4.6(a) shows a representative curve from the $\hbar\omega$=50 eV data taken 0.7 eV below the Fermi level along with a best fit. Note that the lineshape of this curve provides an excellent fit to the experimental data. Figure 4.6(b) shows the two independent contributions to the linewidth: the corrugation-induced broadening and the intrinsic broadening. In order to cross-check that the convolution procedure accurately captures the photon-energy dependence of the photoemission process, the same fitting procedure was repeated on data obtained with a photon energy of $\hbar\omega$=84. At this photon energy, $k_\perp = 4.27\text{Å}^{-1}$ and, according to Eq. 4.6, the width of $S_{k_\perp}$ is nearly twice as large as it is at $\hbar\omega = 50$ eV. However, as expected, the intrinsic linewidth extracted from the fitting procedure is the same for data obtained with both photon energies. A comparison of the self-energy extracted from the two data sets is shown in Fig. 4.6(c); the two resulting curves are the same, within experimental error, thus confirming the photon-energy dependence given in Eq. 4.6 and lending further support to our approach.

Comparison can be made to the theoretical work of Park *et al.* who compute, from first principles, the MDC broadening expected in an ARPES study of graphene [7]. Although their computation has been performed for doped graphene, their result for suspended graphene compares very favorably to ours. Figure 4.7 shows our result for the intrinsic MDC width along with the prediction of Park *et al.* for both freely suspended graphene and SiC supported graphene. As seen in Fig. 4.7(b), dielectric screening from the SiC substrate significatly reduces the MDC broadening. However, their result for suspended graphene is qualitatively similar to ours; they predict a monotonic increase in MDC width from 0 at E_F to $\sim$0.09 at 2 eV. However, care must be taken when comparing this calculation to our result,

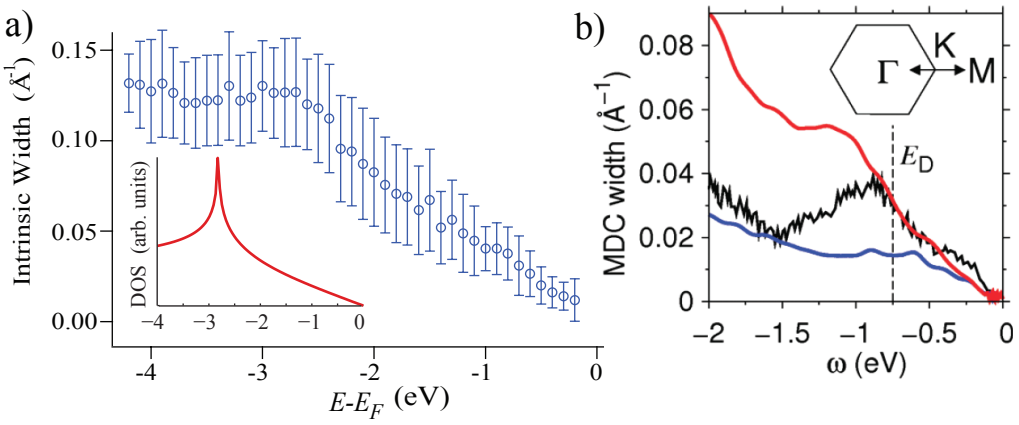

Figure 4.7: Inverse lifetime as a function of binding energy for $\hbar\omega$=50 (blue) shown with error bars. Inset shows graphene DOS. (b) Previous experimental and theoretical results for ARPES MDC width of graphene. Plot includes first principles calculation of Park, *et al.* [7] for suspended (red curve) as well as SiC supported (blue curve) graphene along with data from Bostwick, *et al.*[8] (black curve). Note that this data corresponds to *doped* graphene.

as the calculation has been performed for doped graphene, which changes the quasiparticle dynamics. For example, the kink observed in the 1 to 1.5 eV range is not present in our data. In comparison, our measured intrinsic linewidth increases linearly from E_F to $\sim$ 3 eV, after which it is constant at $\sim$ 0.13 Å^{-1}. The kink at $\sim$3 eV in our data corresponds to the rapid change in the density-of-states in graphene which occurs at a binding energy equal to the nearest-neighbor hopping energy of $\sim$2.8 eV (see inset to Fig 4.7).

To make our observations quantitative and enable comparison with other work, we perform a linear fit of the intrinsic width versus binding energy, $\Gamma_i = \alpha + \beta(E - E_F)$. From this fit, we find $\alpha = 0.002 \pm 0.005$ Å^{-1} and $\beta = 0.039 \pm 0.01$ Å$^{-1}eV^{-1}$. As expected, the value of α is within experimental uncertainty of zero since excited states just above the Fermi level should be very long lived. Consider now the parameter β that describes the increase in inverse quasiparticle lifetime with increasing binding energy. Ready comparison can be made to the theoretical work of Park *et al.* who compute from first principles the broadening expected in an ARPES study of neutral graphene [7]. Their result compares very favorably to ours. In particular, they predict a linear increase in the intrinsic MDC width from 0 to $\sim$ 0.05 Å^{-1} in the energy range from 0 to -1 eV, which corresponds to $\beta \approx 0.05$ [7].

The lifetime is related to Γ_i by $\tau = 1/(2\Gamma_i v_F)$. Thus, our measured value can be expressed as β= 0.78±0.02 fs^{-1} eV^{-1}, so as to enable ready comparison with prior measurements of the same quantity on graphite and exfoliated graphene. For graphite, β has been measured by femtosecond photoemission to be an order of magnitude smaller, viz. 0.029 fs^{-1} eV^{-1} [126], while STS measurements of exfoliated graphene on graphite have produced an intermediate value of (β = 0.11 fs^{-1} eV^{-1}) [127]. A reasonable explanation for this discrepancy is the greater out-of-plane corrugation of suspended graphene, which has been predicted to be the largest contribution to electron scattering in rough graphene sheets[72, 73, 74]. Indeed, such roughness constitutes short-range correlated disorder, which has also been shown theoretically to lead to scattering rates which scale linearly with ω in graphene [128].

Comparison can also be made with results obtained on epitaxial graphene grown on SiC. In such a system the Dirac point is $\sim$ 0.5 eV below the Fermi level which changes the quasiparticle dynamics resulting in a non-linear behavior for Γ_i vs ω. In particular, it has been shown that electron-plasmon interaction in doped epitaxial graphene results in an increase in the electron scattering rate in a narrow energy region where $\omega \sim E_D$.[8] (see black curve in Fig 4.7(b)). However, at deeper binding energies a nearly linear increase of Γ_i has been demonstrated with a slope of $\sim$ 0.025 Å$^{-1}eV^{-1}$, which is comparable to our measured value of β.

Because of the unique Dirac Fermion behavior and two-dimensionality of graphene, there has been much discussion of many-body physics that would lead to lifetime broadening in ARPES measurements of graphene[8, 129, 130, 131]. In conventional bulk crystals Fermi-liquid theory predicts the decay of a photohole through creation of an electron-hole pair to result in a lifetime which scales as $(E - E_F)^2$, in proportion to the number of excitation pathways that satisfy momentum and energy conservation. However, the linear dispersion of the graphene bands, along with the vanishing density of states at E_F, modify this picture. Hence, undoped graphene is expected to show anomalous marginal Fermi-liquid behavior, characterized by a lifetime that scales as $(E - E_F)^{-1}$.[129] Electron-phonon interaction

has also been shown experimentally to lead to linewidth broadening.[125, 8] However, the interaction is limited by the phonon dispersion to within 140 meV of E_F.[106] Coulombic interactions, however can affect scattering rates for electrons well below E_F. As noted above, elastic scattering due to short-range correlated impurities such as adatoms, dislocations or corrugations has also been shown theoretically to produce a $(E - E_F)^{-1}$ dependence on lifetime.[128]

As discussed above, prior STS measurements have confirmed this linear increase for a small range of energies (∼150 meV) in the vicinity of the Fermi level for exfoliated graphene on graphite.[127] Our measurement confirms that this behavior persists as far as 2eV below the Fermi level; a log-log plot of Γ_i vs ω displays a slope of ∼1. As noted above, such marginal Fermi-liquid behavior has also been observed by femtosecond time-resolved photoemission spectroscopy on graphite.[126]

We now return to the topic of asymmetry in MDC peak shape. As many recent theoretical studies have pointed out, the commonly-made **k**-independent approximation for $\mathrm{Im}[\Sigma(\mathbf{k},\omega)]$ is not fully valid in graphene as the doping level approaches zero.[129, 130] The vanishing density of states at $\omega = E_F$ along with graphene's linear dispersion near E_F places a kinematic restriction on the available phase space for electron-electron scattering. The scattering pathway $e^- \rightarrow e^- + e^- h^+$ is only available for off-shell electrons for which $\omega > v_F|\mathbf{k}|$ and is kinematically forbidden when $\omega < v_F|\mathbf{k}|$. Thus, one expects a discontinuity in $\mathrm{Im}[\Sigma(\mathbf{k},\omega)]$ at $\omega = k$ and decay due to electron-electron interaction may be indicated by asymmetry in MDC peak shape.[128, 130] As mentioned above and indicated in Fig. 4.6, in MDCs taken through the K point for monolayer graphene additional spectral weight is present in the $\omega > v_F|\mathbf{k}|$ regime. In principle, a full deconvolution of the ARPES intensity would recover the exact function form of $A(\mathbf{k},\omega)$. However, such a procedure would require use of the full 2D integral specified by Eq. 4.2, which is beyond the scope of the work presented here.

4.5 ARPES formalism for thin film membrane

In this section, we develop the detailed formalism used to evaluate the graphene ARPES results presented above.

According to the standard tight-binding scheme, initial π states in the valence band of graphene with energy ω_k and crystal-momentum $\mathbf{k}$ are represented as a linear combination of molecular p_z orbital states:

$$\psi_{\mathbf{k}}(\mathbf{r}) = \frac{1}{\sqrt{N}} \sum_{\mathbf{R}} e^{i\mathbf{k}\cdot\mathbf{R}} \sum_{j=A,B} C_j^{\mathbf{k}} \phi(\mathbf{r} - \mathbf{R} - \tau_j) \tag{4.7}$$

where $\frac{1}{\sqrt{N}}$ is an overall normalization factor, A and B designate the sublattice sites and τ_j their locations within the unit cell. The $C_j^{\mathbf{k}}$ are complex coefficients obtained from the tight-binding model and the ϕ are molecular p_z orbitals. The sum over $\mathbf{R}$ runs over all N unit cells in the crystal (note that we work in the limit where $N \to \infty$).

The transition-matrix for photoexcitation from this initial state to a plane wave final state with total momentum $\mathbf{k_f}$ outside the crystal can be written, using the dipole approximation, as follows:

$$M^{\mathbf{k}} \propto \int d^3r e^{-i\mathbf{k}_f\cdot\mathbf{r}} (\mathbf{p}\cdot\mathbf{A}) \psi_{\mathbf{k_i}}(\mathbf{r}) \tag{4.8}$$

Inserting the above definition for the initial state we obtain:

$$M^{\mathbf{k}} \propto (\mathbf{k_i}\cdot\hat{\lambda}) \sum_R e^{i(\mathbf{k_i}-\mathbf{k_f})\cdot\mathbf{R}} \tilde{\phi}(k_f) \sum_{j=A,B} C_j^{\mathbf{k}} e^{-i\mathbf{k_f}\cdot\tau_j} \tag{4.9}$$

where $\tilde{\phi}$ is the Fourier transform of the molecular p_z orbital and $\hat{\lambda}$ represents the polarization vector of the incoming radiation. We are interested in a small region of momentum-space in the vicinity of the K point. Since $\mathbf{k_i}\cdot\hat{\lambda}$ and $\tilde{\phi}(\mathbf{k_f})$ are nearly constant in this region, we concentrate our attention on the sum, $\sum e^{i(\mathbf{k_i}-\mathbf{k_f})\cdot\mathbf{R}} \sum C_j^{\mathbf{k_i}} e^{-i\mathbf{k_i}\cdot\tau_j}$. The sum over j, $\sum C_j^{\mathbf{k_i}} e^{-i\mathbf{k_f}\cdot\tau_j}$, depends only on the relative phase between the $C_j^{\mathbf{k}}$'s and the pathlength difference from atoms A and B to the detector. This term changes rapidly on a contour

around the K point. Along the ΓK direction, the term changes from 2 to 0 as we pass through the K point from the first to the second BZ. However, if we restrict ourselves to the region of **k**-space along the ΓK direction within the first BZ (see Fig 4.5), $\sum C_j^{\mathbf{k_i}} e^{-i\mathbf{k_f}\cdot\tau_j}$ is nearly constant. Thus, we are left with the sum $\sum e^{i(\mathbf{k_i}-\mathbf{k_f})\cdot\mathbf{R}}$.

For a 3D crystal with perfect translational symmetry the position vectors can be represented as: $\mathbf{R} = n_1\mathbf{a_1} + n_2\mathbf{a_2} + n_3\mathbf{a_3}$, where n_1, n_2, n_3 are integers and $\mathbf{a_1}, \mathbf{a_2}, \mathbf{a_3}$ are primitive lattice vectors. In this case, the sum over $\mathbf{R}$ reduces to a momentum-preserving delta function $\delta(\mathbf{k_f} - \mathbf{k_i} - \mathbf{G})$ where G is a reciprocal lattice vector. However, since graphene is a two-dimensional lattice, momentum conservation does not hold in the perpendicular direction. More significantly, exfoliated graphene is a flexible membrane that is not atomically flat, so the $\mathbf{R}$'s must be expressed in terms of a continuous variable; thus $\mathbf{R} = n_1\mathbf{a}_1 + n_2\mathbf{a}_2 + \Delta x + \Delta y + z$, where z_j is a continuous variable which represents the local height of the graphene sheet. The variation in height is such that we can consider the well-known theory of scattering from continuous rough surfaces in order to evaluate the sum in equation 4.9. We begin by replacing the discrete sum with an integral:

$$\sum_{\mathbf{R}} e^{i(\mathbf{k_i}-\mathbf{k_f})\cdot\mathbf{R}} = \int d^3r D(\mathbf{r}) e^{i(\mathbf{k_i}-\mathbf{k_f})\cdot\mathbf{r}} \tag{4.10}$$

where $D(r)$ is the density-function of the material which, for a perfectly crystalline flat sample, has the form:

$$D(\mathbf{r}) = \sum_{\mathbf{R}} \delta(\mathbf{r} - \mathbf{R}) \tag{4.11}$$

A periodic lattice generates a photoemission spectrum with the periodicity of the reciprocal lattice. However, since we are concerned with the photoemission spectrum in a small region of **k**-space in the first Brillouin zone, we may abandon the description of the surface as a discrete lattice and replace it with a smooth, continuous sheet. Thus, we approximate $D(r)$ as a surface density function:

$$D(\rho, z') \simeq \delta[z' - z(\rho)] \tag{4.12}$$

where $\rho = r_\parallel = (x, y)$ and $z' = r_\perp$. Thus, the surface is now defined by the height function $z = z(\rho)$. Inserting the above definition of $D(r)$ and explicitly separating $\mathbf{k_i}$ and $\mathbf{k_f}$ into components parallel and perpendicular to the surface we obtain:

$$M \propto \int d^2\rho e^{i(\mathbf{k_{i\perp}} - \mathbf{k_{f\perp}})\cdot z(\rho)} e^{i(\mathbf{k_{i\parallel}} - \mathbf{k_{f\parallel}})\cdot\rho} \tag{4.13}$$

We have retained momentum-conservation; for a constant $z(\rho)$ the above integral produces $\delta(\mathbf{k_{i\parallel}} - \mathbf{k_{f\parallel}})$ times a complex phase; but for a non-trivial $z(\rho)$, the delta function broadens since $e^{i(\mathbf{k_{i\perp}} - \mathbf{k_{f\perp}})\cdot z(\rho)}$ is no longer independent of ρ. Additionally, electronic states in graphene propagate on a curved space, which implies that the direction of the initial state wavevector, $\mathbf{k_i}$, varies as a function of position along the surface so that $k_{i\perp}$ and $k_{i\parallel}$ vary with ρ as well. This introduces additional phase variation into the exponential argument $(\mathbf{k_{i\perp}} - \mathbf{k_{f\perp}}) \cdot z(\rho)$. However, this variation is very small in comparison to that introduced by changes in $z(\rho)$ and can effectively be ignored with little change in our final result. In particular, $k_{i\perp}$ varies proportional to $k\frac{\partial z}{\partial \rho_k}$ which is on the order of 0.01 Å^{-1}. Thus the phase variation in the term $k_{i\perp} z \ll 1$ ($\Delta z \approx 2$ Å) is very small in comparison to the variation in the $k_{f\perp} z$ term ($k_{f\perp}$ ranges from 2.5 to 3.5 Å^{-1}). Thus, we will approximate the direction of the initial state wavevector, $\mathbf{k_i}$, as constant for all points on the surface. This means that $\mathbf{k}$ is not ρ dependent and we can define a new vector $\mathbf{k} = \mathbf{k_i} - \mathbf{k_f}$, so that our expression becomes:

$$M \propto \int d^2\rho e^{i\mathbf{k}_\perp \cdot z(\rho)} e^{i\mathbf{k}_\parallel \cdot \rho} \tag{4.14}$$

To find the photoemission intensity we use Fermi's golden rule which yields:

$$I = \frac{2\pi}{\hbar}\|M\|^2\delta(\epsilon + \hbar\omega - \hbar^2k^2/2m), \tag{4.15a}$$

$$\|M\|^2 \propto \int d^2\rho' d^2\rho e^{i\mathbf{k}_\perp\cdot z(\rho)} e^{i\mathbf{k}_\parallel\cdot\rho} e^{-i\mathbf{k}_\perp\cdot z(\rho')} e^{-i\mathbf{k}_\parallel\cdot\rho'}. \tag{4.15b}$$

Defining $r = \rho - \rho'$ we can rearrange to obtain:

$$I \propto \int d^2r \left(\int d^2\rho e^{i\mathbf{k}_\perp\cdot[z(\rho+r)-z(\rho)]} \right) e^{i\mathbf{k}_\parallel\cdot r} \tag{4.16}$$

The term inside the parentheses is the height-difference function, $C(r, k_\perp)$, of the surface which is related to the height-height correlation function, $H(r) = \langle|z(r_0 + r) - z(r_0)|^2\rangle$. It is straight forward to show that the $C(r, k_\perp)$ equals $e^{-\frac{1}{2}H(r)k_\perp^2}$.[94] Thus, we have:

$$I \propto \int d^2r C(k_\perp, r) e^{i\mathbf{k}_\parallel\cdot r}, \tag{4.17a}$$

$$C(k_\perp, r) = e^{-\frac{1}{2}H(r)k_\perp^2}. \tag{4.17b}$$

For a large class of surfaces, $H(r)$ has the following properties:

$$H(r) \propto e^{2\alpha}, \text{for } r \ll \xi \tag{4.18}$$

$$H(r) = 2w^2, \text{for } r \gg \xi \tag{4.19}$$

where α is a measure of the small scale roughness termed the "roughness exponent." In particular, it can be shown that the full width at half maximum (FWHM) of $I(k_\parallel)$ (with $k_\perp$ held constant) scales as $\xi^{-1}(wk_\perp)^{\frac{1}{\alpha}}$ when $(wk_\perp)^2 \gg 1$. The functional form of $I(k_\parallel)$ is well approximated as:[94]

$$S_{k_\perp}(\mathbf{k}_\parallel) = (\xi/(wk_\perp)^{\frac{1}{\alpha}})F_\alpha(\mathbf{k}_\parallel\xi/(wk_\perp)^{\frac{1}{\alpha}})$$
$$F_\alpha(Y) = \int XdXexp(-X^{2\alpha})J_0(XY) \tag{4.20}$$

The above discussion began with the assumption that the initial state, ψ_k, had a well defined pseudo-momentum, k, and energy ω_k. To include initial state broadening in our description, we replace ψ_k with a sum over multiple momentum states, $\sum a_k\psi_k$, where the a_k are complex coefficients. The coefficients, a_k, are related to the spectral function, $A(k,\omega)$ by $|a_k|^2 = A(k,\omega)$ with the spectral function defined as:

$$A(k,\omega) = \frac{Im(\Sigma)}{(\omega_k - \omega - Re(\Sigma))^2 + Im(\Sigma)^2} \tag{4.21}$$

where $\Sigma = \Sigma(k,\omega)$ is the quasiparticle self-energy. Retaining our simple description of the final state as a free-electron state with momentum q, our transition matrix becomes a sum, $M = \sum a_k M^{kq}$, over multiple matrix elements weighted by the complex coefficients a_k, where the M^{kq} are the original transition matrix elements defined in Eq. 4.9. Again, using Fermi's golden rule we find that the transition probability is proportional to the square of this sum:

$$I \propto |M|^2 = |\sum_k a_k M^{kq}|^2 =$$
$$\sum_k |a_k|^2|M^{kq}|^2 + \sum_{k\neq k'} a_k^* a_{k'} M^{kq*} M^{k'q} \tag{4.22}$$

The cross terms have the form:

$$M^{kq*}M^{k'q} \propto \int d^2r \left(\int d^2\rho e^{i\mathbf{k}_\perp\cdot[z(\rho+r)-z(\rho)]}e^{i\Delta\mathbf{k}_\parallel\rho}\right)e^{i\mathbf{k'}_\parallel\cdot r} \tag{4.23}$$

where $\Delta\mathbf{k}_\parallel = \mathbf{k'}_\parallel - \mathbf{k}_\parallel$, $\mathbf{k}_\perp \approx \mathbf{k'}_\perp$. The $e^{i\Delta\mathbf{k}_\parallel\rho}$ factor in the ρ integral introduces a ran-

dom phase that causes the integral to average to zero (since it is taken over the whole surface). Thus, the cross terms can be safely neglected and we arrive at the final expression or photoemission intensity as a function of $k_{\parallel}$ with $k_{\perp}$ fixed, described by Eq. 4.2.

4.6 Conclusion

Photoemission on thin sheets of 2D crystals is expected to grow in importance as interest in single-layer insulators and semiconductors increases. We have performed ARPES on a 2D suspended surface with well-defined surface corrugation. By comparing our work with our prior results obtained from diffraction measurements on corrugation in suspended graphene sheets[111] we have developed a model for understanding the effect of corrugation on ARPES spectra. By analyzing results obtained with different photon excitation energies, we have estimated the contribution of surface roughness to broadening. Thus, despite the surface corrugation in the graphene layer, it is still possible to develop insights into graphene physics. In particular, we have shown that exfoliated suspended graphene is essentially undoped in its pristine form. Additionally, we have shown that the band structure has no significant deviations from linearity in the vicinity of the Dirac point. Our measured Fermi velocity is comparable to results obtained on supported graphene by transport and optical measurements. Finally, we have also shown that undoped exfoliated graphene behaves as a marginal Fermi-liquid with an anomalous carrier lifetime, which scales as $(E - E_F)^{-1}$.

Chapter 5

Band Mapping of Self Assembled Nanostructures on Single Crystal Surfaces

In this chapter, I describe resonant band mapping of the the model surface systems Cu(111) and Cu(775) using a relatively high-repetition-rate femtosecond OPA source, which is tunable over the photon-energy range of 3.75 to 5 eV. The results show that resonant band mapping can be done with such an OPA source. In addition, the measurements show that, while strong pumping can be obtained with this source, any space charge is sufficiently reduced such that sharp features can be readily observed.

5.1 Introduction

While angle-resolved photoemission spectroscopy (ARPES) is a powerful and widely used technique for probing the occupied states of the band structure of single-crystal materials [30, 31, 32, 33, 6], inverse photoemission (IPE) spectroscopy [35, 36, 37] and two-photon photoemission (2PPE) [23, 38, 39, 20, 40, 41, 42, 43, 44, 45, 46, 47] are the accepted techniques for probing their unoccupied states. Recently, 2PPE has become more widely used due to its

high energy-resolution and the fact that it allows measurement of ultrafast dynamics using pump-probe methods [40, 41, 42, 44, 45, 46, 47]. In addition, the commonly employed high-repetition-rate, i.e., ∼100 MHz, Ti:Sapphire-based lasers have been effective in providing enhanced signal-noise ratios over lower-repetition-rate, nanosecond, dye or excimer lasers.

Band mapping is a major measurement technique for electronic structures that uses occupied-state ARPES in conjunction with a photon-energy-tuned synchrotron beamline[30, 31, 32, 33, 6]. Band mapping can be carried out in 2PPE by using a tunable laser source via resonant excitation of a target intermediate state from a well defined initial state, followed by further excitation to the final-state continuum prior to full equilibration of the $k_{\|}$states[132, 133]. Such crystal-momentum equilibration times have been measured by several authors and, in general, it is found that intraband and interband lifetimes are of the order of 60 and 40 fs, respectively[47, 134]. Thus during pumping within a typical 90-fs pulse, the electron distribution will be only partially equilibrated. This lack of full equilibration in the electron distribution of the excited states can lead to a resonance in the energy-distribution curves (EDC) as the laser photon energy is tuned through the energy spacing of the ground- and target-excited state. This approach has been demonstrated previously using a tunable frequency-doubled dye-laser system[132, 133]. However, a nanosecond-dye-laser system cannot achieve the same 2PPE signal-to-noise ratio in comparison with that using a much higher repetition-rate Ti:Sapphire system and cannot also achieve the same degree of unequilibrated electron distribution that is possible with a femtosecond pulse source.

Optical parametric amplifiers (OPA), driven by Ti:Sapphire lasers are tunable over a wide bandwidth range and thus it is possible to use this tunable laser for band mapping of low-binding-energy surface systems, i.e., those accessible with two 4-5 eV photons. While Ti:Sapphire-based, synchronously-pumped, optical parametric oscillators (OPO) in conjunction with frequency doubling are able to operate at the high ∼100 MHz repetition-rates of Ti:Sapphire oscillators, the use of Ti:Sapphire-based OPA systems in the ∼100 kHz repetition-rate is more conveniently and readily realized. In addition, OPAs are able to provide a higher tuning bandwidth compared to OPOs because of the larger energies achievable

in the OPAs.

5.2 Experiment

In the experiments described in this chapter, a high-purity (99.999 % purity) single-crystal copper sample of 1.2-cm diameter is cut to the desired (111) and (775) orientations on opposite sides of the crystal. The 8.5° miscut of the (775) surface with respect to (111) is accurate to within 0.1°. The laser system uses an ultrafast Ti:Sapphire pulse source, the pulses of which are amplified in a regenerative amplifier, and then used to drive an optical parametric amplifier to provide a tunable source of visible light. This output is then converted to UV wavelengths by second harmonic-generation in a 1 mm BBO crystal. Photoemitted electrons are collected using a 160° (36.5-mm radius) spherical-sector energy analyzer. The angular data is collected along the MΓM direction of the (111) surface Brillouin zone. For the (775) surface this corresponds to the direction across the steps. Throughout the experiments presented in this chapter, the sample was biased at -4 V to reduce the effects of stray fields. The data presented is corrected for both the additional kinetic energy and change in the parallel momentum $k_{\|}$of the electrons due to this accelerating voltage[52]. Additional details of sample preparation and the experimental setup were presented in Chapter 2.

The normally-unoccupied image states are populated by resonant excitation from the occupied sp-like surface state of Cu(111) and/or by nonresonant indirect excitation via electron transfer to and then from occupied bulk states, and then probed after absorption of a second photon of the same energy; see schematic diagram in Fig. 5.1. Since the Cu surface state and image states have different effective masses, resonant excitation occurs at different parallel momenta for each choice of photon energy. By tuning the photon energy, it is possible to resonantly map the entire surface and image-state spectra. The femtosecond laser provides a high signal-to-noise ratio and the resonant mapping scheme allows for precise measurement of the dispersion and reference planes (the dispersion minimum) of both the occupied and the excited bands.

5.3 Excitation Spectra and Processes

Prior to describing the bandmapping measurements, I will show the effect of excitation resonance on the EDC curves as well as the linewidth of these curves and their consistency with previous measurements of resonant 2PPE photoemission. The relevant electronic states for the experiment are shown in the sketch in Fig. 5.1 along with a depiction of two possible excitation channels as well as two measured representative photoemission energy-distribution curves (EDCs), each taken at a different angle for illumination of a Cu(111) surface with $\hbar\omega$ = 4.29 eV. The lower intensity curve (circles), taken at $k_{\|}$= 0 Å^{-1}shows two peaks, while the second (squares), taken at $k_{\|}$= 0 Å^{-1}, shows a single, much-higher intensity peak. Considering first the circle curve, the well-established binding energies and dispersion relations of the Cu(111) surface can be used to assign the lower energy of the two peaks to a nonresonant two-photon process from the n = 0 occupied surface state and the higher energy peak to photoemission from an n = 1 image state, which is excited by scattering from a nearby bulk excited state or intraband scattering. Because of the nature of the excitation processes, each of the processes is termed nonresonant excitation. Note that, in this case, the surface and image-state-peak energies are readily resolvable. On the other hand, at $k_{\|}$= -0.18 Å^{-1}a single, much-higher-intensity peak is observed. Again using the well established energetics of this system, it can be shown that, for this photon energy and parallel momentum, excitation of the n = 1 image state from the n = 0 surface state is resonant with the photon energy in this case. This resonance leads to a sharp, well defined photoemission signal.

Photoemission of a surface-state electron requires the simultaneous absorption of two photons through a virtual or resonant intermediate state, while photoemission of an indirectly excited image-state electron is accomplished through absorption of a single photon. The kinetic energy of electrons photoemitted from the surface and image states can be written, respectively, as $E_0 = 2\hbar\omega - \varepsilon_0 - \phi$ and $E_1 = \hbar\omega - \varepsilon_1$ where $\hbar\omega$ is the incident photon energy, ϕ is the work function and ε_0 and ε_1 are the binding energies of the surface state and

image state electrons, respectively; these binding energies are referenced to the Fermi and vacuum levels, respectively. Thus, the kinetic energy of photoemitted surface-state electrons varies as $2\hbar\omega$, twice the incident photon energy, while the kinetic energy of photoemitted image-state electrons varies as $\hbar\omega$ a result which can be used to distinguish occupied (surface) states from unoccupied (image) states. In addition, the relative separation in energy space of image, E_1, and surface state, E_0, peaks, i.e.,$E_1 - E_0$, are dependent on the incident-photon energy; thus the resonance condition, $E_1 - E_0 = 0$, or equivalently, $\hbar\omega = \varepsilon_0 + \phi - \varepsilon_1$, may hold at different parallel momenta for one excitation wavelength.

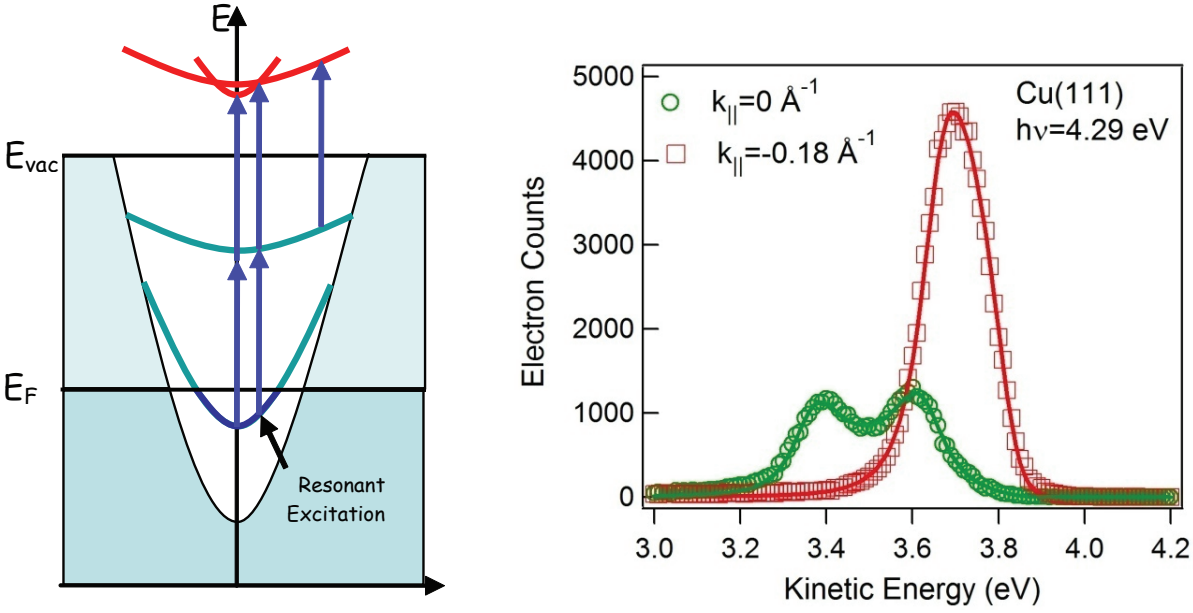

Figure 5.1: (Left) Schematic photoemission channels observed in the 2PPE process using the n = 0 surface and n = 1 image states of Cu(111). The red lines above the vacuum level reflect the measured 2PPE final state kinetic energies. (Right) EDCs from Cu(111) measured at $k_{\|}$= 0 Å^{-1}and $k_{\|}$= -0.18 Å^{-1}using 4.29 eV photons. The data is fit using the functional form discussed in the text [Eq. (1)]. The two curves represent EDCs under off-resonant and near-resonant conditions.

In order to determine the lineshape of the photoemitted signal, I will express the 2PPE intensity or the EDC at a particular emission angle as:

$$I(E) = \frac{a}{[(E-E_0)^2 + (\Gamma_0/2)^2][(E-E_1)^2 + (\Gamma_1/2)^2]} + \frac{b}{(E-E_1)^2 + (\Gamma_1/2)^2} \qquad (5.1)$$

where E_0 and E_1 are the kinetic energies described above, Γ_0 and Γ_1 are the linewidths corresponding to surface- and image-state peaks, and a and b are fitting parameters. This expression is consistent with prior theoretical treatments of two-photon photoemission [135, 136]. The first term in the above equation represents photoemission from coherently coupled surface and image states, whereas the second term corresponds to electrons that are first excited into an unoccupied state, and then scattered by electron-electron interactions or other scattering centers into an image state. As can be seen from the form of the first term, resonant enhancement occurs when $E_0 = E_1$. Although Eq. 5.1 is written for narrow-linewidth laser sources[135, 136], it can be used as a first approximation to describe sources with the 20 meV transform-limited linewidth of the femtosecond source used in this study. As an example, fitted curves corresponding to the functional form in Eq. (1) for 4.29 eV incident photon energy data are shown in Fig. 5.1. In this case, the coherent term dominates the photoemission signal at the resonance and accounts for as much as 75% of the image-state electrons at the band minimum ($k_{\|}$= 0 Å^{-1}). Taking into account spectrometer resolution, the measured linewidths are 76 ± 25 meV and 82 ± 25 meV for the n = 0 and n = 1 states, respectively, at $k_{\|}$= 0 Å^{-1}. These results agree with the room temperature measurements of Wallauer and Fauster of 65 ± 15 meV and 85 ± 10 meV, respectively[137], and measurements of Knoesel, et al. of 62 ± 4 meV and 62 ± 5 meV, respectively[138]. Note, that in our case, this resonant peak is slightly asymmetric due to the Fermi cut-off at ∼3.85 eV. For the n = 1 state, the expected lifetime broadening is ∼ 40 meV, where the rest of the contribution of about 22 meV to the intrinsic linewidth arises from pure dephasing[138, 139].

By operating the OPA source at pulse energies below those leading to space-charge distortion, useful data were collected over a relatively wide photon energy tuning range of ∼ 3.9 to 5 eV. The dispersion curves of the surface states in question were obtained by

measuring the EDC curves over a set of typical emission angles from $-18°$ to $+18°$. Figure 5.2 shows the data obtained at one photon energy, 4.29 eV for Cu(111) and 4.48 eV for Cu(775). In Fig. 5.2(a), the lower of the two bands is that due to the n = 0 surface state (see also Fig. 5.1). As discussed earlier, due to its lower effective mass ($m^* \approx 0.4m_e$) compared to the image-state effective mass ($m^* \approx m_e$), the surface-state band disperses faster and crosses the image-state band at ~ 0.17 Å^{-1}away from the band minimum. In the case of Fig. 5.2(b), the surface-state band of Cu(775) is folded and the band minimum appears at an off-normal angle corresponding to $k_{\|}$=π/L (for Cu(775), $\pi/L = 0.22$ Å^{-1}), due to vicinal cut and superlattice formation as expected from earlier studies of this surface [140, 141] as well as for other noble-metal vicinal surfaces. [52, 52] Note that for the $k_{\|}$= π/L branch of the surface state in Fig. 5.2(b) a strong resonance is observed around the crossing point of this surface state branch and the n = 1 feature. We can also observe the weak surface-state feature for $k_{\|}$< 0.18 Å^{-1}. In contrast, the surface-state feature in the $k_{\|}$= $-\pi/L$ branch is invisible. The resonance feature associated with this branch and the n = 1 state, however, can be observed because of its slightly higher intensity relative to the nearby signal. Thus there is an asymmetry in the two observed Umklapp branches of the surface state, which will be discussed below. In the lower portion of Figs. 5.2(a) and (b), the maximum EDC intensity is plotted as a function of parallel momentum for this same data. Note that the photoemission signal intensity clearly peaks at a value of $k_{\|}$corresponding to the crossing of the surface and image states as a result of resonant excitation. The resonances on the Cu(111) surface are sharper in $k_{\|}$and stronger compared to those on the Cu(775) surface. This relative sharpness is related to the linewidths of the surface and image states, which are considerably broader on the stepped surface due to the scattering and structural variation in terrace widths, as well due to hybridization of the surface states with bulk states [142, 143]. In addition, any step-edge defect scattering would increase the nonresonant contribution given by the second term in Eq. 5.1. Simulated photoemission intensities using Eq. 5.1 and the known energetic properties of the bands are shown as insets in Fig. 5.2. This simulation was obtained using the two terms of Eq. 5.1 at a given value of $k_{\|}$and the fitted dispersion

curves for the surface and n = 1 image states. For the case of Fig. 5.2(b), an additional term, with the same functional form as the first term of Eq. 5.1, was added to model the two separate branches of the band-folded surface state. In both cases, the final simulated intensities include the Fermi function for room temperature. The simulations show good qualitative agreement with the observed photoemission intensities. Finally note that the dispersion data for both the image and the surface state can be obtained from plots such as that presented in Fig. 5.2. However, as discussed in earlier work, the interaction of the surface and image states can distort the apparent band dispersion and result in erroneous determination of dispersive properties [38]. This can be even more important in the case of stepped surfaces where the band structure is more complicated as shown in Fig. 5.2(b). To illustrate this complication, in Fig. 5.2(b), the Umklapp surface state-band centered at $k_{\|}$= $-\pi/L$= - 0.22 $\text{Å}^{-1}$is not sufficiently strong to be observed in the raw EDC data, while its resonance response, as it crosses the image-state band, can be easily identified, as discussed above. In some photoemission experiments Umklapp features from noble-metal stepped surfaces exhibit a lack of symmetry in intensity on either side of $k_{\|}$= 0 and, specifically no Umklapp feature is seen for negative values of $k_{\|}$. For example, it is well known that the step-modulated state on vicinal Cu exhibits a photon-energy dependent intensity variation. As shown on Cu(223) [144], Cu(443) [145], and Cu(775) [146], the step-modulated surface state is most intense in PE measurements for photon energy $\leq$ 45 eV, while its Umklapp, with band minimum located at $k_{\|}$=$3\pi/L$ becomes dominant as the photon energies increase to >45 eV. This phenomenon has been explained as a result of photoemission resonances [143, 144], which are determined by matching the $k_{\perp}$component of the final state with the spatial oscillation of the surface state as it evanesces into the substrate. Note that in our 2PPE measurement, however, an Umklapp is obtained at $k_{\|}$= $-\pi/L$. This result is opposite to that anticipated from single-photoemission experiments and theory, but is in agreement with other 2PPE experiments, such as that of Baumberger et al. on Cu(443)[142].

An important feature of the photoemission seen in our system is the degree to which the process relies on non-equilibration of the electron distribution in the excited intermediate

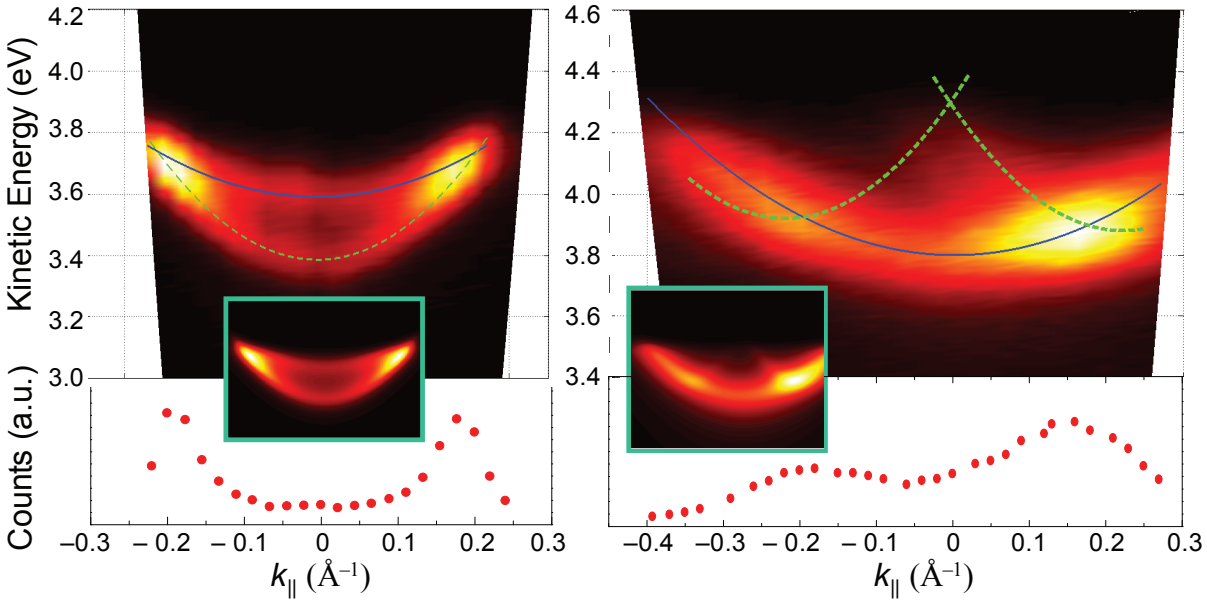

Figure 5.2: Angle-resolved 2PPE (a) from Cu(111) surface at an incident photon energy of 4.29 eV and (b) from Cu(775) at an incident photon energy of 4.48 eV. The green dotted lines represent the n = 0 surface-state band dispersion and the solid blue lines represent the n = 1 image-state band dispersion. The maximum photoemission signal intensity as a function of momentum is plotted in the lower portion of each figure. Using the measured effective masses and linewidths, simulations of the 2PPE signals for (111) and (775) surfaces using Eq. (1) are presented in the insets (an extra term similar to the first term in Eq. (1) is added for the (775) surface simulation).

state, from which photoemission occurs. This lack of full equilibration is not seen, for example, in typical, single-photon photoemission band-mapping experiments done using synchrotron or UV lamp sources. In those cases, non-equilibration does not play a role in determining the excitation-relaxation processes in the final state since it couples directly into the free-electron states and since the occupation of the initial state is given accurately by ambient temperature Fermi-Dirac statistics. In the case of 2PPE, the excitation time is 100 fs and photoemission occurs at times comparable to or faster than the intraband relaxation time of the intermediate state. As mentioned above for Cu(111) the n = 1 lifetime has been measured to be $\sim$ 18 fs [138, 139], a result in agreement with many-body theory [47, 147, 148, 149]. This lifetime arises from contributions due to intraband and interband processes [149]. This lack of full equilibration within the excited state can be seen by the

comparatively narrow region in k-space, over which photoemission occurs in Fig. 5.2. Note that in our experiments with the stepped surface, the intermediate distribution is broadened out more perceptibly than for the flat surface; however, the bright resonant portion of the curves in Fig. 5.2 indicates that this broadening or equilibration is not complete and that resonant mapping is still possible. This additional broadening is attributed to hybridization between the bulk and surfaces states [142, 143], and step scattering[42, 150].

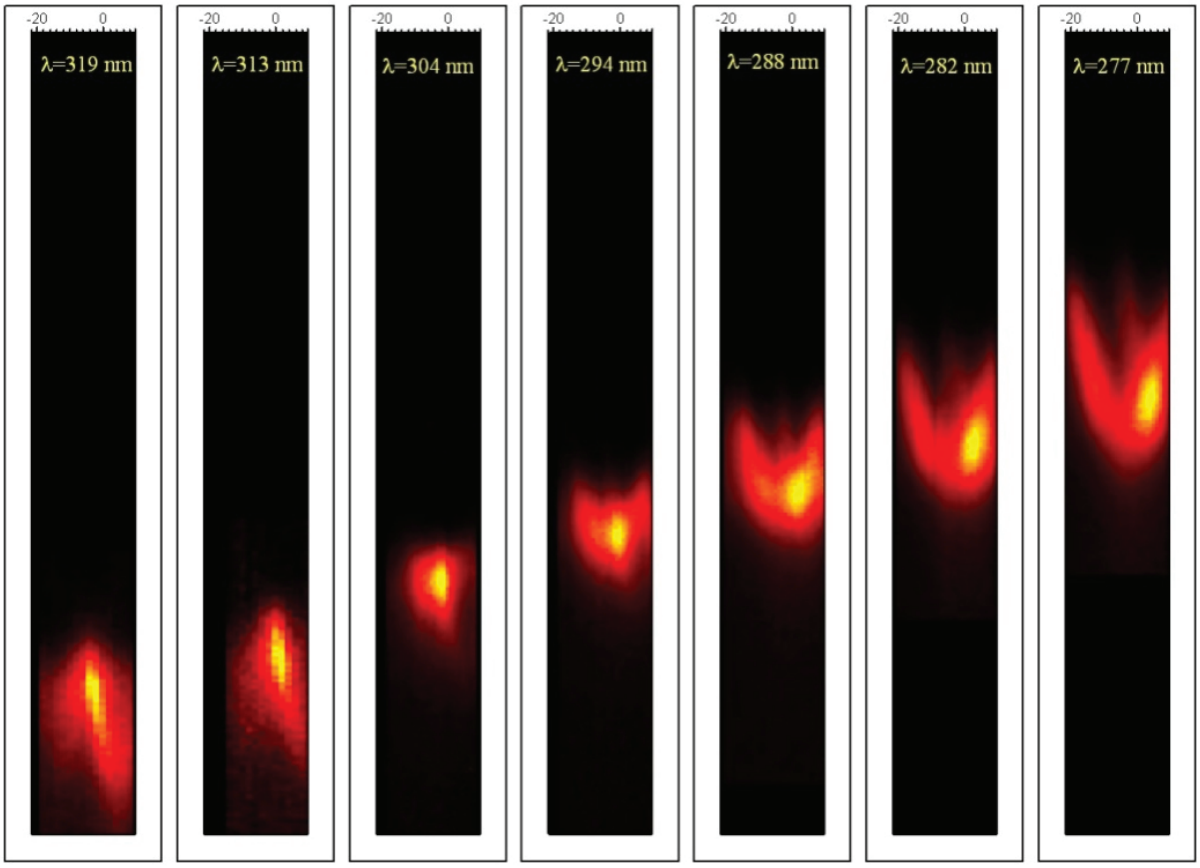

Figure 5.3: Angle-resolved 2PPE spectra for a series of incident photon energies on the Cu(775) surface. From left to right, the photon energies are 3.89, 3.96, 4.08, 4.22, 4.31, 4.40, and 4.48 eV, respectively.

To carry out band mapping, the binding energy and the crystal momentum were measured as described in the experimental section. Figure 5.3 shows a series of angle-resolved 2PPE spectra from the Cu(775) surface at different incident-photon energies. As mentioned above, the origin of the resonance point is reflected by the first term in Eq. 5.1 and is due

to the fact that the image state is directly pumped from the surface state and that, due to the intense, ultrafast laser pulse, photoemission takes place prior to electron equilibration. The measured resonant points obtained from both surfaces are shown in Fig. 5.4 along with parabolic fits to the image and surface states. In the case of Cu(775) the surface state is folded due to the step superlattice [140, 141] and only parts of each folded band are visible. This band-folded surface state may be described by the Kronig–Penney model, wherein the steps are viewed as one-dimensional potential barriers, to yield the surface state energy given by

$$E(k_{\parallel}) = \frac{\hbar^2}{2m^* L^2}\left\{ \cos^{-1}[|T|\cos(k_{\parallel}L)] - \phi \right\}^2 - \varepsilon_0 \tag{5.2}$$

where $T = |T|e^{i\phi}$ is the complex transmission coefficient through the one-dimensional step barriers [151, 152]. Thus by setting L = 14.02 Å, one can obtain the values of the fitting parameters $\varepsilon_0, m^*, |T|$ and ϕ. The minima of the resulting bandfolded parabolas are separated by 0.44 Å^{-1}(i.e., the superlattice reciprocal vector). The measured binding energies for the Cu(111) and Cu(775) surface states are ε_0 = 0.40 ± 0.07 eV and 0.29 ± 0.06 eV respectively, in agreement with the values of 0.39 eV and 0.28 eV below E_F from earlier measurements [142, 141]. The reduced binding energy of the surface state on the stepped surface is attributed to confinement of electrons due to the step-edge potential [142, 153, 141, 145, 152]. The effective masses of the surface state are m^* = 0.40 ± 0.10 me and 0.48 ± 0.30 m_e for Cu(111) and Cu(775), respectively, corresponding to the blue solid-line fits to the data in the bottom panels of Figs. 5.4(a) and (b). The larger mass for the (775) surface compared with the flat surface, agrees with a previous measurement from a vicinal Cu(111) surface with a comparable terrace width of 15.4 Å, which yielded m^* = 0.45 m_e [152]. The remaining fitting parameters for the surface state of Cu(775) are $|T|$ = 0.99 ± 0.10 and $\phi = (0.96 \pm 0.26)\pi$. Note that the larger error bars associated with the (775) surface state bandfolding arise from the insufficient data for $|k_{\parallel}| > \pi/L$ and the assumption that the binding energies, ε_0, at $k_{\parallel} = \pi/L$ and π/L are equal. The measured

binding energy at $k_{\|} = -\pi/L$, however, appears to be lower than the binding energy at $k_{\|} = \pi/L$. This apparent difference in the measured binding energies at $k_{\|} = \pm\pi/L$ may be an artifact due to the large difference between the signal intensity levels at these two parabolas for this photon energy such as observed previously for ARPES experiments with Au(223) [154]. For the case of the n = 1 image-state, the band minimum is approximately 4.05 eV above the Fermi level with effective masses of $m^* = 1.17 \pm 0.10\ m_e$ and $m^* = 1.13 \pm 0.20\ m_e$ for Cu(111) and Cu(775), respectively, as shown in the top panels of Figs. 5.4(a) and (b).

In the case of the (775) surface, the band minimum of the image state is not at $k_{\|} = 0$ but slightly off normal. In a previous, more detailed, nanosecond-pulse band mapping experiment of the Cu(775) surface, the band minimum was observed for the emission in the [111] direction with a subtle inflection of band dispersion close to the surface normal. In the present experiment using fs pulses and with fewer data points, the band minimum in the data fit appeared at an intermediate point between the [111] and [775] directions.

The slightly higher measured value of the effective mass for both Cu(111) and Cu(775) surfaces for the n = 1 state may be indicative of the dynamic nonequilibrium processes occurring during resonant excitation of the electrons from the initial state to the intermediate n = 1 state. Despite the fact that our measured values agree with reported values within the uncertainty limits, these slightly higher values deserve additional comment. With regards to the Cu(111) surface, it has been found theoretically that for Cu(111) (and Ag(111)) the intrinsic linewidth of n = 1 increases linearly with ${k_{\|}}^2$ due chiefly to the contributions of intraband scattering and, more importantly, the increasing overlap between the image states and the bulk states, thus the lifetime decreases with increasing $k_{\|}$values [149]. For the case of Cu(001) and Ag(001), a similar dependence is observed experimentally[134, 155], but with a much weaker lifetime dependence on $k_{\|}$due to the small overlap between wavefunctions of the image state and the bulk states. Thus for ultrashort pulses with large bandwidth, a corresponding band $k_{\|}$values will be excited to the intermediate n = 1 band. Due to shorter lifetimes at the higher $k_{\|}$values, the resonance value will be weighted to lower energy

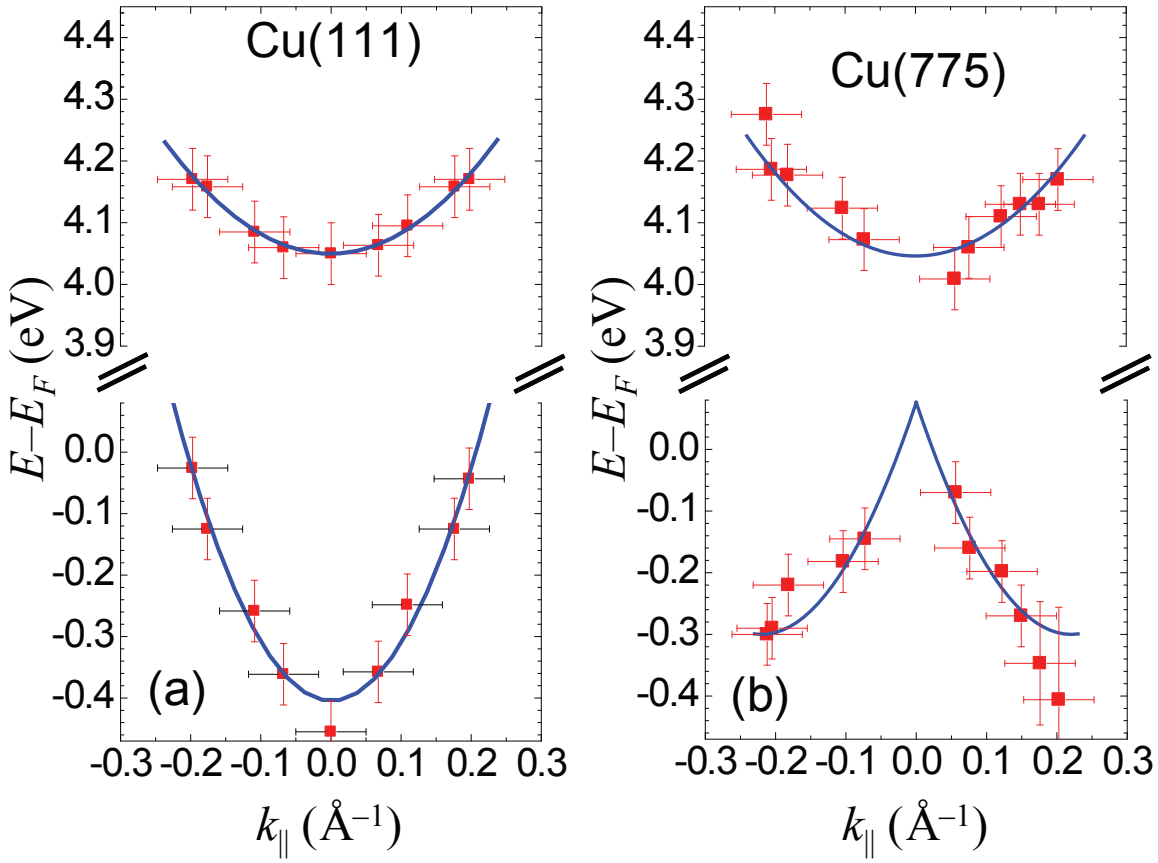

Figure 5.4: Band dispersion obtained for (a) Cu(111) and (b) Cu(775) using the technique of resonant band mapping. The top curves denote the n = 1 intermediate state, while the bottom curves denote the surface state (n = 0). The blue quadratic curves [(a) and top of (b)] are fits to the data. The fits yield n = 1 effective masses of $m^* = 1.17 \pm 0.10\ m_e$ and $m^* = 1.13 \pm 0.20\ m_e$ for the Cu(111) and Cu(775) surfaces, respectively. For Cu(111), $m^* = 0.40 \pm 0.10\ m_e$ for n = 0, while for Cu(775), $m^* = 0.48 \pm 0.30\ m_e$.

value. As direct consequence, the dispersion will yield a larger apparent effective mass. For the Cu(775), a different behavior is expected. Roth et al., demonstrated that in a stepped Cu(119) surface, the lifetime of the n = 1 state has an anisotropic behavior with respect to electrons traveling up-steps or down-steps [150]. As a consequence, this observation suggests that in resonant band-mapping, anisotropic behavior with respect to $k_{\|}$is also expected. To some degree this behavior is observed in Fig. 5.4(b) above. In our fitting however, we used the Kronig-Penney model, in which the bandfolded parabolas are symmetric. The measured effective mass is, again, within the uncertainty in agreement with reported values.

5.4 Conclusion

Laser photoemission is attracting new interest due to its low-photon energy and hence its ability to sample crystal regions away from the surface, that is to reliably probe the bulk-crystal electronic structure. The results shown in this chapter indicate that ultrafast lasers can be used, as well, for other photoemission techniques to study surface and near-surface excited states and bands. Ideally, an optimal laser source for 2PPE would provide high-intensity, tunable, and high-repetition-rate ($>$ 1 MHz) pulses, which permits the reduction of the laser intensity to the ideal one photoemitted-electron per laser pulse. In this chapter, I have examined the implications of newly emerging tunable moderate-repetition-rate lasers for resonant photoemission to map the excited electronic structure in surface bands. I investigated this possibility using the two model surface systems of flat Cu(111) and stepped Cu(775); in the case of the latter, its nanometer-scale arrays of potential steps yields information on lateral surface-electron movement. This nanostructured system is probed by accessing the unoccupied-state manifold with two-photon photoemission since the tunable, fs optical parametric amplifier (OPA) source (with 250 KHz repetition rate), allows resonant mapping with photon energies 4.2-4.6 eV of the unoccupied-states structure. I have demonstrated measurements of surface-state bandfolding due to Umklapp processes by the periodic steps on the Cu(775) surface. The weak unoccupied state observed here using this ultrafast tunable OPA has recently been identified as due to pumping of a bulk band. The observation of this state shows clearly the sufficiently high excitation rate possible with this OPA source.

Chapter 6

Mapping Unoccupied Bulk States using Two-photon Photoemission

6.1 Introduction

As discussed above, angle-resolved photoemission spectroscopy (PES) is the definitive method for accurate measurement of the electronic structure of crystalline solids [6]. Its use is normally constrained to occupied states ranging in energy across the valence band to thermally accessible regions just above the Fermi level E_F [156, 157]. For access of unoccupied bands between E_F and the vacuum level E_v, techniques such as inverse photoemission (IPE) [158, 37] and 2PPE[41, 39] have been developed. Compared to IPE, 2PPE has the advantage of superior energy resolution and time-resolved measurement capability. In this dissertation, I have discussed the importance of 2PPE in investigating the 2D electronic structure of planar and nanostructured metallic surfaces, including surface states (SS) and image states (IS)[41, 39]. Recent work, however, has shown the importance of bulk bands in interpreting 2PPE spectra [23, 159, 160, 161, 52, 49, 50, 51]. In particular, direct two-photon (2P) transitions between bulk bands below E_F and above E_v via *virtual* intermediate states have been observed using 2PPE on Ag(111) [23, 159, 160, 161] and Cu(111) [52].

There is an increasing need for mapping the unoccupied *bulk* electronic structure in the

region $E_F < E < E_v$, as underscored in a recent theoretical formalism for probing bound unoccupied bulk states by 2PPE [162]. This need is growing in many areas of condensed matter research; for example, in strongly correlated materials, non-Fermi-liquid behavior results in the emergence of bandgaps in this energy region, which are not well understood [163, 164]. In this Chapter, I show the use of 2PPE to map an excited, normally unoccupied Cu(111) bulk band in the energy range $E_F < E < E_v$. Thus, I will show that 2PPE is more powerful in its ability to observe bound, unoccupied states than previously demonstrated and should stimulate further studies of their properties.

2PPE has been used to study metals for over 45 years [165] and has been extensively used to probe 2D states below E_v [41, 39]. Its potential, however, for band mapping of bulk states has not been realized until now because of the relatively short lifetimes of bulk states due to electron-electron scattering, which leads to a rapid dephasing of the intermediate state and, thus, a much weaker 2PPE signal. In contrast, 2PPE from image states is readily observed because of the relatively long lifetimes of image states, e.g., $\sim$ 18 fs for IS1 (n=1 IS) [139], since the decay of image states is restricted by the lack of available final states and phase space. The *bulk* electron density N_b may be obtained using the lifetime τ. From Fermi-liquid theory, $\tau = \tau_0 E_F^2/(E - E_F)^2$, $\tau_0 = 128/(\pi^2\sqrt{3}\omega_p)$, and ω_p is the plasma frequency [166, 167, 57]. Using, e.g., $E - E_F \approx 4.4$ eV and Cu parameters [168, 169] yields $\tau \approx 1.6$ fs. If e-e scattering is the dominant loss channel, N_b may be estimated using a rate equation with pumping and loss terms that depend on laser intensity and τ, respectively. To determine the IS1 surface electron density n_s, a similar rate equation is used as discussed in detail in Ref. [170]. Note that only those bulk electrons within the electron mean free path, λ_e, of the surface have a non-negligible probability of being photoemitted. Thus, the relevant quantity for comparison with n_s is $n_b \approx N_b \lambda_e$. Under quasi-equilibrium condition and for sufficiently intense pulses, n_b/n_s scales as $\sim \tau(F/T_p)^{1/2}$, where F and T_p are the laser fluence and pulsewidth, respectively. Thus, despite the short bulk state τ, intense short pulses may be used for efficient pumping of the intermediate bulk states, thereby permitting observation of these states by 2PPE.

6.2 Experiment

Experiments were carried out at pressures $< 2 \times 10^{-10}$ Torr and room temperature. A Cu(111) sample was prepared by several cycles of Ar^+ sputtering and annealing until sharp LEED spots were observed. The surface was also characterized by 2PPE work function Φ measurement to find $\Phi = 4.9 \pm 0.05$ eV. The amplified Ti:Sapphire laser described in Chapter 2 was used as the photon source; laser pulses were p-polarized with 70° incidence angle. Starting from a relatively high value, the laser power was decreased until the 2PPE signal scaled quadratically with the power, and the detected energetic positions and linewidths of the SS or IS did not vary with power. Such a procedure minimized the space-charge effects and limited the maximum fluence to $F \approx 5\ \mu\text{J/cm}^2$. PE electrons were detected along the direction of the (111) surface Brillouin zone using a spherical-sector energy analyzer with 50 meV energy resolution. The sample was biased at -4 V to reduce the effects of stray fields. Corrections for the change in electron kinetic energy KE and parallel momentum $\hbar k_{||}$ due to this bias voltage were performed using a procedure described in Ref. [52].

6.3 Results and Discussion

2PPE data were taken for several $\hbar\omega$ in the range 4.4-4.9 eV, although our discussion below focuses mostly on results at three representative values of $\hbar\omega$: 4.84, 4.70, and 4.59 eV (Fig. 6.1). The 2PPE spectra displayed a set of distinctive features, e.g., Fig. 6.1(a) reveals four bands, where the top two and bottom two bands, each, overlap and exhibit sharp maxima at $k_{||} = \pm 0.22$ and $\pm 0.1 \text{Å}^{-1}$, respectively. Many of these features can be readily identified as originating from well-known 2D Cu(111) states based on their parabolic dispersion and binding energies; the $n = 0$, 1, and 2 features denote SS, IS1, and IS2, respectively. Fig. 1(d)-(f) shows the theoretical curves. The effective masses of the IS1 and SS, averaged over three photon energies, are $m^* = 1.04 \pm 0.10 m_e$ and $0.50 \pm 0.04 m_e$, respectively, where m_e is the electron mass, in excellent agreement with published results [3]. In addition, we have identified a fourth spectral feature, denoted "sp" in Fig 6.1, as due to bulk electronic

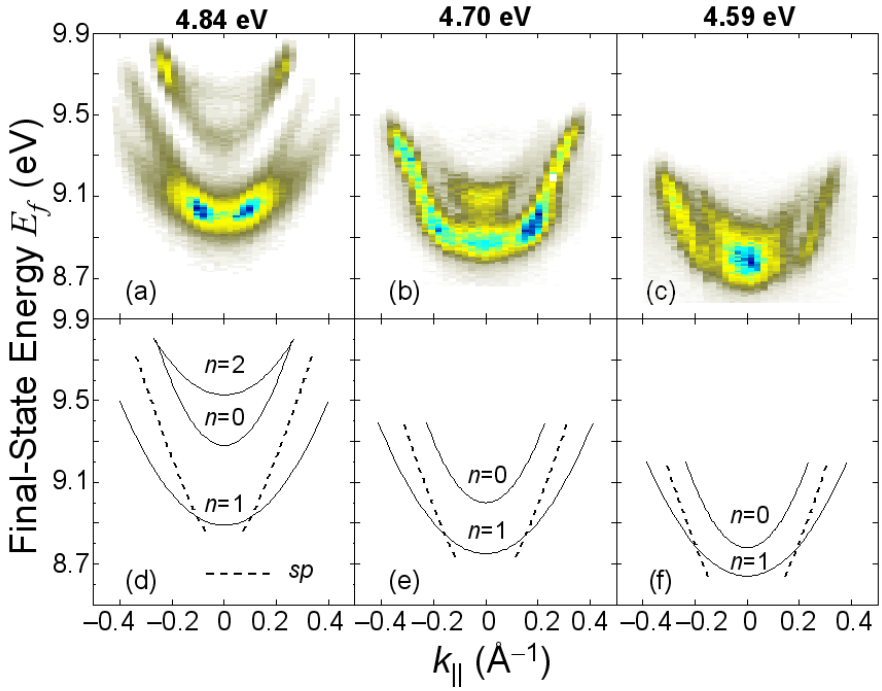

Figure 6.1: 2PPE spectra of Cu(111) at $\hbar\omega$ = (a) 4.84, (b) 4.7, and (c) 4.59 eV. Corresponding panels (d)-(f): theoretical calculations. Labels n =0, 1, and 2 denote SS, IS1, and IS2, respectively; "*sp*" (dashed line) indicates transitions between the occupied and unoccupied *sp* bands below E_v.

transitions between the lower and upper *sp*-bands just below and above E_F, respectively, as discussed below.

In 2PPE, the variation of E_f with $\hbar\omega$ may be used to identify the excitation channels for the intermediate state [41, 39]. Typical excitation channels are presented in Fig. 6.2(a): Photoexcitation of a specific intermediate 2D state may occur as a result of an indirect process, e.g., an intraband or bulk-to-surface band scattering process (A), direct 2P process through a virtual intermediate state (B), or direct surface-band-to-image-band excitation (C). Finally, excitation of a bulk band can occur via a direct bulk-to-bulk band transition (D). Thus for indirect excitation via an intermediate state, and direct excitation via a virtual intermediate state, E_f varies as $\hbar\omega$ and $2\hbar\omega$, respectively. Fig. 6.2(b) shows E_f data for SS, IS1, and IS2 bands at $k_{||} = 0$. Linear fits to the data yield $dE_f/d(\hbar\omega) = 2.04 \pm 0.14$, 1.03 ± 0.03, and 1.02 ± 0.05, respectively, in agreement with the expected $\hbar\omega$-dependence,

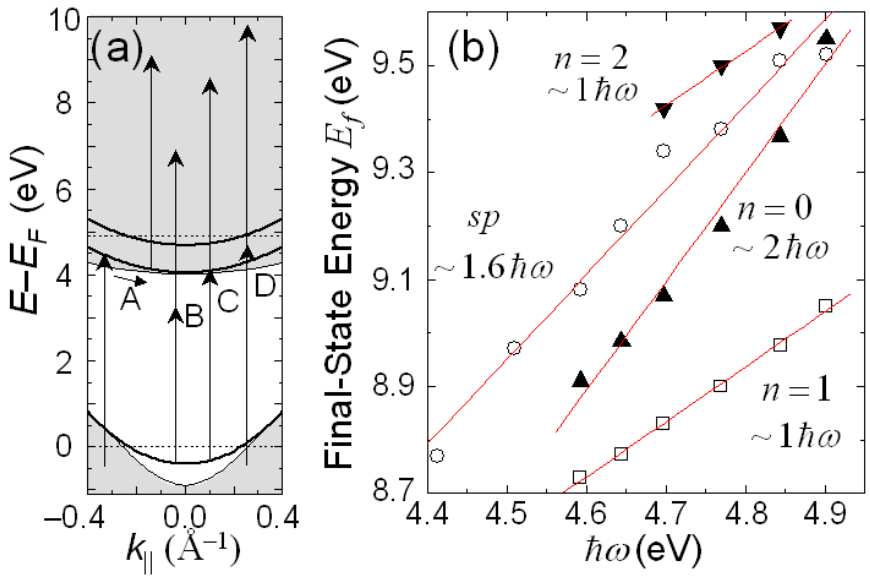

Figure 6.2: (a) Schemes for possible channels of intermediate-state excitation: (A) indirect excitation, (B) virtual-state transition, and resonant transition (C) between 2D states and (D) between bulk states. (b) E_f vs. $\hbar\omega$ for SS, IS1, IS2 bands at $k_{||} = 0.0$ Å^{-1}, and for *sp*-band feature at $k_{||} = 0.3$ Å^{-1}. Lines: fits to data with approximate slopes.

further confirming the identity of these states. For the *sp*-band features, $dE_f/d(\hbar\omega) = 1.64 \pm 0.09$ averaged over $k_{||}$= 0.1, 0.2, and 0.3 Å^{-1}. The data for $k_{||}$= 0.3 Å^{-1} are shown. The origin of this last $\hbar\omega$-dependence is discussed below.

Examination of prior 2PPE measurements on Cu(111) shows that the *sp*-feature in Fig. 6.1 has not been previously reported, which is likely due to the use of lower laser intensities, which decreases the effective population of the excited electrons, and in addition, the use of smaller photon energies, which prevents access to the relevant states. To confirm the bulk origin of this band, we first examine its dispersion with respect to $k_{||}$. Note that this feature has an approximately linear dispersion with respect to $k_{||}$, in contrast to the clearly parabolic SS, IS1, and IS2 bands. In addition, at lower photon energies, e.g., at $\hbar\omega = 4.59$ eV [Fig. 6.1(c)] and 4.51 eV (not shown), these "linear" features become more spectrally isolated and shorter in $k_{||}$ space. At larger $\hbar\omega$ (e.g., at 4.7 and 4.84 eV), these *sp*-features intersect the IS1 state. Note, further, that the *sp*-structures exhibit clear high-electron-energy cutoffs, which depend on $\hbar\omega$. In Fig. 1(b)-(c) the cutoff occurs at E_F; however, this is t not for the

case in Fig. 6.1(a).

To understand the physics of our photoexcitation processes, we examined the variation of the intensity maxima in the spectra near the points where two 2PPE features intersect, which arise either from a true resonance (i.e., a direct band-to-band transition from initial state to intermediate state) or simply a simultaneous excitation from two different initial states into the same final state. In particular, the peaks of the electron distribution curves away from the intersection points for the Fig. 6.1(a) data were fit for each of the features and the extracted intensities were then normalized to the relevant peak signal. A comparison of the sum of these individual intensities extrapolated to the intersection points, with the actual measured intensities at the maxima, may be used to determine the nature of the excitation (Fig. 6.3). For the SS and IS2 bands, an extrapolation of the individual contributions to the resonance peak at $k_{||} = 0.22$ Å^{-1} shows that their sum (solid line, Fig. 3(a) inset) is about half of the measured intensity. The fact that the total intensity is not simply a sum of the contributions implies that the maximum signal is the result of a resonant excitation between the SS and IS2. In fact, at $k_{||} = 0.22$ Å^{-1}, the energy separation of these two bands is 4.88 ± 0.09 eV, which is equal, within the experimental error, to the photon energy, $\hbar\omega = 4.84 \pm 0.05$ eV.

Consider now the strong 2PPE signal at $k_{||} = 0.1$ Å^{-1}, which originates from the crossing of the IS1 and *sp* features. Performing the same analysis as above yields the results plotted in Fig. 3(b). Extrapolating and adding the measured intensities to the "resonance" location gives a value equal to within 10% of the total measured intensity (see Fig. 6.3(b) inset). The clear additive nature of these two contributions to the total signal implies that these two bands are predominantly independent of each other since the momentum-conserving transitions between these two states are not possible. Thus, at the point where the two features cross, the total intensity is due to the sum of the intensities of separate transitions. These results however do not preclude possible coupling between bulk and the 2D states, as seen in 3PPE [171, 172]

Our observed *sp*-features, Fig. 6.1, agree with the Cu band structure that was obtained

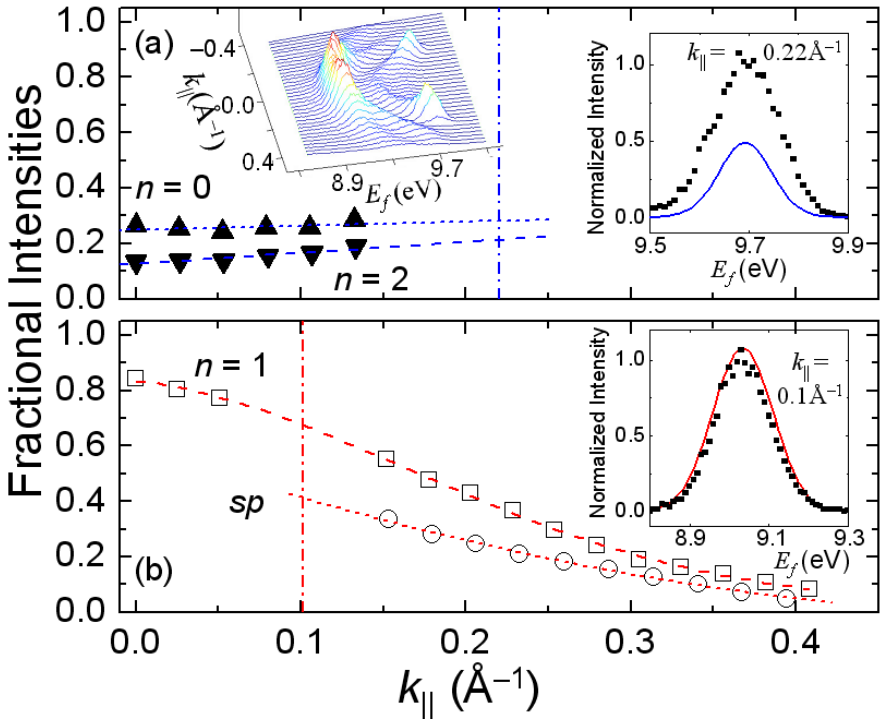

Figure 6.3: Contributions to $\hbar\omega$ =4.84 eV spectrum. Top inset (2PPE spectrum). Fractional signals for (a) $n = 0$ and 2, and (b) $n = 1$ and sp-band, states relative to the peak signals at $k_{||} = 0.22$ and 0.1 Å^{-1}, respectively. Vertical dash-dot lines: signal-maxima positions. Other insets: squares (data), solid lines are corresponding sums of the extrapolated contributions to the peaks at maxima $k_{||}$ values.

using a tight-binding code employing a 9×9 Hamiltonian [168]. (For a list of references on Cu band structure, see Refs. [6] and [173, 174, 175].) Here, the position of the upper band was adjusted by 0.35 eV so that the L-gap is equal to its experimentally measured value of 4.95 eV for Cu [6, 176]. In Fig. 6.4(a), the pairs of relevant bands are shown for the first excitation step of the 2PPE process as a function of $k_\perp$ and $k_{||}$ in the vicinity of the L-point, i.e., $(k_\perp, k_{||}) = (1.507, 0.0)$ Å^{-1} (see Fig. 4). The 2D-projected intermediate state transitions are shown as dashed lines in Fig. 6.1(d)-(f), in excellent agreement with the experimental results. The observed bulk transitions can only occur for values of $\mathbf{k}$, which satisfy the following three criteria simultaneously: (I) $E_m(\mathbf{k}) - E_i(\mathbf{k}) = \hbar\omega$, (II) $E_F \leq E_m(\mathbf{k}) \leq E_v$, and (III) $E_i(\mathbf{k}) \leq E_F$, where E_i and E_m are the initial state and intermediate state energies, respectively. These criteria thus imply a finite range of $\mathbf{k}$, hence

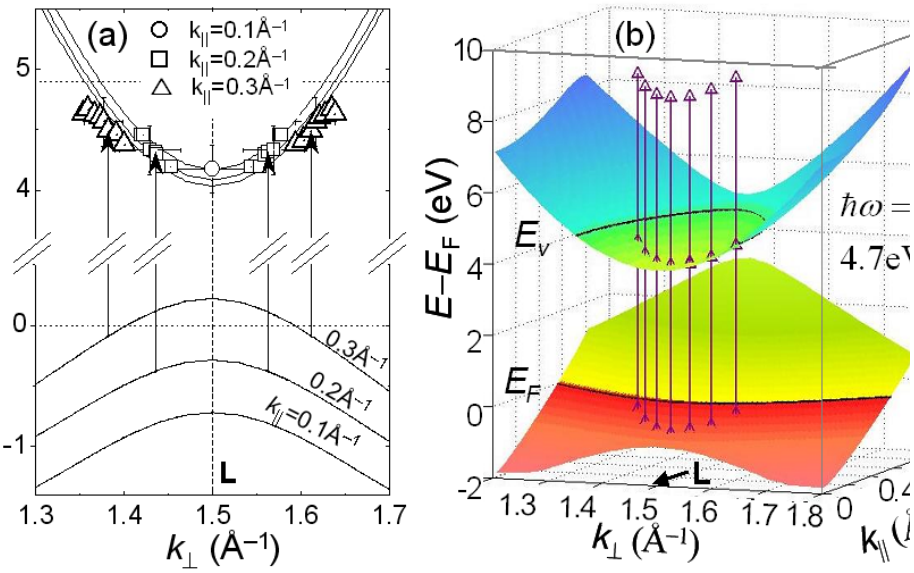

Figure 6.4: (a) Lines: calculated energy band structure vs. $k_\perp$ at fixed $k_{||}$ values. Symbols: measured band map of bound, unoccupied states. (b) Calculated band structure vs. $k_\perp$ and $k_{||}$. Transitions with $\hbar\omega = 4.7$ eV are indicated.

$k_{||}$, values at these transitions. For Cu(111), these conditions may be satisfied near the L-point. In our case, the lower limit of allowed $|k_{||}|$ values is set by criterion I, while the upper limit is set either by criterion II (the onset of one-photon PE occurs when $E_m > E_v$) or by criterion III (Fermi cutoff). As $\hbar\omega$ is decreased, the available range of $|k_{||}|$ decreases and these bulk transition features become more isolated in our spectrum as observed in Fig. 1(c).

Our measured non-integer E_f-vs.-$\hbar\omega$ slope for the *sp*-band may be explained by approximating the upper and lower *sp*-bands as two parabolic bands [Fig. 4(a)] with quadratic coefficients α_1 and $-\alpha_2$, respectively. Using $E_f(\mathbf{k}) = E_m(\mathbf{k}) + \hbar\omega$, we obtain $dE_f/d(\hbar\omega) = 1 + (1 + \alpha_2/\alpha_1)^{-1} = 1.67 \pm 0.02$, averaged over the range $k_{||} = 0$ to 0.4 Å^{-1}, in excellent agreement with the measured value of 1.64 ± 0.09. This non-integer slope implies that the transition cannot involve a 2D state, and is a consequence of the extra degree of freedom arising from the additional quantum number, $k_\perp$. Our measured data together with a knowledge of the initial states permit us to map the intermediate state band structure, i.e., E_m

vs. $k_\perp$, as shown in Fig. 4(a) for $k_{||}$=0.1 to 0.3 Å^{-1}. This map is obtained by first extracting E_i from the data using the relation $E_i = \Phi + KE - 2\hbar\omega$, then extracting $k_\perp$ at the given E_i using the known Cu band structure for states below E_F and for which intermediate states are accessible by vertical transitions using our photon energies. The resulting values of $E_m = E_i + \hbar\omega$, agree with the theoretical curves within the uncertainty limits.

The excellent agreement between theory and experiment implies that the two-step transitions are vertical in E vs. $\mathbf{k}$ space and, thus, do not involve changes in crystal momentum [see Fig. 4(b)]. Examination of the Cu band structure, however, shows that the only momentum conserving transitions in this final stage are located > 12 eV above the intermediate bands, and, hence, are not accessible for low photon energies. The lack of an energetically accessible well-defined bulk free-electron band implies that the final PE transition proceeds as a one-step process [177, 178, 179] involving the near-surface electrons into the strongly damped inverse-LEED states [6, 162].

6.4 Conclusion

In this chapter, I have demonstrated an example of non-equilibrium mapping of bound, unoccupied bulk states below E_v with two-photon photoemission. Such states are, in general, hard to access by standard photoemission techniques. However, I have shown that these states are distinguishable from and are predominantly independent of the well-known 2D-state transitions. Such states possess a non-integer final-state dispersion with respect to $\hbar\omega$, which illustrates the significant role of $k_\perp$. This result is relevant for a better understanding of bulk electronic structures and it opens new avenues for high energy-resolution studies and direct measurements of unoccupied bulk-state lifetimes and electron dynamics.

Bibliography

[1] AH Neto, F. Guinea, NMR Peres, KS Novoselov, and AK Geim. The electronic properties of graphene. *Reviews of Modern Physics*, 81(1):109–162, 2009.

[2] A. Fasolino, JH Los, and MI Katsnelson. Intrinsic ripples in graphene. *Nature Materials*, 6(11):858–861, 2007.

[3] E. Bauer. Low energy electron microscopy. *Reports on Progress in Physics*, 57:895, 1994.

[4] H. Lüth. *Solid surfaces, interfaces and thin films*. Springer, 2010.

[5] Saiht. General principle of arpes with description. *Wikipedia: The Free Encyclopedia.*, 2009. [Online; accessed 30-June-2011].

[6] S. Hüfner. *Photoelectron spectroscopy: principles and applications*. Springer Verlag, 2003.

[7] C.H. Park, F. Giustino, C.D. Spataru, M.L. Cohen, and S.G. Louie. Angle-resolved photoemission spectra of graphene from first-principles calculations. *Nano letters*, 9(12):4234–4239, 2009.

[8] A. Bostwick, T. Ohta, T. Seyller, K. Horn, and E. Rotenberg. Quasiparticle dynamics in graphene. *Nature Physics*, 3(1):36–40, 2006.

[9] KS Novoselov, AK Geim, SV Morozov, D. Jiang, Y. Zhang, SV Dubonos, IV Grigorieva, and AA Firsov. Electric field effect in atomically thin carbon films. *Science*, 306(5696):666, 2004.

[10] PR Wallace. The band theory of graphite. *Physical Review*, 71(9):622, 1947.

[11] KS Novoselov, AK Geim, SV Morozov, D. Jiang, M.I.K.I.V. Grigorieva, SV Dubonos, and AA Firsov. Two-dimensional gas of massless Dirac fermions in graphene. *Nature*, 438(7065):197–200, 2005.

[12] Y. Zhang, Y.W. Tan, H.L. Stormer, and P. Kim. Experimental observation of the quantum Hall effect and Berry's phase in graphene. *Nature*, 438(7065):201–204, 2005.

[13] LD Landau. Zur theorie der phasenumwandlungen ii. *Phys. Z. Sowjetunion*, 11:26–35, 1937.

[14] RE Peierls. Bemerkungen über umwandlungstemperaturen. *Helv. Phys. Acta*, 7:81–83, 1934.

[15] N.D. Mermin. Crystalline order in two dimensions. *Physical Review*, 176(1):250–254, 1968.

[16] D.R. Nelson, T. Piran, S. Weinberg, et al. *Statistical mechanics of membranes and surfaces*. World Scientific Pub., 2004.

[17] W. Shockley. On the surface states associated with a periodic potential. *Physical review*, 56(4):317, 1939.

[18] IE Tamm. On the possible bound states of electrons on a crystal surface. *Phys. Z. Sowjetunion*, 1:733–735, 1932.

[19] EG McRae. Electronic surface resonances of crystals. *Reviews of Modern Physics*, 51(3):541, 1979.

[20] R.M. Osgood Jr and X. Wang. Image states on single-crystal metal surface. *Solid State Physics*, 51:1–80, 1997.

[21] P. Echenique. Theory of image states at metal surfaces. *Progress in surface science*, 32:111–159, 1989.

[22] V. Dose, W. Altmann, A. Goldmann, U. Kolac, and J. Rogozik. Image-potential states observed by inverse photoemission. *Physical review letters*, 52(21):1919–1921, 1984.

[23] K. Giesen, F. Hage, FJ Himpsel, HJ Riess, and W. Steinmann. Two-photon photoemission via image-potential states. *Physical review letters*, 55(3):300–303, 1985.

[24] A. Locatelli, A. Bianco, D. Cocco, S. Cherifi, S. Heun, M. Marsi, M. Pasqualetto, and E. Bauer. High lateral resolution spectroscopic imaging of surfaces: The undulator beamline" nanospectroscopy" at Elettra. *J. Phys. IV France*, 104:99–102, 2003.

[25] T. Schmidt, S. Heun, J. Slezak, J. Diaz, KC Prince, G. Lilienkamp, and E. Bauer. SPELEEM: combining LEEM and spectroscopic imaging. *Surface Review and Letters*, 5(6):1287–1296, 1998.

[26] A. Locatelli and E. Bauer. Recent advances in chemical and magnetic imaging of surfaces and interfaces by XPEEM. *Journal of Physics: Condensed Matter*, 20:093002, 2008.

[27] A. Locatelli, L. Aballe, TO Mentes, M. Kiskinova, and E. Bauer. Photoemission electron microscopy with chemical sensitivity: SPELEEM methods and applications. *Surface and Interface Analysis*, 38(12-13):1554–1557, 2006.

[28] H. Hertz. Ueber einen einfluss des ultravioletten lichtes auf die electrische entladung. *Annalen der Physik*, 267(8):983–1000, 1887.

[29] A. Einstein. On a heuristic point of view concerning the production and transformation of light. *Annalen der Physik*, 17:132–148, 1905.

[30] EW Plummer and W. Eberhardt. Angle-resolved photoemission as a tool for the study of surfaces. 1982.

[31] FJ Himpsel. Angle-resolved measurements of the photoemission of electrons in the study of solids. *Advances in Physics*, 32(1):1–51, 1983.

[32] R. Courths and S. Hufner. Photoemission experiments on copper. *Physics Reports*, 112(2):53–171, 1984.

[33] LC Davis. Photoemission from transition metals and their compounds. *Journal of applied physics*, 59(6):R25–R64, 1986.

[34] CN Berglund and WE Spicer. Photoemission studies of copper and silver: Theory. *Physical Review*, 136(4A):1030–1044, 1964.

[35] V. Dose. Momentum-resolved inverse photoemission. *Surface Science Reports*, 5(8):337–378, 1985.

[36] N.V. Smith. Inverse photoemission. *Reports on Progress in Physics*, 51:1227, 1988.

[37] FJ Himpsel. Inverse photoemission from semiconductors. *Surface Science Reports*, 12(1):3–48, 1990.

[38] W. Steinmann. Spectroscopy of image-potential states by two-photon photoemission. *Applied Physics A: Materials Science & Processing*, 49(4):365–377, 1989.

[39] H.L. Dai and W. Ho. *Laser spectroscopy and photochemistry on metal surfaces*. World Scientific Pub Co Inc, 1995.

[40] R. Haight. Electron dynamics at surfaces. *Surface science reports*, 21(8):275–325, 1995.

[41] H. Petek and S. Ogawa. Femtosecond time-resolved two-photon photoemission studies of electron dynamics in metals. *Progress in surface science*, 56(4):239–310, 1997.

[42] M. Weinelt. Time-resolved two-photon photoemission from metal surfaces. *Journal of Physics: Condensed Matter*, 14:R1099, 2002.

[43] X.Y. Zhu. Electronic structure and electron dynamics at molecule-metal interfaces: implications for molecule-based electronics. *Surface science reports*, 56(1-2):1–83, 2004.

[44] J. Güdde and U. Höfer. Femtosecond time-resolved studies of image-potential states at surfaces and interfaces of rare-gas adlayers. *Progress in surface science*, 80(3-4):49–91, 2005.

[45] T. Fauster, M. Weinelt, and U. Hofer. Quasi-elastic scattering of electrons in image-potential states. *Progress in surface science*, 82(4-6):224–243, 2007.

[46] A. Hotzel. Electron dynamics of image potential states in weakly bound adsorbate layers: A short review. *Progress in surface science*, 82(4-6):336–354, 2007.

[47] PM Echenique, R. Berndt, EV Chulkov, T. Fauster, A. Goldmann, and U. Höfer. Decay of electronic excitations at metal surfaces. *Surface science reports*, 52(7-8):219–317, 2004.

[48] T. Wegehaupt, D. Rieger, and W. Steinmann. Observation of empty bulk states on cu (100) by two-photon photoemission. *Physical Review B*, 37(17):10086, 1988.

[49] K. Shudo and T. Munakata. Resonant photoexcitation of Si (001) measured with two-photon photoemission spectroscopy. *Physical Review B*, 63(12):125324, 2001.

[50] C. Kentsch, M. Kutschera, M. Weinelt, T. Fauster, and M. Rohlfing. Electronic structure of Si (100) surfaces studied by two-photon photoemission. *Physical Review B*, 65(3):35323, 2001.

[51] T. Ichibayashi and K. Tanimura. Identification of the conduction-band photoemission in time-resolved two-photon photoemission spectroscopy of Si surfaces. *Physical Review B*, 75(23):235327, 2007.

[52] M. Hengsberger, F. Baumberger, HJ Neff, T. Greber, and J. Osterwalder. Photoemission momentum mapping and wave function analysis of surface and bulk states on flat cu (111) and stepped cu (443) surfaces: A two-photon photoemission study. *Physical Review B*, 77(8):085425, 2008.

[53] Z. Hao, JI Dadap, KR Knox, MB Yilmaz, N. Zaki, PD Johnson, and RM Osgood. Nonequilibrium band mapping of unoccupied bulk states below the vacuum level by two-photon photoemission. *Physical review letters*, 105(1):17602, 2010.

[54] U. Höfer, IL Shumay, C. Reuß, U. Thomann, W. Wallauer, and T. Fauster. Time-resolved coherent photoelectron spectroscopy of quantized electronic states on metal surfaces. *Science*, 277(5331):1480, 1997.

[55] H. Petek, M.J. Weida, H. Nagano, and S. Ogawa. Real-time observation of adsorbate atom motion above a metal surface. *Science*, 288(5470):1402, 2000.

[56] J. Güdde, M. Rohleder, T. Meier, SW Koch, and U. Höfer. Time-resolved investigation of coherently controlled electric currents at a metal surface. *Science*, 318(5854):1287, 2007.

[57] S. Ogawa, H. Nagano, and H. Petek. Hot-electron dynamics at Cu (100), Cu (110), and Cu (111) surfaces: mComparison of experiment with Fermi-liquid theory. *Physical Review B*, 55(16):10869–10877, 1997.

[58] K. Ertel, U. Kohl, J. Lehmann, M. Merschdorf, W. Pfeiffer, A. Thon, S. Voll, and G. Gerber. Time-resolved two-photon photoemission spectroscopy of hopg and ag nanoparticles on hopg. *Applied Physics B: Lasers and Optics*, 68(3):439–445, 1999.

[59] A. Kubo, K. Onda, H. Petek, Z. Sun, Y.S. Jung, and H.K. Kim. Femtosecond imaging of surface plasmon dynamics in a nanostructured silver film. *Nano letters*, 5(6):1123–1127, 2005.

[60] N.H. Ge, CM Wong, RL Lingle, JD McNeill, KJ Gaffney, and CB Harris. Femtosecond dynamics of electron localization at interfaces. *Science*, 279(5348):202, 1998.

[61] P. Szymanski, S. Garrett-Roe, and C.B. Harris. Time-and angle-resolved two-photon photoemission studies of electron localization and solvation at interfaces. *Progress in surface science*, 78(1):1–39, 2005.

[62] A.D. Miller, I. Bezel, K.J. Gaffney, S. Garrett-Roe, SH Liu, P. Szymanski, and CB Harris. Electron solvation in two dimensions. *Science*, 297(5584):1163, 2002.

[63] U. Bovensiepen, C. Gahl, and M. Wolf. Solvation dynamics and evolution of the spatial extent of photoinjected electrons in d2o/cu (111). *The Journal of Physical Chemistry B*, 107(33):8706–8715, 2003.

[64] J. Zhao, B. Li, K. Onda, M. Feng, and H. Petek. Solvated electrons on metal oxide surfaces. *Chemical reviews*, 106(10):4402–4427, 2006.

[65] M. Muntwiler and X.Y. Zhu. Formation of two-dimensional polarons that are absent in three-dimensional crystals. *Physical review letters*, 98(24):246801, 2007.

[66] P. Blake, EW Hill, A.H.C. Neto, KS Novoselov, D. Jiang, R. Yang, TJ Booth, and AK Geim. Making graphene visible. *Applied Physics Letters*, 91:063124, 2007.

[67] A. Locatelli, K.R. Knox, D. Cvetko, T.O. Mentes, M.A. Niño, S. Wang, M.B. Yilmaz, P. Kim, R.M. Osgood Jr, and A. Morgante. Corrugation in Exfoliated Graphene: An Electron Microscopy and Diffraction Study. *ACS Nano*, 4(8):4879–4889, 2010.

[68] H. Hibino, H. Kageshima, F. Maeda, M. Nagase, Y. Kobayashi, and H. Yamaguchi. Microscopic thickness determination of thin graphite films formed on SiC from quantized oscillation in reflectivity of low-energy electrons. *Physical Review B*, 77(7):75413, 2008.

[69] MS Altman. Low energy electron microscopy of quantum well resonances in Ag films on W (110). *Journal of Physics: Condensed Matter*, 17:S1305, 2005.

[70] L. Liu, S. Ryu, M.R. Tomasik, E. Stolyarova, N. Jung, M.S. Hybertsen, M.L. Steigerwald, L.E. Brus, and G.W. Flynn. Graphene oxidation: Thickness-dependent etching and strong chemical doping. *Nano Lett*, 8(7):1965–1970, 2008.

[71] F. Schedin, AK Geim, SV Morozov, EW Hill, P. Blake, MI Katsnelson, and KS Novoselov. Detection of individual gas molecules adsorbed on graphene. *Nature Materials*, 6(9):652–655, 2007.

[72] D. Gazit. Theory of the spontaneous buckling of doped graphene. *Physical Review B*, 79(11):113411, 2009.

[73] E. Mariani and F. Von Oppen. Flexural phonons in free-standing graphene. *Physical review letters*, 100(7):76801, 2008.

[74] MI Katsnelson and AK Geim. Electron scattering on microscopic corrugations in graphene. *Philosophical Transactions A*, 366(1863):195, 2008.

[75] SC Xu, S. Irle, DG Musaev, and MC Lin. Quantum chemical study of the dissociative adsorption of OH and H2O on pristine and defective graphite (0001) surfaces: Reaction mechanisms and kinetics. 2006.

[76] M. Ishigami, JH Chen, WG Cullen, MS Fuhrer, and ED Williams. Atomic structure of graphene on SiO2. *Nano Lett*, 7(6):1643–1648, 2007.

[77] S. Niyogi, MA Hamon, H. Hu, B. Zhao, P. Bhowmik, R. Sen, ME Itkis, and RC Haddon. Chemistry of single-walled carbon nanotubes. *Acc. Chem. Res*, 35(12):1105–1113, 2002.

[78] KI Bolotin, KJ Sikes, Z. Jiang, M. Klima, G. Fudenberg, J. Hone, P. Kim, and HL Stormer. Ultrahigh electron mobility in suspended graphene. *Solid State Communications*, 146(9-10):351–355, 2008.

[79] J.C. Meyer, AK Geim, MI Katsnelson, KS Novoselov, TJ Booth, and S. Roth. The structure of suspended graphene sheets. *Nature*, 446(7131):60–63, 2007.

[80] W. Bao, F. Miao, Z. Chen, H. Zhang, W. Jang, C. Dames, and C.N. Lau. Controlled ripple texturing of suspended graphene and ultrathin graphite membranes. *Nature Nanotechnology*, 4(9):562–566, 2009.

[81] P. Le Doussal and L. Radzihovsky. Self-consistent theory of polymerized membranes. *Physical review letters*, 69(8):1209–1212, 1992.

[82] J.M. Carlsson. Graphene: Buckle or break. *Nature Materials*, 6(11):801–802, 2007.

[83] KV Zakharchenko, MI Katsnelson, and A. Fasolino. Finite temperature lattice properties of graphene beyond the quasiharmonic approximation. *Physical review letters*, 102(4):46808, 2009.

[84] E. Stolyarova, K.T. Rim, S. Ryu, J. Maultzsch, P. Kim, L.E. Brus, T.F. Heinz, M.S. Hybertsen, and G.W. Flynn. High-resolution scanning tunneling microscopy imaging of mesoscopic graphene sheets on an insulating surface. *Proceedings of the National Academy of Sciences*, 104(22):9209, 2007.

[85] FV Tikhonenko, DW Horsell, RV Gorbachev, and AK Savchenko. Weak localization in graphene flakes. *Physical review letters*, 100(5):56802, 2008.

[86] V. Geringer, M. Liebmann, T. Echtermeyer, S. Runte, M. Schmidt, R. Ruckamp, MC Lemme, and M. Morgenstern. Intrinsic and extrinsic corrugation of monolayer graphene deposited on SiO_2. *Physical Review Letters*, 102(7):76102, 2009.

[87] MS Altman, WF Chung, ZQ He, HC Poon, and SY Tong. Quantum size effect in low energy electron diffraction of thin films. *Applied Surface Science*, 169:82–87, 2001.

[88] JJ Paggel, T. Miller, and T.C. Chiang. Occupied and unoccupied band structure of Ag (100) determined by photoemission from Ag quantum wells and bulk samples. *Physical Review B*, 61(3):1804–1810, 2000.

[89] YZ Wu, AK Schmid, MS Altman, XF Jin, and ZQ Qiu. Spin-Dependent Fabry-Pérot Interference from a Cu Thin Film Grown on fcc Co (001). *Physical review letters*, 94(2):27201, 2005.

[90] KL Man, ZQ Qiu, and MS Altman. Kinetic limitations in electronic growth of Ag films on Fe (100). *Physical review letters*, 93(23):236104, 2004.

[91] T. Takahashi, H. Tokailin, and T. Sagawa. Angle-resolved ultraviolet photoelectron spectroscopy of the unoccupied band structure of graphite. *Physical Review B*, 32(12):8317–8324, 1985.

[92] T. Ohta, F.E. Gabaly, A. Bostwick, J.L. McChesney, K.V. Emtsev, A.K. Schmid, T. Seyller, K. Horn, and E. Rotenberg. Morphology of graphene thin film growth on SiC (0001). *New Journal of Physics*, 10:023034, 2008.

[93] M.H. Gass, U. Bangert, A.L. Bleloch, P. Wang, R.R. Nair, and AK Geim. Free-standing graphene at atomic resolution. *Nature nanotechnology*, 3(11):676–681, 2008.

[94] H.N. Yang, G.C. Wang, and T.M. Lu. *Diffraction from rough surfaces and dynamic growth fronts*. World Scientific Pub Co Inc, 1993.

[95] H.N. Yang, T.M. Lu, and G.C. Wang. Diffraction from surface growth fronts. *Physical Review B*, 47(7):3911–3922, 1993.

[96] YP Zhao, G.C. Wang, and TM Lu. Characterization of amorphous and crystalline rough surfaces: principles and applications, Experimental Methods in the Physical Science, vol. 37, 2001.

[97] T.M. Lu and MG Lagally. Diffraction from surfaces with randomly distributed steps. *Surface Science*, 120(1):47–66, 1982.

[98] H.N. Yang, T.M. Lu, and G.C. Wang. Time-invariant structure factor in an epitaxial growth front. *Physical review letters*, 68(17):2612–2615, 1992.

[99] HN Yang, GC Wang, and TM Lu. Instability in Low-Temperature Molecular-Beam Epitaxy Growth of Si/Si (111). *Physical review letters*, 73(17):2348–2351, 1994.

[100] Y.P. Zhao, H.N. Yang, G.C. Wang, and T.M. Lu. Diffraction from diffusion-barrier-induced mound structures in epitaxial growth fronts. *Physical Review B*, 57(3):1922–1934, 1998.

[101] P. Buseck, J. Cowley, and L.R. Eyring. High-Resolution Transmission Electron Microscopy-and Associated Techniques. 1989.

[102] T. Ohta, A. Bostwick, T. Seyller, K. Horn, and E. Rotenberg. Controlling the electronic structure of bilayer graphene. *Science*, 313(5789):951, 2006.

[103] Y.S. Dedkov, M. Fonin, U. Rüdiger, and C. Laubschat. Rashba effect in the graphene/Ni (111) system. *Physical Review Letters*, 100(10):107602, 2008.

[104] AM Shikin, GV Prudnikova, VK Adamchuk, F. Moresco, and K.H. Rieder. Surface intercalation of gold underneath a graphite monolayer on Ni (111) studied by angle-resolved photoemission and high-resolution electron-energy-loss spectroscopy. *Physical Review B*, 62(19):13202–13208, 2000.

[105] AL Vázquez de Parga, F. Calleja, B. Borca, MCG Passeggi Jr, JJ Hinarejos, F. Guinea, and R. Miranda. Periodically rippled graphene: Growth and spatially resolved electronic structure. *Physical Review Letters*, 100(5):56807, 2008.

[106] Y. Liu, L. Zhang, MK Brinkley, G. Bian, T. Miller, and T.C. Chiang. Phonon-Induced Gaps in Graphene and Graphite Observed by Angle-Resolved Photoemission. *Physical Review Letters*, 105(13):136804, 2010.

[107] I. Pletikosić, M. Kralj, P. Pervan, R. Brako, J. Coraux, AT N'Diaye, C. Busse, and T. Michely. Dirac cones and minigaps for graphene on Ir (111). *Physical Review Letters*, 102(5):56808, 2009.

[108] P. Sutter, MS Hybertsen, JT Sadowski, and E. Sutter. Electronic structure of few-layer epitaxial graphene on Ru (0001). *Nano Letters*, 9(7):2654–2660, 2009.

[109] T. Valla, J. Camacho, Z.H. Pan, AV Fedorov, AC Walters, CA Howard, and M. Ellerby. Anisotropic Electron-Phonon Coupling and Dynamical Nesting on the Graphene Sheets in Superconducting CaC_6 using Angle-Resolved Photoemission Spectroscopy. *Physical Review Letters*, 102(10):107007, 2009.

[110] M. Sprinkle, D. Siegel, Y. Hu, J. Hicks, A. Tejeda, A. Taleb-Ibrahimi, P. Le Fèvre, F. Bertran, S. Vizzini, H. Enriquez, et al. First direct observation of a nearly ideal graphene band structure. *Physical Review Letters*, 103(22):226803, 2009.

[111] K.R. Knox, S. Wang, A. Morgante, D. Cvetko, A. Locatelli, T.O. Mentes, M.A. Niño, P. Kim, and RM Osgood Jr. Spectromicroscopy of single and multilayer graphene supported by a weakly interacting substrate. *Physical Review B*, 78(20):201408, 2008.

[112] F. Wang, Y. Zhang, C. Tian, C. Girit, A. Zettl, M. Crommie, and Y.R. Shen. Gate-variable optical transitions in graphene. *Science*, 320(5873):206, 2008.

[113] K.F. Mak, M.Y. Sfeir, J.A. Misewich, and T.F. Heinz. The evolution of electronic structure in few-layer graphene revealed by optical spectroscopy. *Proceedings of the National Academy of Sciences*, 107(34):14999, 2010.

[114] Y. Fujikawa, T. Sakurai, and RM Tromp. Micrometer-scale band mapping of single silver islands in real and reciprocal space. *Physical Review B*, 79(12):121401, 2009.

[115] W.G. Cullen, M. Yamamoto, K.M. Burson, JH Chen, C. Jang, L. Li, M.S. Fuhrer, and E.D. Williams. High-Fidelity Conformation of Graphene to SiO_2 Topographic Features. *Physical Review Letters*, 105(21):215504, 2010.

[116] E.L. Shirley, LJ Terminello, A. Santoni, and FJ Himpsel. Brillouin-zone-selection effects in graphite photoelectron angular distributions. *Physical Review B*, 51(19):13614–13622, 1995.

[117] AR Law, MT Johnson, and HP Hughes. Synchrotron-radiation-excited angle-resolved photoemission from single-crystal graphite. *Physical Review B*, 34(6):4289–4297, 1986.

[118] SY Zhou, G.H. Gweon, J. Graf, AV Fedorov, CD Spataru, RD Diehl, Y. Kopelevich, D.H. Lee, S.G. Louie, and A. Lanzara. First direct observation of Dirac fermions in graphite. *Nature Physics*, 2(9):595–599, 2006.

[119] K. Sugawara, T. Sato, S. Souma, T. Takahashi, and H. Suematsu. Anomalous quasiparticle lifetime and strong electron-phonon coupling in graphite. *Physical Review Letters*, 98(3):36801, 2007.

[120] SD Kevan and RH Gaylord. High-resolution photoemission study of the electronic structure of the noble-metal (111) surfaces. *Physical Review B*, 36(11):5809–5818, 1987.

[121] F. Theilmann, R. Matzdorf, and A. Goldmann. High-resolution photoemission studies at rough Cu (111) surfaces:: The influence of defect scattering and disorder-dependent dephasing processes. *Surface science*, 420(1):33–42, 1999.

[122] F. Theilmann, R. Matzdorf, G. Meister, and A. Goldmann. Influence of surface structural disorder on linewidths in angle-resolved photoemission spectra. *Physical Review B*, 56(7):3632–3635, 1997.

[123] NV Smith, P. Thiry, and Y. Petroff. Photoemission linewidths and quasiparticle lifetimes. *Physical Review B*, 47(23):15476–15481, 1993.

[124] Z. Jiang, EA Henriksen, LC Tung, Y.J. Wang, ME Schwartz, MY Han, P. Kim, and HL Stormer. Infrared spectroscopy of Landau levels of graphene. *Physical Review Letters*, 98(19):197403, 2007.

[125] ZQ Li, EA Henriksen, Z. Jiang, Z. Hao, MC Martin, P. Kim, HL Stormer, and DN Basov. Dirac charge dynamics in graphene by infrared spectroscopy. *Nature Physics*, 4(7):532–535, 2008.

[126] S. Xu, J. Cao, CC Miller, DA Mantell, RJD Miller, and Y. Gao. Energy dependence of electron lifetime in graphite observed with femtosecond photoemission spectroscopy. *Physical Review Letters*, 76(3):483–486, 1996.

[127] G. Li, A. Luican, and E.Y. Andrei. Scanning tunneling spectroscopy of graphene on graphite. *Physical Review Letters*, 102(17):176804, 2009.

[128] M.S. Foster and I.L. Aleiner. Graphene via large N: A renormalization group study. *Physical Review B*, 77(19):195413, 2008.

[129] S. Das Sarma, EH Hwang, and W.K. Tse. Many-body interaction effects in doped and undoped graphene: Fermi liquid versus non-Fermi liquid. *Physical Review B*, 75(12):121406, 2007.

[130] J Gonzalez, F Guinea, and MAH Vozmediano. Unconventional quasiparticle lifetime in graphite. *Physical Review Letters*, 77(17):3589–3592, OCT 21 1996.

[131] J. Gonzalez, F. Guinea, and MAH Vozmediano. Electron-electron interactions in graphene sheets. *Physical Review B*, 63(13):134421, 2001.

[132] S. Schuppler, N. Fischer, W. Steinmann, R. Schneider, and E. Bertel. Image-potential states on ni (111): A two-photon-photoemission study. *Physical Review B*, 42(15):9403, 1990.

[133] XY Wang, XJ Shen, RM Osgood, et al. Surface electron motion near monatomic steps: Two-photon photoemission studies on stepped cu (111). *Physical Review B*, 56(12):7665, 1997.

[134] W. Berthold, U. Höfer, P. Feulner, EV Chulkov, VM Silkin, and PM Echenique. Momentum-resolved lifetimes of image-potential states on cu (100). *Physical Review Letters*, 88(5):56805, 2002.

[135] H. Ueba. A simple theory of two-photon photoemission from clean and adsorbate covered metal surfaces. *Surface science*, 334(1-3):L719–L729, 1995.

[136] H. Ueba and B. Gumhalter. Theory of two-photon photoemission spectroscopy of surfaces. *Progress in surface science*, 82(4-6):193–223, 2007.

[137] W. Wallauer and T. Fauster. Two-photon excitation processes and linewidths of surface and image states on cu (111). *Surface science*, 374(1-3):44–50, 1997.

[138] E. Knoesel, A. Hotzel, and M. Wolf. Temperature dependence of surface state lifetimes, dephasing rates and binding energies on cu (111) studied with time-resolved photoemission. *Journal of electron spectroscopy and related phenomena*, 88:577–584, 1998.

[139] M. Wolf, E. Knoesel, and T. Hertel. Ultrafast dynamics of electrons in image-potential states on clean and xe-covered cu (111). *Physical Review B*, 54(8):5295–5298, 1996.

[140] XY Wang, XJ Shen, RM Osgood Jr, R. Haight, and FJ Himpsel. Observation of lateral superlattice effects on stepped cu (001). *Physical Review B*, 53:15738–15742, 1996.

[141] S.C. Wang, MB Yilmaz, KR Knox, N. Zaki, JI Dadap, T. Valla, PD Johnson, and RM Osgood Jr. Electronic structure of a co-decorated vicinal cu (775) surface: High-resolution photoemission spectroscopy. *Physical Review B*, 77(11):115448, 2008.

[142] F. Baumberger, T. Greber, and J. Osterwalder. Fermi surfaces of the two-dimensional surface states on vicinal cu (111). *Physical Review B*, 64(19):195411, 2001.

[143] R. Eder and H. Winter. Electronic structure and angle-resolved photoemission spectra of vicinal cu (111) surfaces via the one-step model. *Physical Review B*, 70(8):085413, 2004.

[144] J. Lobo, EG Michel, AR Bachmann, S. Speller, L. Roca, J. Kuntze, and JE Ortega. Surface electronic structure of a vicinal cu crystal. *Journal of Vacuum Science & Technology A: Vacuum, Surfaces, and Films*, 21:1194, 2003.

[145] F. Baumberger, M. Hengsberger, M. Muntwiler, M. Shi, J. Krempasky, L. Patthey, J. Osterwalder, and T. Greber. Localization of surface states in disordered step lattices. *Physical review letters*, 92(19):196805, 2004.

[146] N. Zaki, K. Knox, PD Johnson, J. Fujii, I. Vobornik, G. Panaccione, and RM Osgood. Surface states on vicinal cu (775): Stm and photoemission study. *Physical Review B*, 83(20):205420, 2011.

[147] EV Chulkov, VM Silkin, and PM Echenique. Image potential states on metal surfaces: binding energies and wave functions. *Surface science*, 437(3):330–352, 1999.

[148] I. Sarria, J. Osma, EV Chulkov, JM Pitarke, and PM Echenique. Self-energy of image states on copper surfaces. *Physical Review B*, 60(16):11795, 1999.

[149] SV Eremeev, SS Tsirkin, and EV Chulkov. Dependence of the intrinsic line width of surface states on the wave vector: The cu (111) and ag (111) surfaces. *Physics of the Solid State*, 52(8):1768–1773, 2010.

[150] M. Roth, M. Pickel, W. Jinxiong, M. Weinelt, and T. Fauster. Electron scattering at steps: Image-potential states on cu (119). *Physical review letters*, 88(9):96802, 2002.

[151] LC Davis, MP Everson, RC Jaklevic, and W. Shen. Theory of the local density of surface states on a metal: Comparison with scanning tunneling spectroscopy of a au (111) surface. *Physical Review B*, 43(5):3821, 1991.

[152] O. Sánchez, J.M. García, P. Segovia, J. Alvarez, A.L.V. de Parga, JE Ortega, M. Prietsch, and R. Miranda. Lateral confinement of surface states on stepped cu (111). *Physical Review B*, 52(11):7894, 1995.

[153] F. Schiller, M. Ruiz-Osés, J. Cordón, and JE Ortega. Scattering of surface states at step edges in nanostripe arrays. *Physical review letters*, 95(6):66805, 2005.

[154] A. Mugarza and JE Ortega. Electronic states at vicinal surfaces. *Journal of Physics: Condensed Matter*, 15:S3281, 2003.

[155] G. Ferrini, C. Giannetti, D. Fausti, G. Galimberti, M. Peloi, G.P. Banfi, and F. Parmigiani. Effective mass and momentum-resolved intrinsic linewidth of image-potential states on ag (100). *Physical Review B*, 67(23):235407, 2003.

[156] H.B. Yang, JD Rameau, PD Johnson, T. Valla, A. Tsvelik, and GD Gu. Emergence of preformed Cooper pairs from the doped Mott insulating state in Bi2Sr2CaCu2O8+ &dgr. *Nature*, 456(7218):77–80, 2008.

[157] K.Y. Yang, H.B. Yang, PD Johnson, TM Rice, and F.C. Zhang. Quasiparticles in the pseudogap phase of underdoped cuprate. *EPL (Europhysics Letters)*, 86:37002, 2009.

[158] PD Johnson and SL Hulbert. Inverse photoemission. *Review of Scientific Instruments*, 61:2277, 1990.

[159] S. Pawlik, R. Burgermeister, M. Bauer, and M. Aeschlimann. Direct transition in the system Ag (111) studied by one-and two-photon photoemission. *Surface Science*, 402:556–560, 1998.

[160] N. Pontius, V. Sametoglu, and H. Petek. Simulation of two-photon photoemission from the bulk sp-bands of Ag (111). *Physical Review B*, 72(11):115105, 2005.

[161] A. Winkelmann, V. Sametoglu, J. Zhao, A. Kubo, and H. Petek. Angle-dependent study of a direct optical transition in the sp bands of Ag (111) by one-and two-photon photoemission. *Physical Review B*, 76(19):195428, 2007.

[162] W. Schattke, EE Krasovskii, R. Díez Muiño, and PM Echenique. Direct resolution of unoccupied states in solids via two-photon photoemission. *Physical Review B*, 78(15):155314, 2008.

[163] X.G. Wen and P.A. Lee. Theory of Quasiparticles in the Underdoped High-T_C Superconducting State. *Physical Review Letters*, 80(10):2193–2196, 1998.

[164] K.Y. Yang, TM Rice, and F.C. Zhang. Phenomenological theory of the pseudogap state. *Physical Review B*, 73(17):174501, 2006.

[165] MC Teich, JM Schroeer, and GJ Wolga. Double-quantum photoelectric emission from sodium metal. *Physical Review Letters*, 13(21):611, 1964.

[166] D. Pines and P. Nozieres. The theory of quantum fluids. *Vol. I (Benjamin, New York)*, 1966.

[167] T. Hertel, E. Knoesel, M. Wolf, and G. Ertl. Ultrafast electron dynamics at Cu (111): Response of an electron gas to optical excitation. *Physical review letters*, 76(3):535–538, 1996.

[168] DA Papaconstantopoulos. *Handbook of the band structure of elemental solids*. Plenum press New York, 1986.

[169] H. Ehrenreich and HR Philipp. Optical properties of Ag and Cu. *Physical Review*, 128(4):1622–1629, 1962.

[170] S. Gao and BI Lundqvist. Two-dimensional electrons gas in surface rydberg states: Limits set by auger decay. *Solid State Communications*, 84(1-2):147–150, 1992.

[171] F. Bisio, M. Nỳvlt, J. Franta, H. Petek, and J. Kirschner. Mechanisms of high-order perturbative photoemission from Cu (001). *Physical review letters*, 96(8):87601, 2006.

[172] A. Winkelmann, W.C. Lin, C.T. Chiang, F. Bisio, H. Petek, and J. Kirschner. Resonant coherent three-photon photoemission from Cu (001). *Physical Review B*, 80(15):155128, 2009.

[173] G.A. Burdick. Energy band structure of copper. *Physical Review*, 129(1):138–150, 1963.

[174] NV Smith. Photoemission spectra and band structures of d-band metals. VII. Extensions of the combined interpolation scheme. *Physical Review B*, 19(10):5019–5027, 1979.

[175] H. Eckardt, L. Fritsche, and J. Noffke. Self-consistent relativistic band structure of the noble metals. *Journal of Physics F: Metal Physics*, 14:97, 1984.

[176] SA Lindgren, J. Paul, and L. Walldén. The cu conduction band gap at the l point determined by photoemission and electron reflectivity measurements. *Solid State Communications*, 44(5):639–642, 1982.

[177] P.J. Feibelman and DE Eastman. Photoemission spectroscopy, Correspondence between quantum theory and experimental phenomenology. *Physical Review B*, 10(12):4932–4947, 1974.

[178] A. Liebsch. Theory of angular resolved photoemission from adsorbates. *Physical Review Letters*, 32(21):1203–1206, 1974.

[179] JB Pendry. Theory of photoemission. *Surface science*, 57(2):679–705, 1976.